REPORT DOCUMENTATION PAGE

Form Approved OMB NO. 0704-0188

1. REPORT DATE (DD-MM-YYYY)	2. REPORT TYPE	3. DATES COVERED (From - To)
05-07-2013	Final Report	10-May-2009 - 9-May-2013

4. TITLE AND SUBTITLE	5a. CONTRACT NUMBER
Enhancement of Radiation Tolerance by Interfaces in Nanostructured Metallic Materials	W911NF-09-1-0223
	5b. GRANT NUMBER
	5c. PROGRAM ELEMENT NUMBER
	611102

6. AUTHORS	5d. PROJECT NUMBER
Xinghang Zhang	
	5e. TASK NUMBER
	5f. WORK UNIT NUMBER

7. PERFORMING ORGANIZATION NAMES AND ADDRESSES	8. PERFORMING ORGANIZATION REPORT NUMBER
Texas Engineering Experiment Station Office of Sponsored Research 400 Harvey Mitchell Parkway South, Suite 300 College Station, TX 77845 -4375	

9. SPONSORING/MONITORING AGENCY NAME(S) AND ADDRESS(ES)	10. SPONSOR/MONITOR'S ACRONYM(S)
U.S. Army Research Office P.O. Box 12211 Research Triangle Park, NC 27709-2211	ARO
	11. SPONSOR/MONITOR'S REPORT NUMBER(S)
	54184-MS.19

12. DISTRIBUTION AVAILIBILITY STATEMENT

Approved for Public Release; Distribution Unlimited

13. SUPPLEMENTARY NOTES

14. ABSTRACT

The objective of this project is to explore fundamental mechanisms through which interfaces (nanocrystalline grain boundaries or layer interface in multilayers) attract radiation induced point defects, expedite annihilation of vacancies and interstitials, and thus restore strong capability to absorb radiation induced point defects. The ultimate goal of this project is to construct unique interfaces to significantly enhance radiation tolerance of metallic materials.

15. SUBJECT TERMS

radiation damage, nanocrystalline metals, extreme environment

16. SECURITY CLASSIFICATION OF:			17. LIMITATION OF ABSTRACT	15. NUMBER OF PAGES	19a. NAME OF RESPONSIBLE PERSON
a. REPORT	b. ABSTRACT	c. THIS PAGE			Xinghang Zhang
UU	UU	UU	UU		19b. TELEPHONE NUMBER
					979-845-2143

Report Title

Enhancement of Radiation Tolerance by Interfaces in Nanostructured Metallic Materials

ABSTRACT

The objective of this project is to explore fundamental mechanisms through which interfaces (nanocrystalline grain boundaries or layer interface in multilayers) attract radiation induced point defects, expedite annihilation of vacancies and interstitials, and thus restore strong capability to absorb radiation induced point defects. The ultimate goal of this project is to construct unique interfaces to significantly enhance radiation tolerance of metallic materials.

The major technical accomplishments achieved during this project include the followings. First, we unveil for the first time (in Nature Communications 2013) that coherent and incoherent twin boundaries can offer an alternative solution to remove stacking fault tetrahedral (SFTs) in heavy ion irradiated nanotwinned Ag. We also revealed frequent twin boundary migration in nanotwinned Ag. Second, we show for the first time drastic difference on damage mechanisms between He ion and proton irradiated Ag/Ni multilayers. Third, we used a novel in situ Kr ion irradiation technique (through collaboration with Argonne National laboratory) to understand fundamental mechanisms of layer interface and high angle grain boundary induced radiation tolerance in Ag/Ni multilayer and nanocrystalline Ni. Finally we have shown that coherency of interface (in Cu/Fe) plays a critical role on radiation tolerance in multilayers.

Numerous invited talks have been delivered and 16 papers have been published. Three Ph.D. students worked on this project. One of them becomes a postdoctor at Los Alamos National Lab and another student will be a faculty member.

Enter List of papers submitted or published that acknowledge ARO support from the start of the project to the date of this printing. List the papers, including journal references, in the following categories:

(a) Papers published in peer-reviewed journals (N/A for none)

Received		Paper
07/05/2013	8.00	K.Y. Yu, Y. Liu, S. Rios, H. Wang, X. Zhang. Strengthening mechanisms of Ag/Ni immiscible multilayers with fcc/fcc interface, Surface and Coatings Technology, (06 2013): 0. doi: 10.1016/j.surfcoat.2013.05.051
07/05/2013	18.00	K.Y. Yu, , C. Sun, , Y. Chen, , Y. Liu, , H. Wang, , M.A. Kirk, , M. Li , X. Zhang. Superior tolerance of Ag/Ni multilayers against Kr ion irradiation:an in situ study, Philosophical Magazine, (08 2013): 0. doi:
07/05/2013	17.00	Y. Chen, Y. Liu, F. Khatkhatay, C. Sun, H. Wang, X. Zhang. Significant enhancement in the thermal stability of nanocrystalline metals via immiscible tri-phases, Scripta Materialia, (07 2012): 0. doi: 10.1016/j.scriptamat.2012.04.010
07/05/2013	16.00	Y. Chen, Y. Liu, C. Sun, K.Y. Yu, M. Song, H. Wang, X. Zhang. Microstructure and strengthening mechanisms in Cu/Fe multilayers, Acta Materialia, (10 2012): 6312. doi: 10.1016/j.actamat.2012.08.005
07/05/2013	15.00	E.G. Fu, H. Wang, J. Carter, Lin Shao, Y.Q. Wang, X. Zhang. Fluence-dependent radiation damage in helium (He) ion-irradiated Cu/V multilayers, Philosophical Magazine, (03 2013): 0. doi: 10.1080/14786435.2012.735773
07/05/2013	14.00	C. Sun, K.Y. Yu, J.H. Lee, Y. Liu, H. Wang, L. Shao, S.A. Maloy, K.T. Hartwig, X. Zhang. Enhanced radiation tolerance of ultrafine grained Fe–Cr–Ni alloy, Journal of Nuclear Materials, (01 2012): 0. doi: 10.1016/j.jnucmat.2011.10.001
07/05/2013	13.00	X. Zhang, E. G. Fu, Nan Li, A. Misra, Y.-Q. Wang, L. Shao, H. Wang. Design of Radiation Tolerant Nanostructured Metallic Multilayers, Journal of Engineering Materials and Technology, (10 2012): 41010. doi: 10.1115/1.4006979
07/05/2013	12.00	K.Y. Yu, Y. Liu, E.G. Fu, Y.Q. Wang, M.T. Myers, H. Wang, L. Shao, X. Zhang. Comparisons of radiation damage in He ion and proton irradiated immiscible Ag/Ni nanolayers, Journal of Nuclear Materials, (09 2013): 310. doi: 10.1016/j.jnucmat.2013.04.069
07/05/2013	11.00	K.Y. Yu, D. Bufford, F. Khatkhatay, H. Wang, M.A. Kirk, X. Zhang. In situ studies of irradiation-induced twin boundary migration in nanotwinned Ag, Scripta Materialia, (09 2013): 0. doi: 10.1016/j.scriptamat.2013.05.024
07/05/2013	10.00	M. Song, K. Y. Yu, Y. Chen, M. Kirk, M. Li, C. Sun, H. Wang, X. Zhang. In situ Evidence of Defect Cluster Absorption by Grain Boundaries in Kr Ion Irradiated Nanocrystalline Ni, METALLURGICAL AND MATERIALS TRANSACTIONS A, (02 2013): 1966. doi: 10.1007/s11661-013-1635-9
07/05/2013	9.00	K. Y. Yu, D. Bufford, C. Sun, Y. Liu, H. Wang, M. A. Kirk, M. Li, X. Zhang. Removal of stacking-fault tetrahedra by twin boundaries in nanotwinned metals, Nature Communications, (01 2013): 0. doi: 10.1038/ncomms2382
07/26/2012	7.00	K.Y. Yu, Y. Liu, C. Sun, H. Wang, L. Shao, E.G. Fu, X. Zhang. Radiation damage in helium ion irradiated nanocrystalline Fe, Journal of Nuclear Materials, (06 2012): 0. doi: 10.1016/j.jnucmat.2011.10.052
07/28/2011	1.00	Nan Li, M. S. Martin, O. Anderoglu, A. Misra, L. Shao, H. Wang, X. Zhang. He ion irradiation damage in Al?Nb multilayers, Journal of Applied Physics, (05 2009): 93503. doi: 10.1063/1.3138804
07/28/2011	2.00	Nan Li, K. Y. Yu, J. Lee, H. Wang, X. Zhang. Size dependent strengthening mechanisms in sputtered Fe/W multilayers, Journal of Applied Physics, (05 2010): 93503. doi: 10.1063/1.3400130

07/28/2011	3.00	E. G. Fu, A. Misra, M. J. Demkowicz, X. Zhang. Interface-enabled defect reduction in He ion irradiated metallic multilayers, JOM, (12 2010): 75. doi: 10.1007/s11837-010-0185-5
07/28/2011	4.00	Nan Li, J. Wang, J.Y. Huang, A. Misra, X. Zhang. In situ TEM observations of room temperature dislocation climb at interfaces in nanolayered Al/Nb composites, Scripta Materialia, (08 2010): 363. doi: 10.1016/j.scriptamat.2010.04.005
07/28/2011	5.00	E.G. Fu, A. Misra, H. Wang, Lin Shao, X. Zhang. Interface enabled defects reduction in helium ion irradiated Cu/V nanolayers, Journal of Nuclear Materials, (12 2010): 178. doi: 10.1016/j.jnucmat.2010.10.011
07/28/2011	6.00	Nan Li, J.J. Carter, A. Misra, L. Shao, H. Wang, X. Zhang. The influence of interfaces on the formation of bubbles in He-ion-irradiated Cu/Mo nanolayers, Philosophical Magazine Letters, (01 2011): 19. doi: 10.1080/09500839.2010.522210

TOTAL: **18**

Number of Papers published in peer-reviewed journals:

(b) Papers published in non-peer-reviewed journals (N/A for none)

Received   Paper

TOTAL:

Number of Papers published in non peer-reviewed journals:

(c) Presentations

Invited talks
1. "Radiation tolerance mechanism in Cu/V nanolayers", TMS annual meeting, 2010, Seattle, WA, Feb. 14-17, 2010. (TMS meeting is an international conference).
2. "Mechanical properties of nanotwinned metal films", Plasticity 2009, St. Thomas, VI, Jan. 4-9, 2009.
3. "Radiation damage in nanostructured metallic nanolayers", TMS 2009, San Francisco, CA, Feb. 22-25, 2009.
4. "Radiation damage in nanostructured metallic materials", Santa Barbara, University of California, Santa Barbara, March 2010.
5. "Radiation tolerant metallic multilayers and bulk ultra-fine grained steels", Engineering Conference International, "Innovative Materials Immune to Radiation", Vail, CO, Aug. 2010.
6. "Radiation tolerant metallic multilayers and bulk ultra-fine grained steels", The 5th Annual Asia-Pacific Nuclear Energy Forum on Materials for Nuclear Applications, June 2011, Berkeley, CA
7. "Radiation tolerant nanostructured metals", Los Alamos National Laboratory, Los Alamos, NM, DOE workshop, Sep. 2012.
8. "Enhanced irradiation tolerance of ultrafine grained Fe-Cr-Ni alloy and nanocrystalline Ni", American Nuclear Society, Chicago, IL summer 2012.

Number of Presentations: 12.00

Non Peer-Reviewed Conference Proceeding publications (other than abstracts):

<u>Received</u> <u>Paper</u>

TOTAL:

Number of Non Peer-Reviewed Conference Proceeding publications (other than abstracts):

Peer-Reviewed Conference Proceeding publications (other than abstracts):

<u>Received</u> <u>Paper</u>

TOTAL:

Number of Peer-Reviewed Conference Proceeding publications (other than abstracts):

(d) Manuscripts

<u>Received</u> <u>Paper</u>

TOTAL:

Number of Manuscripts:

Books

<u>Received</u> <u>Paper</u>

TOTAL:

Patents Submitted

Patents Awarded

Awards

1. Best graduate teaching award, Dept. Mechanical Engineering, Texas A&M University, 2009.
2. TEES (Texas Engineering Experiment Station) fellow, 2013.

---

3. Graduate student, Mr. Kaiyuan Yu, won TMS best graduate student paper (1st prize), 2013.
4. Graduate student, Mr. Cheng Sun, won TMS best graduate student paper (1st prize), 2012.

Graduate Students

NAME	PERCENT_SUPPORTED	Discipline
Youxing Chen	1.00	
Kaiyuan Yu	1.00	
Nan Li	0.20	
FTE Equivalent:	**2.20**	
Total Number:	**3**	

Names of Post Doctorates

NAME	PERCENT_SUPPORTED
FTE Equivalent:	
Total Number:	

Names of Faculty Supported

NAME	PERCENT_SUPPORTED	National Academy Member
Xinghang Zhang	0.50	No
FTE Equivalent:	**0.50**	
Total Number:	**1**	

Names of Under Graduate students supported

NAME	PERCENT_SUPPORTED	Discipline
Ms. Cassie L. Gutierrez	0.10	Mechanical Engineering
FTE Equivalent:	**0.10**	
Total Number:	**1**	

Student Metrics

This section only applies to graduating undergraduates supported by this agreement in this reporting period

The number of undergraduates funded by this agreement who graduated during this period: 1.00

The number of undergraduates funded by this agreement who graduated during this period with a degree in science, mathematics, engineering, or technology fields: 1.00

The number of undergraduates funded by your agreement who graduated during this period and will continue to pursue a graduate or Ph.D. degree in science, mathematics, engineering, or technology fields: 1.00

Number of graduating undergraduates who achieved a 3.5 GPA to 4.0 (4.0 max scale): 0.00

Number of graduating undergraduates funded by a DoD funded Center of Excellence grant for Education, Research and Engineering: 0.00

The number of undergraduates funded by your agreement who graduated during this period and intend to work for the Department of Defense 1.00

The number of undergraduates funded by your agreement who graduated during this period and will receive scholarships or fellowships for further studies in science, mathematics, engineering or technology fields: 1.00

Names of Personnel receiving masters degrees

NAME

Total Number:

Names of personnel receiving PHDs

NAME
Kaiyuan Yu
Nan Li

Total Number: **2**

Names of other research staff

NAME	PERCENT_SUPPORTED

FTE Equivalent:
Total Number:

Sub Contractors (DD882)

Inventions (DD882)

Scientific Progress

See Attachment

Technology Transfer

Texas A&M University/Texas Engineering Experiment Station

Final Progress Report to ARO

on the W911NF-09-1-0223 Contract

"**Enhancement of Radiation Tolerance by Interfaces in**

Nanostructured Metallic Materials"

For the Period of May 2009 - May 2013

By

Xinghang Zhang, Texas A&M University

July 5, 2013

ABSTRACT

This is the final progress report. The objective of this project is to explore fundamental mechanisms through which interfaces (nanocrystalline grain boundaries or layer interface in multilayers) attract radiation induced point defects, expedite annihilation of vacancies and interstitials, and thus restore strong capability to absorb radiation induced point defects. The ultimate goal of this project is to construct unique interfaces to significantly enhance radiation tolerance of metallic materials.

The major technical accomplishments achieved during this project include the followings. First, we unveil for the first time (in Nature Communications 2013) that coherent and incoherent twin boundaries can offer an alternative solution to remove stacking fault tetrahedral (SFTs) in heavy ion irradiated nanotwinned Ag. We also revealed frequent twin boundary migration in nanotwinned Ag. Second, we show for the first time drastic difference on damage mechanisms between He ion and proton irradiated Ag/Ni multilayers. Third, we used a novel in situ Kr ion irradiation technique (through collaboration with Argonne National laboratory) to understand fundamental mechanisms of layer interface and high angle grain boundary induced radiation tolerance in Ag/Ni

multilayer and nanocrystalline Ni. Finally we have shown that coherency of interface (in Cu/Fe) plays a critical role on radiation tolerance in multilayers.

Numerous invited talks have been delivered and 18 papers have been published. Three Ph.D. students worked on this project. One of them becomes a postdoctor at Los Alamos National Lab and another student will be a faculty member.

Some of the major technical accomplishments achieved during the period of May 2009 - May 2013 are briefly summarized as follows.

(1) We present an alternative solution to remove stacking fault tetrahedral (SFTs) generated during room-temperature, *in situ* Kr ion irradiation in epitaxial nanotwinned (nt) Ag with an average twin spacing of ~ 8 nm. A large number of SFTs were removed during their interactions with abundant coherent twin boundaries. Consequently the density of SFTs in irradiated nt Ag was much lower than that in its bulk counterpart. Two fundamental interaction mechanisms were identified, and compared to predictions by molecular dynamics simulations. *In situ* studies also revealed a new phenomenon: radiation induced frequent migration of coherent and incoherent twin boundaries. This study implies that twin boundaries are effective to destruct SFTs, which are previously believed very hard to eliminate.

(2) We have sputter-deposited Ag/Ni nanolayer films with individual layer thickness, *h*, varying from 1 to 200 nm, and these multilayers were subjected to 100 keV helium (He) ion irradiation to a fluence of 6×10^{20} ions/m^2, and compared with those irradiated by proton to a fluence of 6×10^{21} ions/m^2 at room temperature. Helium bubbles were found to be the major defects in helium irradiated films while dislocation loops were ubiquitous in proton irradiated multilayers. Radiation hardening decrease with decreasing individual layer thickness after helium radiation, whereas no size dependence was observed in proton irradiated films. Mechanisms of radiation hardening were discussed.

(3) We have also prepared nanostructured Cu/Fe multilayers on Si (110) and Si (100) substrates by magnetron sputtering, with individual layer thickness h, varying from 0.75 to 200 nm. The growth orientation relationship between Cu and Fe at interfaces was

determined to be Kurdjumov-Sachs and Nishiyama-Wasserman type. Nanoscale columnar grains in Fe, with an average grain size of 11 - 23 nm, played dominant roles on strengthening mechanism when h ≥ 50 nm. At smaller h, the hardness of Cu/Fe multilayers with (100) texture approached a peak value, followed by softening due to the formation of fully coherent interfaces. However, abundant twins were observed in Cu/Fe films with (111) texture at h of 0.75 nm, which led to high hardness in multilayers.

(4) Sputtered Cu/Fe nanolayer films were subjected to 100 keV helium (He) ion irradiation to a fluence of 6×10^{20} ions/m^2 at room temperature. Preliminary results have shown enhanced radiation tolerance in this system.

(5) *In situ* Kr^{++} ion irradiation with energy of 1 MeV at room temperature was performed in fcc coarse grained (CG) Ni with average grain size of 2.5µm and nanocrystalline (nc) Ni of average grain size of 55 nm. The microstructure evolution and the absorption of defect clusters by grain boundary were observed under transmission electron microscopy (TEM). The results indicated that the grain boundary structure effectively sucks the defect clusters and suppresses the formation of the defect clusters and dislocation segments. Up to a dose of 5 dpa, the defect cluster density and diameter of irradiated nc Ni are around two times lower than those in CG Ni.

(6) We report on *in situ* observation of Kr ion irradiation induced microstructure evolution in epitaxial nanotwinned Ag films with an average twin thickness of 70 nm. Kr ion irradiation induced defect clusters are absorbed by coherent and incoherent twin boundaries. Frequent interactions between defect clusters and twin boundaries lead to continuous migration of twin boundaries. The potential mechanisms of twin boundary migration are discussed.

I. Overall objective of the project

The goal of this project is to understand fundamental mechanisms, through which interfaces (grain boundary and interphase interfaces) in nanocrystalline and nanolayer metallic materials accumulate and promote annihilation of radiation induced point defects

(interstitials and vacancies), and to construct appropriate interfaces that will significantly enhance radiation tolerance of metals. To achieve the project goal, we will undertake the following tasks:

(1) Grain boundary mitigated radiation damage in nanocrystalline films. We will investigate the influences of grain sizes and crystal structures (fcc and bcc), in accumulating and annihilating point defects, and suppressing the formation of stacking fault tetrahedra. We will then explore the influence of radiation dose on hardening of films.

(2) Layer interface mitigated radiation damage in multilayer films. Two types of interfaces are chosen: coherent and incoherent interfaces. In both cases, immiscible system is a perquisite to avoid intermixing during ion irradiation. Incoherent interfaces will see a higher density of misfit dislocations along interfaces, and thus lead to segregation of point defects (vacancy and bubbles) to misfit dislocations. Coherency stress in coherent systems may lead to preferential generation of vacancy or interstitial in one of the constituent layer, which in turn might alleviate coherency stress to some extent. Both types of interface may facilitate migration and diffusion of point defects along interfaces and facilitate recombination of unlike point defects. We will first examine the radiation induced microstructural change by a combination of microscopy and high resolution XRD technique. Then study the thermal stability of films before and after radiation to examine evolution of interface stability, and study thermal stability of radiation induced defect clusters (He bubbles and interstitial loops) to identify appropriate temperature range for the application of multilayers. Radiation induced hardness and electrical resistivity change, indirect evidence for the evolution of point defect density, are anticipated to depend sensitively on the thickness of layers, type of interfaces (coherent vs. incoherent), and radiation dose etc.

(3) Twin boundary mitigated radiation damage in nanotwinned films. Twinning is another important type of nanostructure in materials and it has been increasingly investigated recently. Remarkable strengthening effect due to twinning has been found in Cu and Ag. But radiation damage in nanotwinned structure has been rarely studied. Atomistic modeling work by Demkowicz *et. al* has shown that ∑3 twin boundaries in Cu did not reduce the formation of defects clusters produced by He irradiation because

defect formation energies and Frenkel pair annihilation rates are comparable to those in neighboring matrix. Moreover, systematic simulation work regarding interaction of twinning structure and SFT has pointed out that the interaction leads to damage of parent SFTs and production of new defects in the twin lattice. Since the interaction in that study was triggered by twin boundary motion due to twin growth, we hypothesize that similar results should be found during a dynamic SFT generation process, namely *in situ* irradiation with heavy ion. We will first examine the SFTs generation during heavy ion radiation and observed their interactions with abundant coherent and incoherent twin boundaries.

II. Major technical accomplishments

II.1. Removal of stacking fault tetrahedra by twin boundaries in nanotwinned (Published in Nature Communications 2013)

Neutron, proton or heavy ion irradiation can create a large amount of defect clusters, including bubbles, voids, and dislocation loops in irradiated metallic materials. Consequently radiation may lead to void swelling and degrade the mechanical properties of metallic materials in terms of radiation hardening, embrittlement and irradiation induced creep. Various types of defect sinks, such as grain boundaries and interphase interfaces, have been used to reduce the density of radiation induced defects [1-4]. King and Smith studied the mechanism of point defect absorption by grain boundaries and $\sum 3$ {111} coherent twin boundaries (CTBs) in electron irradiated Al and Cu, and showed that twin boundaries may be biased sinks for dislocation loops [5]. Recently there are increasing interests on radiation tolerance of nanostructured materials because they possess a significant fraction of high-angle grain boundaries that led to reduction of radiation induced defect density [6, 7]. Atomistic modeling has also been adopted to investigate the radiation response of high-angle grain boundaries in nanomaterials [8-10]. Molecular dynamics (MD) simulations of $\Sigma 11$ grain boundaries in face-centered-cubic (fcc) Cu showed that radiation induced interstitials were first absorbed by grain boundaries to form interstitial-rich (or interstitial-loaded) grain boundaries which promote the vacancy-interstitial recombination. Compared to pristine grain boundaries,

the interstitial-rich grain boundaries reduce the barrier for interstitial emission and thus emitted interstitials (from grain boundaries) can effectively annihilate vacancies in grain interior [11]. Meanwhile the interstitial-rich grain boundaries also reduce the vacancy diffusion barrier so that it is easier for vacancies to migrate to grain boundaries where they recombine with interstitials. Besides high angle grain boundaries, layer interfaces in certain immiscible metallic multilayers [12-15] also act as remarkable sinks for point defects, and lead to dramatic reduction of defect density, swelling and radiation hardening. MD simulations showed that Cu/Nb layer interfaces can act as inexhaustible sinks for radiation induced point defects [16].

SFTs are a dominant type of vacancy clusters in various irradiated fcc metals with low-to-intermediate stacking fault energy [4, 17, 18] in absence of noble gases in the materials. SFTs, once formed via collapse of vacancy clusters [19, 20], are typically very stable, and their removal requires annealing at very high temperature [21], incorporation of interstitials via radiation [19] or mobile dislocations [22]. Effective removal of high density SFTs is necessary to minimize void swelling and alleviate radiation hardening. Recently Niewczas and Hoagland [23] simulated the interaction between $\sum 3$ {111} CTBs and SFTs and found that the interaction led to destabilization of parent SFTs and production of new defects at twin boundaries. But their prediction received little attention as the proposed interactions require frequent migration of Shockley partials and twin boundaries, which occurs only sporadically in conventional bulk metallic materials with coarse grains. Hence there is no experimental evidence to verify their predicted SFT removal mechanism to date. Meanwhile nanotwins have been shown to induce remarkably high mechanical strength in Cu, Ag and 330 stainless steel [24-27], and twin boundaries are mobile under stress or annealing [28, 29]. But little is known experimentally on radiation response of nanotwinned (nt) materials [30].

Here we report on an *in situ* study of radiation damage in epitaxial nt Ag films in a transmission electron microscope at room temperature. Significant findings include twin thickness dependent reduction of dislocation loop density, destruction of SFTs by twin boundaries and consequently drastic reduction of density of SFTs. Besides the validation of two SFT removal mechanisms predicted by MD simulations, we observed radiation induced migration of coherent and incoherent twin boundaries (ITBs). These findings

provide important implications for the design of swelling resistant structural materials, and offer basis for exploration of physics of radiation induced twin boundary migrations. Epitaxial Ag films with thickness of ~ 1 μm were synthesized on Si (111) substrate by using DC magnetron sputtering technique at room temperature. XTEM specimens for *in situ* radiation study were prepared. Details of deposition and specimen preparation can be found elsewhere [26]. Prior to and post irradiation, the specimen was investigated by an FEI Tecnai G2 F20 ST microscope. The thickness of TEM foil was measured to be ~ 110 nm by using the Kossel-Mollenstedt fringes captured under two-beam conditions. Numerous specimens were irradiated with 1 MeV Kr^{++} ions up to a maximum fluence of 2×10^{14} ions/m^2 (corresponding to a maximum of 1 dpa) at room temperature at the IVEM-TANDEM facility at Argonne National Laboratory where an ion accelerator is attached to a HITACHI H-9000NAR microscope. Depth dependent damage and defect concentration profile were calculated by the Stopping and Range of Ions in Matter (SRIM)-2008 [38] using a threshold energy of 40 eV for Ag. The density of defects, defined as the number of defects per unit volume, were estimated from abundant bright field and dark field TEM images.

*Microstructure of as-deposited and Kr irradiated nt Ag films*
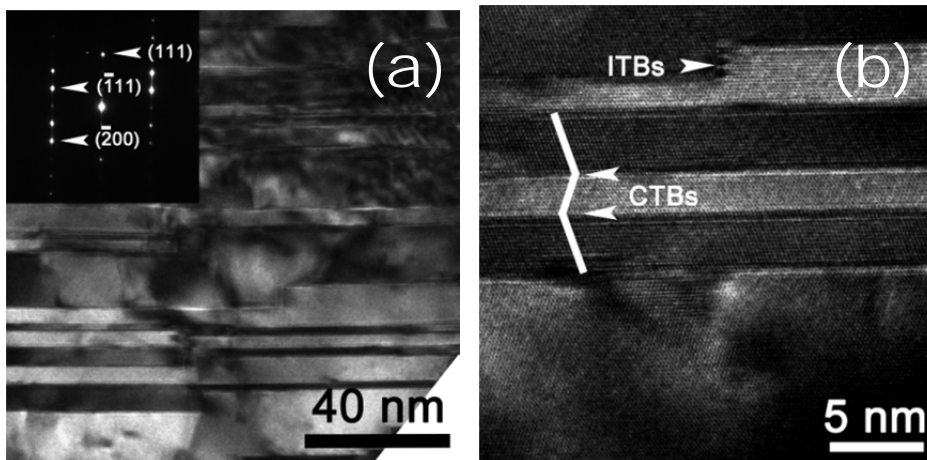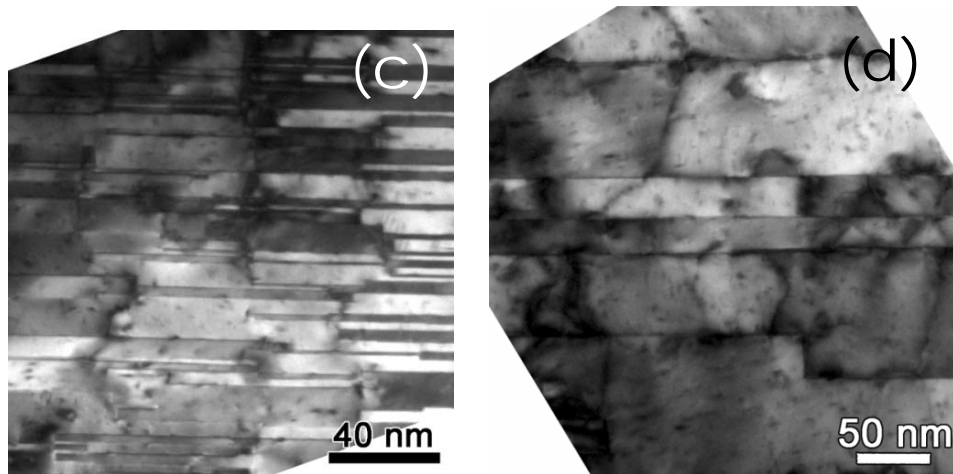
Figure 1.1 (a) XTEM image of as-deposited fine nt Ag (t_{ave} = 8 nm) shows high density of Σ3{111} growth twins with CTBs normal to the growth direction. The inserted SAD pattern reveals the orientation relationship between twins and matrix. (b) HRTEM micrograph shows the lateral Σ3 {1 1 1} CTBs and vertical Σ3 {1 1 2} ITBs. (c-d) Lower magnification TEM micrographs of as-deposited nt Ag (t_{ave} = 8 and 70 nm respectively) show a low density of dislocation loops and threading dislocations.
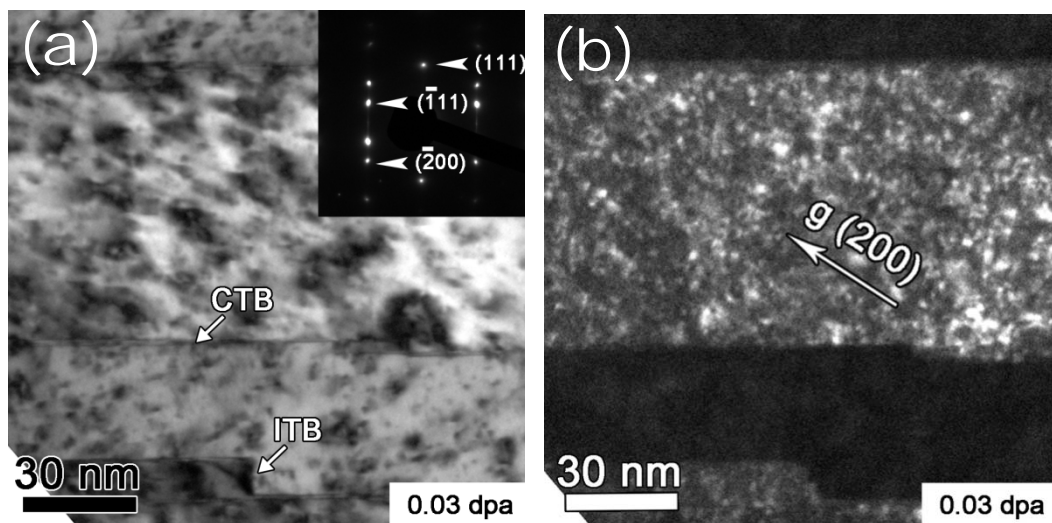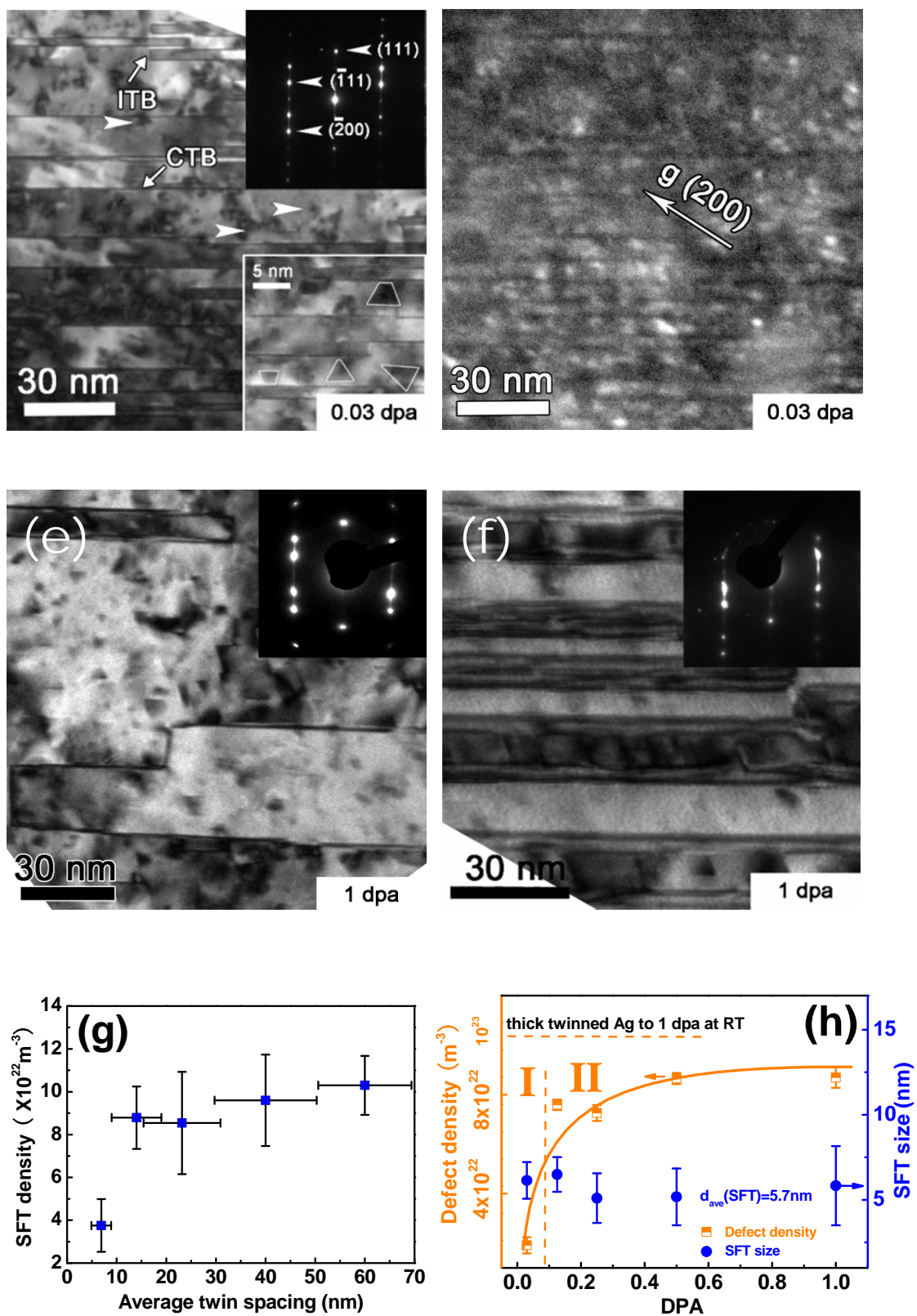
Figure 1.2 (a) Bright field XTEM micrograph of thick twinned Ag (t$_{ave}$ = 70 nm),

irradiated to 0.03 dpa and examined along the Ag <011> zone axis, shows high density of ∑3 {111} CTBs and vertical ∑3 {112} ITBs. High density defects were generated by irradiation. (b) Corresponding dark field image showing the formation of high density defects. (c) Bright field TEM micrograph of fine nt Ag (t_{ave} = 8 nm) irradiated to 0.03 dpa shows significantly lower defect density than thick twinned Ag. Irradiation led to triangular and trapezoidal SFTs (inset) and other defect clusters. (d) Corresponding dark field image of nt Ag confirms that defect density is much lower than that of thick twinned Ag. At 1 dpa, the density of defects in thick nt Ag (e) continued to increase and was much greater than thin nt Ag (f). The inserted selected area diffraction pattern in (f) shows much stronger intensity of streaking lines, implying the formation of a high density of stacking faults, which were observed along twin boundaries. (g) The density of SFTs decreased sharply at smaller average twin spacing (8 nm). All specimens were irradiated up to 1 dpa. (h) Density of defects (including SFTs and dislocation loops) in thick twinned Ag increased sharply and reached saturation at 0.01 dpa (as shown by the horizontal dash line). In comparison the density of defects in fine nt Ag (t_{ave} = 8 nm) increased gradually up to ~ 0.1 dpa in stage I, and then leveled off thereafter in stage II (0.1 -1 dpa) to a lower staturation value, at least 50% lower than that of thick twinned Ag. The average size of SFTs remained constant, ~ 5.7 nm, throughout the irradiation experiment.

As-deposited Ag films have high density growth twins (Fig. 1.1a-b) with Σ3{111} CTBs and Σ3{112} ITBs with an average twin spacing (t_{ave}) of 8 and 70 nm respectively. The average thickness of twins is identical to that of matrix, that is twins account for 50 vol.% of the films. The as-deposited nt Ag had very low density of growth defects (dislocation loops and threading dislocations, Fig. 1.1c-d). Fig. 1.2a shows a bright field (BF) cross-sectional transmission electron microscopy (XTEM) micrograph of nt Ag films with t_{ave} of 70 nm, irradiated by Kr ions up to a dose of 0.03 displacements-per-atom (dpa). High density nanotwins with sharp twin boundaries were observed throughout the specimen. The inserted selected area diffraction (SAD) pattern in Fig. 1.2a also provides clear evidence for the existence of Σ3{111} lateral CTBs. High density dark spots which are signatures of radiation induced defect clusters, were also

observed in the corresponding dark field TEM image in Fig. 1.2b. In comparison, nt Ag with t_{ave} of ~ 8 nm irradiated at the same condition has a much lower density of defect clusters as shown in Fig. 1.2c and d. Numerous SFTs were produced by radiation as indicated in the inset of Fig. 1.2c. The bases of SFTs were parallel to the CTBs and some SFTs were apparently truncated. Extra diffraction spots in SAD pattern arose from Σ3{112} ITBs as observed previously in as-deposited nt Ag and Cu [26, 31]. Radiation at 0.25 dpa led to significant increase in defect density in the thick nt Ag, whereas the defect density in the fine nt Ag only increased moderately .
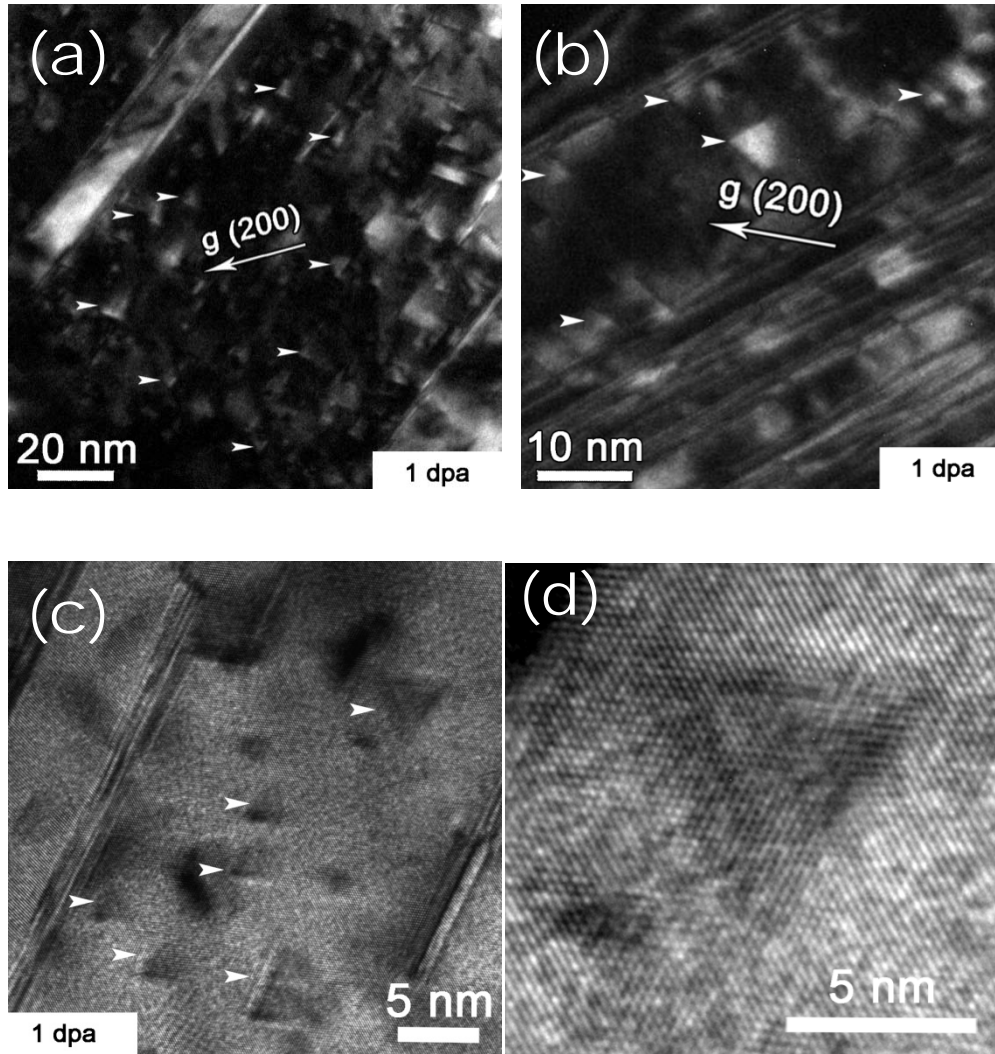
Figure 1.3 (a) Dark field TEM image of nt Ag (t_{ave} = 8 nm) irradiated to 1 dpa shows the formation of high density SFTs (indicated by arrows). (b) A higher magnification TEM micrograph shows distinct triangular geometry of SFTs. (c-d) HRTEM micrographs

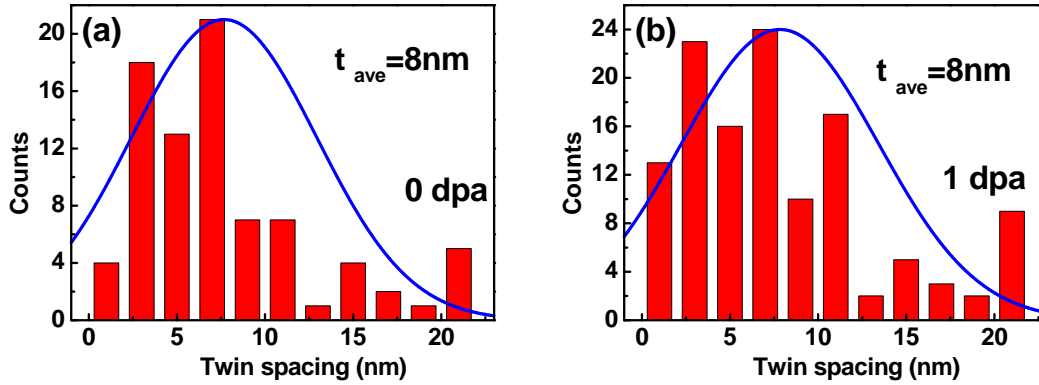reveal SFTs at atomic resolution in the same irradiated specimen.

Figure 1.4 Histograms of twin spacing measured from numerous XTEM images. As-deposited (a) and irradiated (b) nt Ag film (up to 1 dpa) have identical average twin spacing, ~ 8 nm.

Detailed microstructural examination of nt Ag irradiated to 1 dpa also reveals several important characteristics. First, smaller twin spacing led to less SFTs. Fewer defects, and in particular fewer SFTs, were formed in the fine nt Ag (Fig. 1.2f) than that in the thick nt Ag (Fig. 1.2e). Besides bright field TEM, extensive dark field TEM and HRTEM studies were also performed to identify SFTs and determine their density (Fig. 1.3). Second, many truncated SFTs were observed. Third, stacking faults (SFs) were observed frequently next to twin boundaries and inside twins in both fine and thick twinned Ag, and the existence of SFs is also confirmed by both elongated diffraction dots and streaking lines in the insets of Fig. 1.2e and f. Statistics in Fig. 1.2g shows the density of SFTs reduced gradually with decreasing twin spacing down to ~ 15 nm, and was significantly lower when $t < 10$ nm. Furthermore in Kr ion irradiated nt Ag ($t_{ave} = 8$ nm) the density of defects (including SFTs and dislocation loops) increased with dose rapidly prior to 0.1 dpa (Fig. 1.2h) and saturated thereafter up to 1 dpa. Meanwhile, the thick nt Ag showed at least twice greater defect density (Fig. 1.2h), which saturated at a much lower dose (0.01 dpa) during *in situ* irradiation. The average dimension of SFTs remained 5 - 6 nm over 0.01 - 1 dpa (Fig. 1.2h). Comparison of fine nt Ag before and after radiation (1 dpa) shows that the t_{ave} remains the same, ~ 8 nm (as shown in Fig. 1.4).

Mechanism of SFT/tb interaction

According to the Silcox and Hirsch model [32], SFTs can evolve from Frank loops through the migration of Shockley partials and the formation of stair-rod dislocations. To understand the formation of SFTs, we first compare the energetics for the formation of perfect loops versus Frank loops in Ag. The size of SFTs is evaluated by their edge length (L). The loop radius (r_L) is defined as the radius of the circum-circle of one tetrahedron face. The formation of a faulted loop is favored over a perfect loop if the following criterion satisfies [19]

$$\gamma_{SFE} < \frac{\mu b^2}{3\pi r_L}\left(\frac{2-\nu}{2(1-\nu)}\right)\ln\left[\frac{4r_L}{r_c} - 2\right]$$

(1),

where γ_{SFE} is the stacking fault energy (SFE), which is ~ 17mJ/m^2 for Ag [33], μ is the shear modulus, b is the Burgers vector, ν is the Poisson's ratio, and r_c is the dislocation core radius.

For Ag given μ = 30 GPa, b = 0.289 nm, ν = 0.37, r_L = 3.3 nm (calculated with L = 5.7 nm, as shown in Fig. 1h) and r_c = 1 nm, the right side of the equation and becomes 25 mJ/m^2, greater than 17 mJ/m^2. Therefore the formation of Frank loop is energetically favorable over a perfect loop in Ag and consequently a considerable amount of SFTs were formed in irradiated Ag films. Furthermore it was found that SFTs in various irradiated fcc metals (Ag, Au, Cu, Ni) are predominantly vacancy clusters [34, 35].

The evolution of defect density with dose can be divided into two stages: rapid increase in stage I, and saturation in stage II as shown in Fig. 1.2h. Stage I may arise from the formation of a large number of faulted loops during the initial stage of radiation. Defect density saturates in stage II because a balance between the defect generation (by radiation) and removal (by twin boundaries) rate was established in nt Ag. Defect density in fine nt Ag (t_{ave} = 8 nm) saturates at a level of 8 ×10^{22} m^{-3}, as compared to 1.6 × 10^{23}/m^{-3} in Ag with thick twins (t_{ave} = 70 nm) as shown by the dash line. Literature data on defect density of room temperature irradiated Ag are scarce. Kiritani *et al.* [17] showed the density of SFTs in Ag irradiated by neutron at a similar dose at 573K is ~ 1.5×10^{22} m^{-3}, and reduction of radiation temperature by 100K in Au (that has higher stacking fault energy and threshold displacement energy than Ag) can lead to an order of magnitude increase in defect density in Au. Also defect density in neutron irradiated Ni

and Cu at a similar dose level approaches 2-10 $\times$ 10^{23} m^{-3} at room temperature [36]. Ag has a lower stacking fault energy than Au, Cu and Ni, and hence it is anticipated that the density of SFTs in bulk Ag irradiated at room temperature to a similar dose will be much greater than that observed in nt Ag.
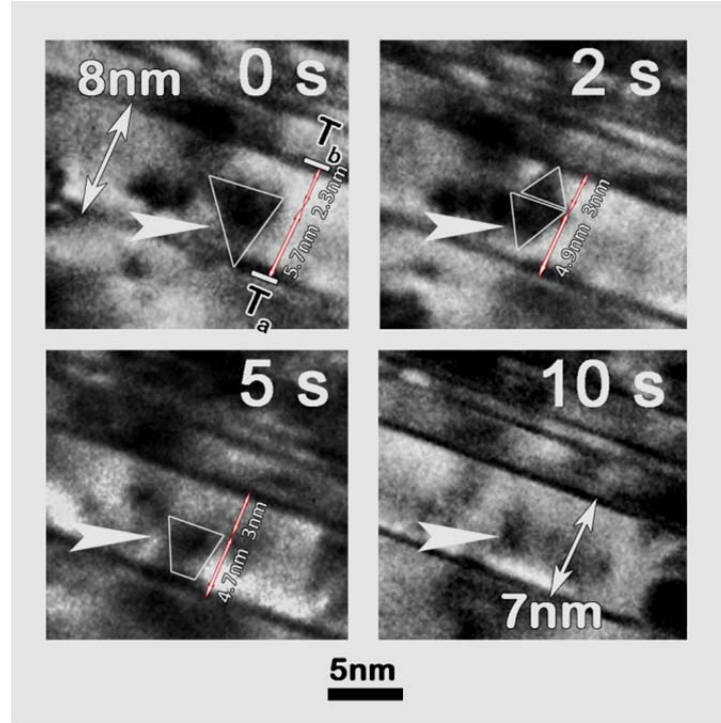

Figure 1.5 *In situ* observation of SFTs interacting with CTBs over a dose range of 0.075 - 0.081 dpa. The apex of a 5 nm SFT is in contact with CTB, T_a at 0 s. The SFT split into two smaller SFTs joint from their bases at 2 s. By 5 s, the upper SFT adjacent to T_b vanishes and the lower SFT is truncated from its tip. At 10 s, the SFT has a core barely discernible and the twin spacing shrinks by 1 nm.

SFTs, the predominant type of vacancy clusters in irradiated Cu, Ni, Ag and Au [34] in absence of noble gas, can expand (or shrink) by absorbing a vacancy (or an interstitial) or even collapse by consuming a sufficient number of interstitials [23]. Therefore, it is very important to note that a majority of SFTs in our study were actually annihilated through active interaction with twin boundaries as supported by several observations. First of all, the direct evidence of annihilation of SFTs via their frequent interactions with twin boundaries was captured. A series of video clips in Fig. 1.5 obtained from the *in situ* video show that the apex of a 5 nm SFT touched a CTB, T_a. The original SFT then split

into two smaller SFTs after 2 s. The upper SFT, whose apex contacted the upper CTB, T_b, disappeared by 5 s. Meanwhile the apex of the lower SFT was truncated by T_a. The truncated SFT nearly disappeared by 10 s. Comparison shows the twin spacing (separation distance between T_a and T_b) shrank from 8 to 7 nm, indicating that twin boundaries migrated during radiation from 0.075 to 0.081 dpa. Second, CTBs were severely distorted after interaction with SFTs as revealed by the formation of SFs along twin boundaries (Fig. 1.2f). Third, twin spacing has a significant influence on the density of SFTs, that is, the smaller the twin spacing, the lower the density of SFTs. Also, truncated SFTs were frequently observed adjacent to CTBs (the inset of Fig. 1.2c). The annihilation mechanisms of SFTs by twin boundaries are briefly discussed as follows.
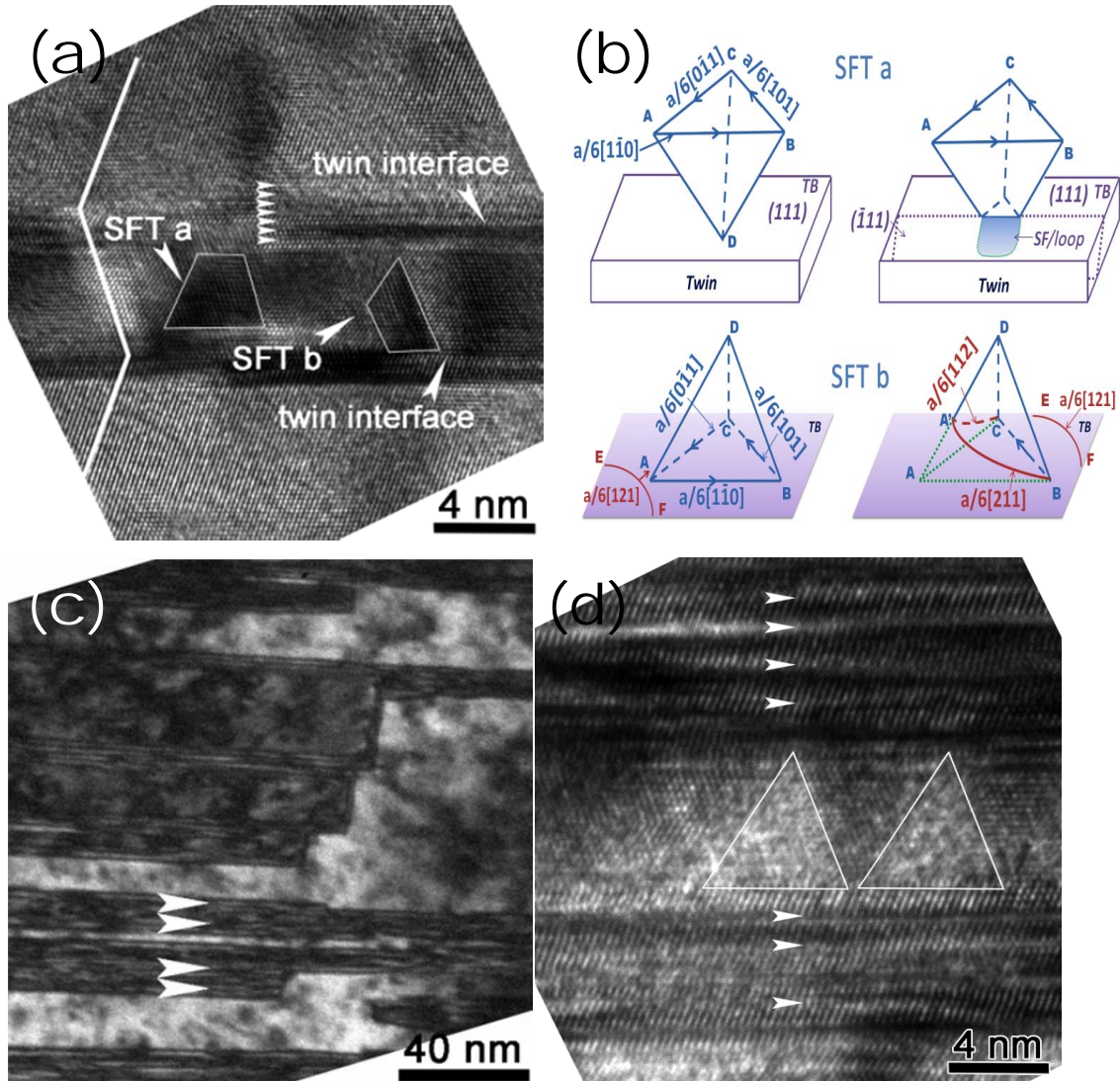
Figure 1.6 (a) HRTEM image of two truncated SFTs during their interactions with CTBs.

SFT-a was truncated from its apex, whereas SFT-b was destructed from its base. (b) Schematics of two types of interactions between SFTs and twin boundaries corresponding to the two cases in (a). The removal of SFT initiated from its apex (in contact with a twin boundary) results in the formation of dislocation loops on {111} plane in the twin lattices. In the lower case, the interaction of a mobile partial with stair rod dislocations, AB and AC, results in two new mobile partials that can migrate on the surface of SFT and lead to its decomposition. (c) Stacking faults along twin boundaries in irradiated nt Ag (t_{ave} = 8 nm) were induced by SFT-twin boundary interactions as shown by cross-sectional TEM micrograph. (d) HRTEM micrograph showing the formation of groups of stacking faults in irradiated thin nt Ag (up to 1 dpa).

The HRTEM image in Fig. 1.6a shows two truncated SFTs adjacent to CTBs. SFT-a is truncated from its apex and the destruction of SFT-b starts from its base in contact with a lower CTB. Two possible annihilation mechanisms are illustrated in Fig. 1.6b. Atomistic simulations [23, 37] have shown when a mobile twin boundary reached an SFT from its apex as depicted in the upper case in Fig. 1.6b, the SFT-twin boundary interaction transforms the {111} apex of SFT in matrix to a smaller {100}$_T$ tetrahedron residing temporarily within the twin lattice which then collapses rapidly into a partial loop on the {111} plane in the twinned crystal. SFs also form next to the twin boundary. Continuous migration of the twin boundary towards the SFT leads to the further consumption of the truncated SFT. SFs absorb vacancies supplied by the SFT and continuously expand along the twin boundary. On the other hand, when the SFT is approached by a mobile twin boundary from its base as shown in the lower case of Fig. 1.6b, a mobile Shockley partial, a/6[121], migrating along the twin boundary could interact with stair-rod dislocations, AB (a/6[1$\bar{1}$0]), AC (a/6[0 1 $\bar{1}$]) and BC (a/6[101]), at the base of SFT. The interactions with AB and AC lead to new mobile Shockley partials (a/6[211] and a/6[112])) whose migration on ABD and ACD planes of the SFT can result in the unfaulting of Frank loops [18]. The two scenarios predicted by MD simulations are consistent with our *in situ* observations. Note that intensive SFT-twin boundary interactions result in high density SFs, adjacent to twin boundaries as shown in Fig. 1.6c and d. Foregoing discussions strongly suggest that twin boundaries play a remarkable

role during the removal of radiation induced SFTs.

Observation of CTB and ITB motion

What MD simulations did not capture though is that the continuous interactions led to the formation of multiple SFs along twin boundaries, and thus twin boundary appears 'thicker' after radiation. A thicker twin boundary increases the probability of its interaction with SFTs. In the fine nt Ag specimen, the area fraction of irradiation induced stacking faults is estimated to be ~ 10% using a method shown in Fig. 1.7.
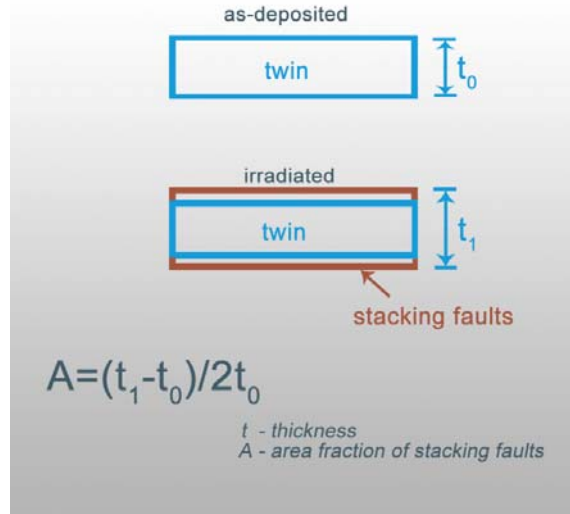
Figure 1.7 Schematics of radiation induced stacking faults adjacent to twin boundaries. The inset equation is used to quantify the area fraction of stacking faults.

The kinetic interactions of SFTs with twin boundaries may also be enhanced by several other means. First, continuous growth of SFTs in size (before reaching a saturation dimension) coupled with smaller t_{ave} may expedite their interactions. Second, twin boundaries may be mobile. *In situ* nanoindentation studies and MD simulations have shown that ITBs in nt Cu can migrate rapidly under stress or annealing through the movement of mobile Shockley partials [28, 29, 31]. The migration can lead to detwinning. However, there is no prior evidence on radiation induced migration of twin boundaries.

We have captured frequent migration of twin boundaries during *in situ* radiation

studies. TEM micrographs in Fig. 1.8 show an ITB in thick nt Ag (t_{ave}= 70 nm) migrated by 5.7 nm during radiation from 0.5 to 1 dpa. Another example of such migration in irradiated fine nt Ag (t_{ave} = 8 nm) is shown in Fig. 1.9 obtained from *in situ* video. Area A consists of several ITBs as outlined and labeled as T1 to T5. Snap shots were taken over the dose of ~ 0.07 - 0.11 dpa. As seen in the 0 - 15 s frames, the ITB T1 and T2 aligns well with each other. But T2 is completely removed by 25 s and a new ITB T3 forms and aligns with T1. By 35 s, T3 is separated from T4 (evolved from T1) and forms inclined ITBs. By 55 s, T3 migrates leftward by 2 nm and finally aligns with ITB T5. Two factors may lead to the formation and migration of new ITBs. First, the destruction of SFTs by CTBs leads to the formation of multiple stacking faults (as shown in Fig. 1.6c and d). ITBs are consisted of groups of Shockley partials, one on each atomic plane [31]. The summation of Burgers vectors of three Shockley partials on three adjacent planes is zero [29]. Under stress, sharp ITBs can transform into diffuse boundaries (groups of wide stacking faults). It may be energetically favorable for the groups of stacking faults (formed by destruction of SFTs) to evolve into wide ITBs. Second, ITBs are sources for Shockley partials and sinks for point defects. Radiation induced defect clusters, including SFTs, may attract or repel partials inside ITBs and lead to their migration. Significant mobility makes twin boundaries an attractive candidate for removing radiation induced SFTs as well as other defects. The physical mechanisms and details of radiation induced twin boundary migration require atomistic simulations. Although twin boundaries can actively remove SFTs in irradiated metallic materials, special precaution shall be applied as twin boundaries may become less effective in removing He stabilized defects, such as He bubbles as shown previously [30].

Other than twin boundaries, mobile dislocations may also interact with SFTs. The same *in situ* video also reveals the emission and migration of a dislocation as outlined in the box B in a series of snap shots in Fig. 1.9. The dislocation in box B is emitted from an ITB at the beginning of the video during radiation and it evolves during continuous radiation. The migration of the dislocation is confined within the twins by attaching its upper end to the original ITB. The dislocation continues to propagate until it finally reaches the lower CTB, where a dislocation loop forms by 55 s. Propagation of mobile dislocations may also contribute to the removal of some radiation induced defects as

shown previously [22].

In conclusion, *in situ* radiation of nt Ag reveals the removal of SFTs through their frequent interactions with twin boundaries. At least two types of interaction mechanisms arising from abundant mobile Shockley partials or twin boundaries are responsible for the destruction of SFTs. Thus the *in situ* radiation studies validate predictions by atomistic simulations. Smaller average twin spacing leads to lower density of SFTs and dislocation loops, and the density of SFTs in nt Ag is much lower than that in its bulk counterpart. Radiation also induces remarkable migration of coherent and incoherent twin boundaries that may assist the removal of radiation induced defects.

Reference

[1] S.J. Zinkle, L.L. Snead, Journal of Nuclear Materials, 225 (1995) 123-131.

[2] B.N. Singh, A.J.E. Foreman, Philosophical Magazine, 29 (1974) 847-858.

[3] B.N. Singh, Philosophical Magazine, 29 (1974) 25-42.

[4] B.N. Singh, A. Horsewell, P. Toft, D.J. Edwards, Journal of Nuclear Materials, 224 (1995) 131-140.

[5] A.H. King, D.A. Smith, Philosophical Magazine A, 42 (1980) 495-512.

[6] R.W. Grimes, R.J.M. Konings, L. Edwards, Nat Mater, 7 (2008) 683-685.

[7] K.Y. Yu, Y. Liu, C. Sun, H. Wang, L. Shao, E.G. Fu, X. Zhang, Journal of Nuclear Materials, 425 (2012) 140-146.

[8] M. Hiratani, H.M. Zbib, B.D. Wirth, Philosophical Magazine A, 82 (2002) 2709-2735.

[9] Y.N. Osetsky, D. Rodney, D.J. Bacon, Philosophical Magazine, 86 (2006) 2295-2313.

[10] N.M. Ghoniem, B.N. Singh, L.Z. Sun, T. Díaz de la Rubia, Journal of Nuclear Materials, 276 (2000) 166-177.

[11] X.-M. Bai, A.F. Voter, R.G. Hoagland, M. Nastasi, B.P. Uberuaga, Science, 327 (2010) 1631-1634.

[12] X. Zhang, N. Li, O. Anderoglu, H. Wang, J.G. Swadener, T. Höchbauer, A. Misra, R.G. Hoagland, Nuclear Instruments and Methods in Physics Research Section B: Beam Interactions with Materials and Atoms, 261 (2007) 1129-1132.

[13] E.G. Fu, J. Carter, G. Swadener, A. Misra, L. Shao, H. Wang, X. Zhang, Journal of Nuclear Materials, 385 (2009) 629-632.

[14] E.G. Fu, A. Misra, H. Wang, L. Shao, X. Zhang, Journal of Nuclear Materials, 407 (2010) 178-188.

[15] Q.M. Wei, N. Li, N. Mara, M. Nastasi, A. Misra, Acta Materialia, 59 (2011) 6331-6340.

[16] M.J. Demkowicz, R.G. Hoagland, J.P. Hirth, Physical Review Letters, 100 (2008) 136102.

[17] M. Kiritani, Materials Chemistry and Physics, 50 (1997) 133-138.

[18] S.J. Zinkle, L.E. Seitzman, W.G. Wolfer, Philosophical Magazine A, 55 (1987) 111-125.

[19] G. Was, Fundamentals of Radiation Materials Science, 2007.

[20] B.P. Uberuaga, R.G. Hoagland, A.F. Voter, S.M. Valone, Physical Review Letters, 99 (2007) 135501.

[21] B.N. Singh, S.I. Golubov, H. Trinkaus, D.J. Edwards, M. Eldrup, Journal of Nuclear Materials, 328 (2004) 77-87.

[22] Y. Matsukawa, S.J. Zinkle, Journal of Nuclear Materials, 329–333, Part B (2004) 919-923.

[23] M. Niewczas, R.G. Hoagland, Philosophical Magazine, 89 (2009) 727-746.

[24] L. Lu, Y. Shen, X. Chen, L. Qian, K. Lu, Science, 304 (2004) 422-426.

[25] K. Lu, L. Lu, S. Suresh, Science, 324 (2009) 349-352.

[26] D. Bufford, H. Wang, X. Zhang, Acta Materialia, 59 (2011) 93-101.

[27] X. Zhang, A. Misra, H. Wang, T.D. Shen, M. Nastasi, T.E. Mitchell, J.P. Hirth, R.G. Hoagland, J.D. Embury, Acta Materialia, 52 (2004) 995-1002.

[28] L. Liu, J. Wang, S.K. Gong, S.X. Mao, Physical Review Letters, 106 (2011) 175504.

[29] J. Wang, N. Li, O. Anderoglu, X. Zhang, A. Misra, J.Y. Huang, J.P. Hirth, Acta Materialia, 58 (2010) 2262-2270.

[30] M.J. Demkowicz, O. Anderoglu, X. Zhang, A. Misra, Journal of Materials Research, 26 (2011) 1666-1675.

[31] J. Wang, O. Anderoglu, J.P. Hirth, A. Misra, X. Zhang, Applied Physics Letters, 95 (2009) 021908-021903.

[32] J. Silcox, P.B. Hirsch, Philosophical Magazine, 4 (1959) 1356-1374.

[33] J.P. Hirth, J. Lothe, McGraw-Hill, New York, (1967).

[34] L. Jenkins, A. Kirk, Characterization of Radiation Damage by Transmission Electron Microscopy, Institute of Physics Pub., 2001.

[35] S. Kojima, S.J. Zinkle, H.L. Heinisch, Journal of Nuclear Materials, 179–181, Part 2 (1991) 982-985.

[36] B.N. Singh, S.J. Zinkle, Journal of Nuclear Materials, 206 (1993) 212-229.

[37] N. Nita, R. Schaeublin, M. Victoria, R.Z. Valiev, Philosophical Magazine, 85 (2005) 723-735.

[38] U.L. J.F. Ziegler, J.P. Biersack, , <http://www.srim.org/>.

II. 2. Comparisons of radiation damage in He ion and proton irradiated immiscible Ag/Ni nanolayers (Published in Journal of Nuclear Materials, 2013)

Highly energetic particles, including protons and neutrons, in nuclear reactors initially create equal number of interstitials and vacancies in irradiated metallic materials. These point defects later evolve into defect clusters due to various reasons. For instance, preferential sinks, such as dislocations, can trap one type of the defects preferentially and leave the other type supersaturated, resulting in defect clusters. Defect clusters lead to degradation of swelling and radiation hardening, which is typically accompanied by embrittlement [1-3]. Therefore it is of great significance to design materials with improved radiation tolerance via removal of those defect clusters *in situ* during radiation. Next generation nuclear reactors require structural materials with superior radiation tolerance, that is to sustain more than hundreds of displacements-per-atom (dpa) over 80 years [3]. In order to reach such a high operational standard, materials with a large amount of defect sinks, such as dislocations, grain boundaries (GBs) and phase boundaries, are needed [4]. These sinks must have the ability to annihilate radiation induced defects and their clusters and consequently suppress radiation hardening and embrittlement [1]. Meanwhile these defect sinks must be stable themselves against radiation at high temperatures [5-8].

Numerous attempts have been made to explore radiation tolerance of nanostructured metals. Zinkle and Singh proposed grain size dependent nucleation of defects based on the observation of grain boundary denuded zone (free of defect clusters by GBs) in neutron irradiated alloys [9-11]. Bai *et al.*, through atomistic simulations,

showed that interstitials were first loaded into the grain boundaries; followed by their emission (upon super saturation) back to (unloaded) the interior of grain to annihilate vacancies [12]. Sun *et al.* studied Fe-Cr-Ni alloys with an average grain size of ~ 400 nm, processed by equal channel angular pressing (ECAP) and observed significant improvement of radiation tolerance [13]. Yu *et al.* revealed a reduction of helium bubble density with decreasing grain size in nanocrystalline (NC) Fe films prepared by magnetron sputtering [14]. Wang *et al.* showed that NC TiN has superior radiation tolerance against He ion irradiation[15]. Odette *et al.* have reviewed the significance of metal/oxide phase boundaries in nanostructured ferritic steels with oxide nanoparticles on radiation tolerance of steels [16].

Multilayers are attractive systems to examine the impact of layer interfaces on removal of radiation induced defects, since nanolayers have significant interfacial areas that can act as defect sinks [8, 17]. Modern nanomanufacturing techniques, such as magnetron sputtering, enable flexible construction of various types (coherent vs. incoherent) of interfaces as well as accurate control of the thickness of individual layers. Cu/Nb [8] and Cu/V [5, 7] were among the first studied systems. Significant layer thickness dependent reductions of both helium bubble density and radiation hardening were reported. In Cu/V system, smaller layer thickness leads to enhanced radiation tolerance (less hardening and lower bubble density). Using molecular dynamics (MD) simulations, Demkowicz *et al.* showed that at the Cu/Nb interface two K-S orientation relationships can convert alternatively by absorbing a vacancy or an interstitial and form jogs [18]. Such a process makes the Cu/Nb interface inexhaustible sinks for radiation induced defects. Other metallic multilayers, such as Cu/W [19, 20], Ag/V [21], Ti/Ta [22], Fe/W [6] and Al/Nb [23]   have also been investigated that showed the nucleation and migration of defects will be considerably affected once the individual layer thickness, h, reduced down to several nanometers. Considering He bubbles as barriers for the propagation of dislocations in multilayers, Wei *et al.* modified the confined layer system model to understand the He bubble induced radiation hardening [21]. Among multilayers investigated thus far, immiscible systems appeared to have better radiation tolerance overall, primarily because of the stability of interface against radiation induced intermixing. Meanwhile many of the immiscible multilayer systems investigated to date

have fcc/bcc type of interfaces with typically K-S orientation relationship. Little attention has been paid to immiscible systems with fcc/fcc interfaces. We report in this study on the radiation response of immiscible Ag/Ni multilayers which were irradiated by He ions and protons to a similar damage level. Comparison of defect nature and hardening provides important insights on the mechanism of radiation damage in this immiscible multilayer system.

Ag/Ni multilayer films with thickness of ~1-4 μm were synthesized on HF etched single crystal silicon (111) substrates by using DC magnetron sputtering technique at room temperature. Ag and Ni layers within the films have equal layer thickness, varying from 1 to 200 nm. The purity of the targets is both 99.95%. A base pressure of 6.7×10^{-6} Pa was reached before depositions and the Ar partial pressure during sputtering was ~ 0.5 Pa. The films with various h were irradiated together at room temperature using 100 keV He ions and 180 keV protons, respectively. A total fluence of 6×10^{20} ions/m^2 was achieved for He radiation and 6×10^{21} ions/m^2 for proton radiation. The temperature rise of the sample stage was ~ 50°C during implantation. Base pressure in the ion implanter was 4×10^{-5} Pa. The microstructure of Ag/Ni multilayers was characterized by a Bruker-AXS D8 advanced Bragg-Brentano X-ray powder diffractometer with Cu $\lambda_{K\alpha1}$= 0.154056 nm. The cross-sectional transmission electron microscopy (XTEM) samples were mechanically ground and polished, followed by dimpling and low energy Ar ion milling. XTEM samples were then examined by a 200 kV JEOL 2010 transmission electron microscope equipped with a Gatan SC1000 ORIUS CCD camera. During TEM sample preparation Ar ion milling can induce damage in the form of Ar bubbles and amorphization. These artifacts were typically observed in a narrow region, within 20 nm from the edge of TEM specimens (near the center of a hole in specimens). Appropriate selection of ion milling parameters (low energy and low angle), can effectively reduce the ion milling induced damage [5, 7, 24]. The indentation hardness and modulus of the films were measured from an average of 12-15 indents at different indentation depths, using instrumented nanoindentation technique by a Fischerscope HM2000XYp micro/nanoindenter with a Vickers indenter tip. The loading rate was kept at 10 mN/s and indentation depth was set to let the diamond tip penetrate into at least two bilayers, ranging from 75 nm at small layer thickness to 600 nm at large h (the total thickness of these films were ~ 4 μm). The

stopping and range of ions in matter (SRIM) was used to simulate the profiles of He and proton concentration and displacements in multilayers as a function of depth [25]. The profile, as shown in Fig. 2.1a, implies the He concentration reaches a peak value of ~ 4 at. % at a depth of ~ 340 nm. The peak radiation damage is approximately 4 displacements-per-atom (dpa) at a depth of ~ 300 nm and the irradiated region extends to a maximum depth of ~ 480 nm beyond the surface. Damage and He concentration profiles of proton irradiation (Fig. 2.1b) show a peak damage of ~ 4 dpa at the depth of ~ 800 nm and peak H concentration at a slightly deeper level. The radiation damage region extends to ~ 1.2 μm. The average dpa in both He and proton irradiated multilayers is similar.
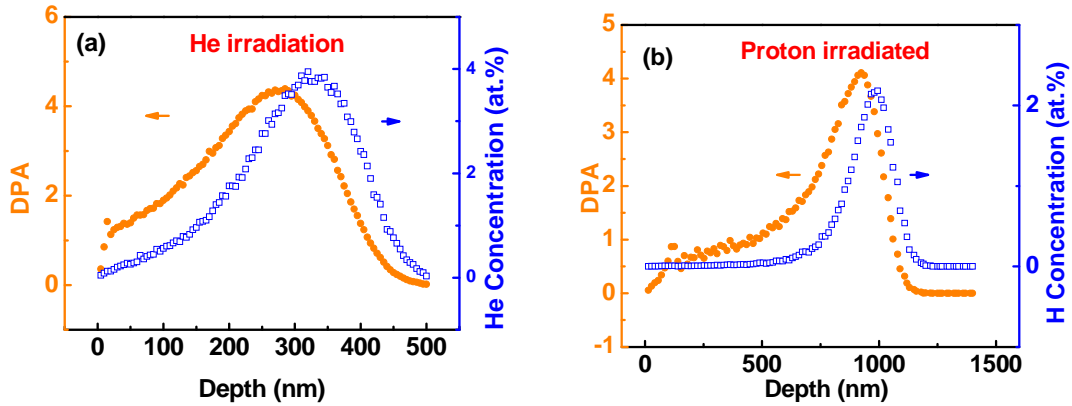
Figure 2.1 Radiation damage profile of $Ag_{50}Ni_{50}$ alloys irradiated by (a) 100keV He, to a fluence of 6×10^{16} cm^{-2} and (b) 180keV proton, to a fluence of 6×10^{17} cm^{-2}, run by SRIM simulation. Both types of radiation reached a damage baseline at ~ 1dpa.
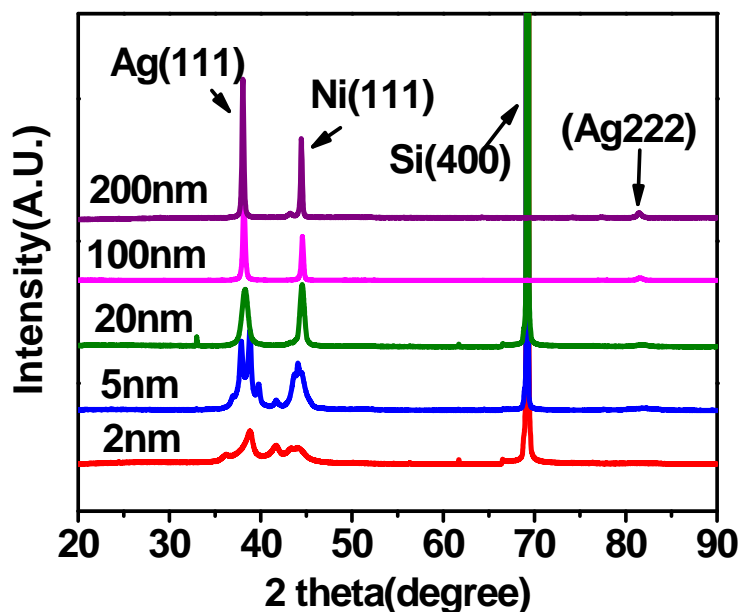
Figure 2.2 XRD profiles of as-deposited Ag/Ni multilayers show polycrystalline films with Ag and Ni (111) texture. Superlattice peaks were detected in film with individual layer thickness of 5 nm or less.
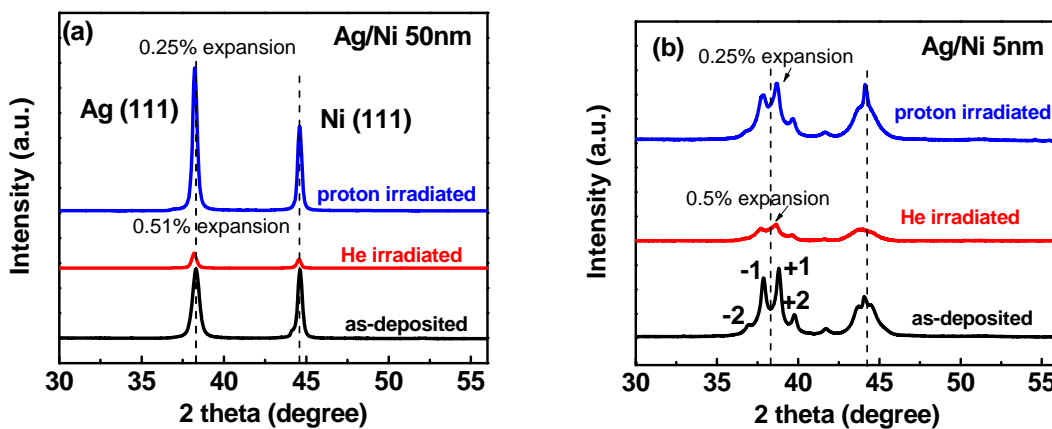

Figure 2.3 Comparison of XRD profiles between as-deposited, He irradiated and proton irradiated (a) Ag/Ni 50 nm and (b) Ag/Ni 5 nm multilayers. Lattice distortions are indicated by percentage. A reduction of peak intensity is observed in He irradiated films.

Microstructure of as-deposited and irradiated Ag/Ni multilayers

XRD patterns of as-deposited Ag/Ni multilayers are shown in Fig. 2.2. Distinct Ag and Ni (111) peaks were observed at larger h, 20 ~ 200 nm, while at smaller layer thickness, 2 ~ 5 nm, satellite peaks arose due to super lattice structure [26]. With decreasing layer thickness, Ag and Ni peaks shifted towards each other due to the constraint along layer interface. XRD profiles in Fig. 2.3 show drastic difference between He and proton irradiated Ag 50 nm / Ni 50 nm (referred to as Ag/Ni 50 nm afterwards) and Ag/Ni 5 nm multilayers. After He radiation, the peak density of Ag and Ni (111) dropped drastically accompanied with a peak shift to lower angles (indication of out-of-plane lattice expansion), whereas there was only minor intensity variation for proton-irradiated specimens. Average out-of-plane lattice expansions of Ag (111) for He and proton irradiated films were estimated to be 0.5 % and 0.25 %, respectively.
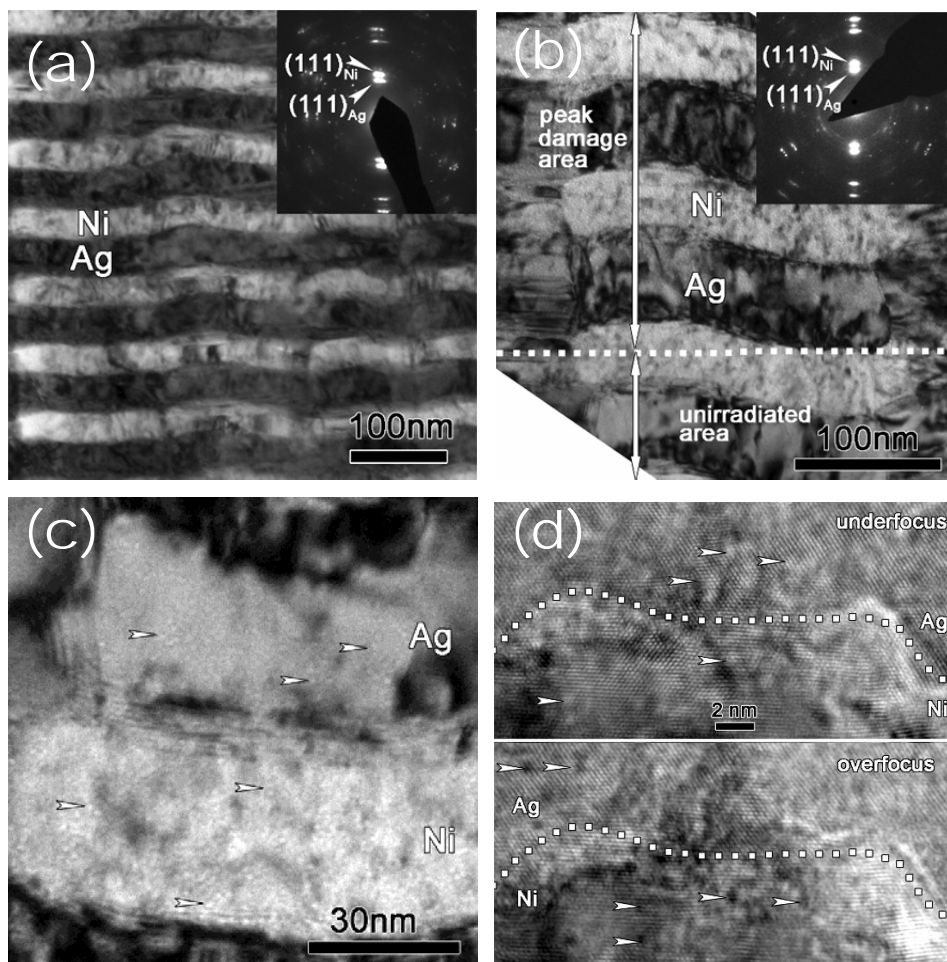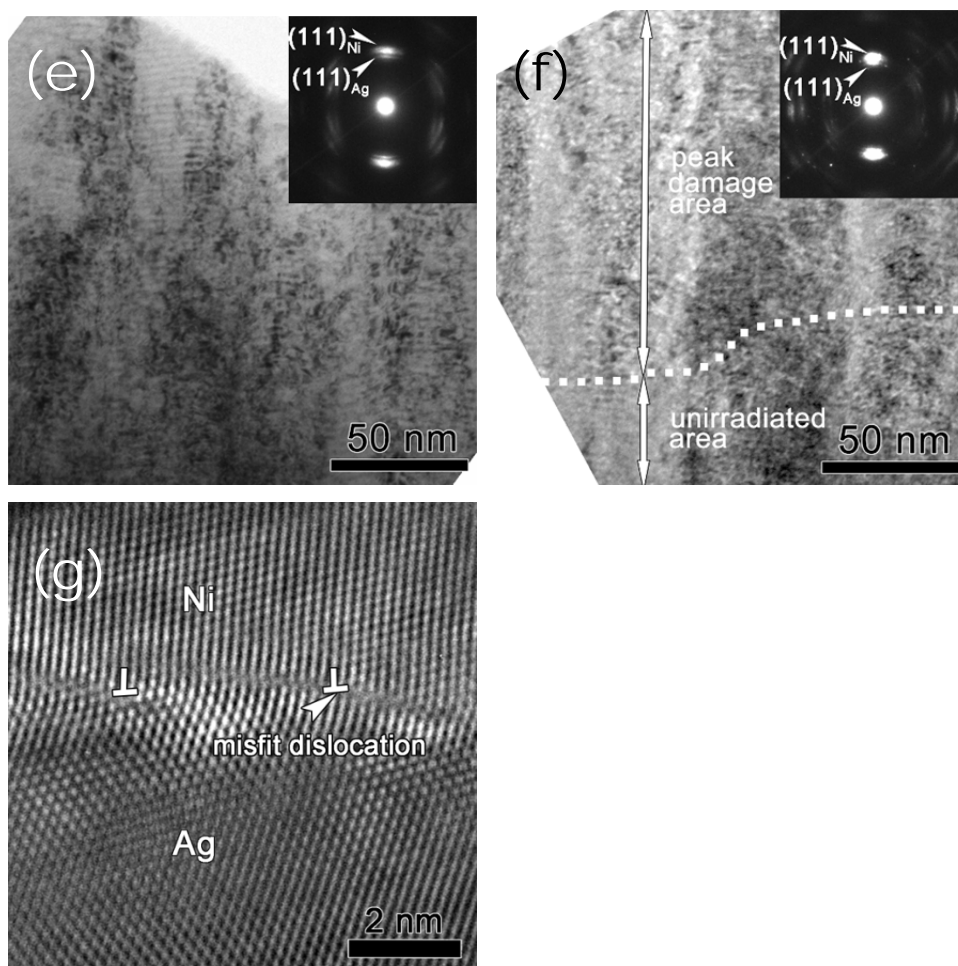
Figure 2.4 XTEM micrographs of various multilayers subjected to He ion irradiations. (a) As-deposited Ag/Ni 50 nm film had clear interface and Ag and Ni (111) texture. (b) Interfaces remained stable after He ion irradiations. High density He bubbles were observed in both Ag and Ni (c), and confirmed in defocused HRTEM micrograph in (d). (e) as-deposited Ag/Ni 2 nm film had superlattice diffractions as shown by the inserted SAD pattern, and He bubbles were observed in He ion irradiated specimens (f). (g) showing high density misfit dislocations at the Ag/Ni interface, with an average spacing of ~ 3.5 nm.

XTEM micrograph of as-deposited Ag/Ni 50 nm film (Fig. 2.4a) shows that both constituents had polycrystalline structure and grain sizes were 5 times larger than h. Inserted selected area diffraction (SAD) pattern verifies that the films were highly textured with a strong (111) texture. The interfaces between Ag and Ni were slightly wavy but sharp.

After He ion irradiation (Fig. 2.4b) high density He bubbles (white dots) were observed in the peak damage area. A higher magnification image in Fig. 2.4c revealed the formation of He bubbles in both Ag and Ni layers. High resolution TEM (HRTEM) images captured at different focus conditions in Figure 6.7d show that He bubbles appeared white at under focus (- 400 nm) condition and black when over focus (400 nm) was applied. The bubble size in both constituents was ~ 1.2 nm. Bubbles agglomerated at grain boundaries and layer interfaces. Black dots, which were also observed in under focused condition, could be Frank dislocation loops as well as other defect clusters. No bubbles were detected beyond ~ 550 nm underneath the film surface. As-deposited and He irradiated Ag/Ni 2 nm films were also investigated as shown in Fig. 2.4e and f. Similar to 50 nm specimen, He bubbles are found in Ag/Ni 2 nm film. The bubble size was ~ 1.3 nm.
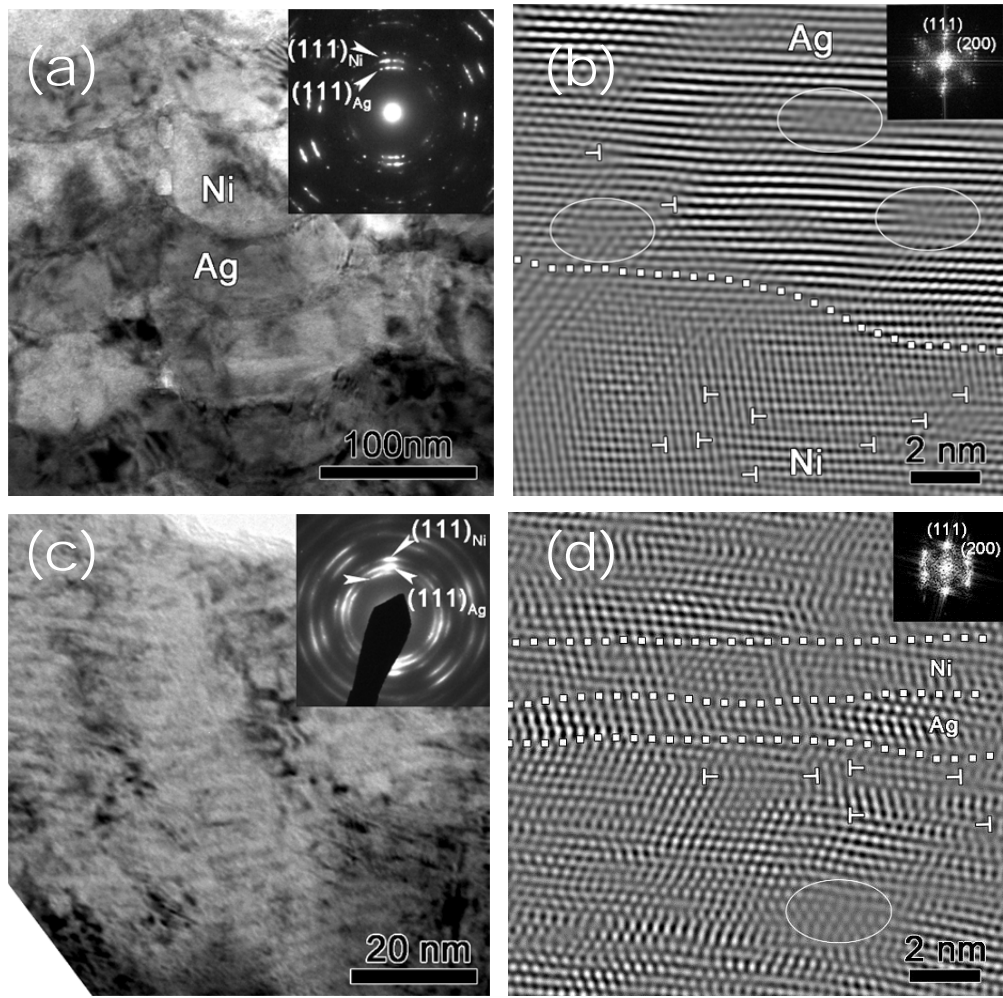
Figure 2.5 XTEM micrographs of (a) proton irradiated Ag/Ni 50 nm at low magnification and (b) corresponding filtered HRTEM image. Vacancy loops were identified by circles, whereas interstitial loops were labeled by pairs of dislocations. (c) Proton irradiated Ag/Ni 2 nm film had stable layer interface with strong fiber texture. (d) The corresponding filtered HRTEM image displayed dislocation loops. Dotted lines represent layer interfaces.

TEM micrographs of proton irradiated Ag/Ni 50 nm and Ag/Ni 2 nm films are shown in Fig. 2.5. Layer structure remained intact after radiation. No evident defect clusters were detected at low magnification (Fig. 2.5a and c). Filtered high resolution images reveal the nature of defects as dislocation loops, as seen in Fig. 2.5b and d. Interstitial loops are indicated by pairs of edge dislocations while vacancy loops are identified by circles. Lattice distortions were observed surrounding loops.
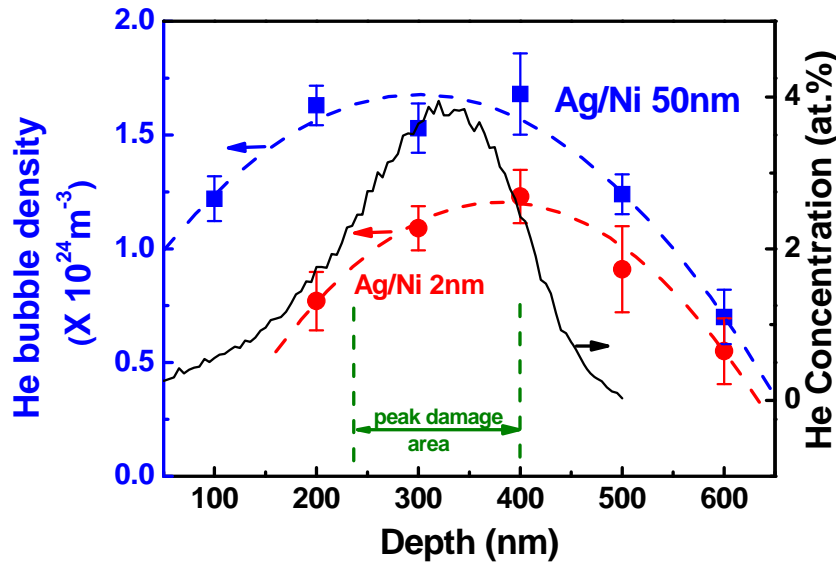
Figure 2.6 Bubble density evolution as a function of depth for He ion irradiated Ag/Ni film with individual layer thickness of 50 nm (square) and 2 nm (circle), respectively. The trend agrees well with the superimposed SRIM results of He concentration (solid line). The Ag/Ni 2 nm film showed lower peak density and larger threshold depth where bubbles can be detected.

He bubble profile and hardness evolution

He bubble density at different depth was examined via extensive XTEM studies. The average TEM foil thickness was measured to be ~ 120 nm using Kossel-Mollenstedt fringes. The bubble density increased first and approached a peak value at a depth of ~ 350 – 400 nm, and then continued to drop till a depth of ~ 600 nm, as plotted in Fig. 2.6. In comparison, the peak bubble density in Ag/Ni 2 nm film is ~ 25% lower than that in the Ag/Ni 50 nm film, and peak damage region in the Ag/Ni 2nm film is narrower. Also, the threshold He concentration to detect bubbles in Ag/Ni 2 nm film is ~ 1 at.% as compared to ~ 1 at.% in Ag/Ni 50 nm film. The depth of peak bubble density for both systems is somewhat close to peak He concentration as shown by the superimposed SRIM simulation result (solid line) in the same figure.
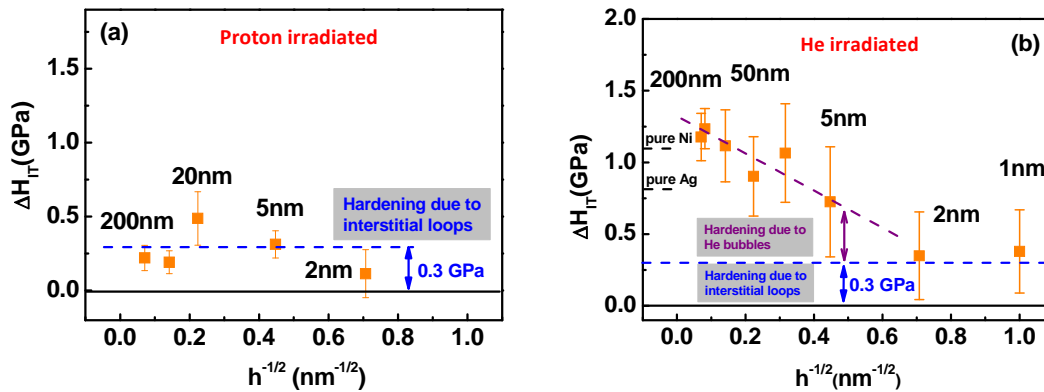
Figure 2.7 Hardening induced by (a) proton and (b) He ion irradiation, as a function of layer thickness. No particular hardening trend was detected in proton irradiated films given that similar hardness increase was found in all films. And this ~ 0.3 GPa hardening may be attributed solely to loops, as well as other undetectable defect clusters. Thus we are able to isolate bubble hardening observed in (b) by subtracting a baseline of 0.3 GPa, as shown by the area between two dash lines.

In proton irradiated Ag/Ni films, radiation induced hardening probed by nanoindentation was found to be nearly constant as ~ 0.3 GPa, as indicated in Fig. 2.7a, independent of layer thickness. On the other hand, hardening can be divided into two regimes for He irradiated films. Radiation hardening at large layer thickness (100 and 200

nm) was about 1.3 GPa, as compared to ~ 0.7 GPa of polycrystalline Ag and ~ 1.2 GPa of polycrystalline Ni. Using the rule of mixture, the average hardening of Ag/Ni is ~ 1 GPa. As seen in Fig. 2.7b, radiation hardening first decreased with decreasing h and then reached a minimum value of ~ 0.3 GPa at 1 – 2 nm.   Hardening mechanism will be discussed in the following section.

Lower bubble density was revealed in films with smaller h. This phenomenon can be explained by the absorption of both vacancies and interstitials at the immiscible layer interface. It has been shown by MD simulations that there exist two types of interfacial relationship in Cu/Nb multilayers, referred to as K-S$_1$ and K-S$_2$ [18]. Each type of interface can convert to the other one by absorbing an interstitial or a vacancy and correspondingly jogs form at the interfaces. Such a mechanism in immiscible fcc/bcc systems makes the interfaces inexhaustible sinks for point defects [8, 18]. Modeling on interfacial evolution under radiation is still lacking for fcc/fcc type of immiscible systems, such as Ag/Ni. The Ag/Ni interface is likely to absorb vacancies and interstitials and promotes their recombination at the interface as well. Additionally large lattice mismatch at Ag/Ni interface (by ~ 15 %) creates abundant misfit dislocations, which can also act as sinks and contribute to the deduction of defect clusters. Multilayers with smaller h will clearly provide more interfaces, and hence are more effective during absorbance and removal of radiation induced point defects. Similar size dependent reduction of bubble density has also been observed in other He ion irradiated systems, including Cu/V and Fe/W multilayers [5-7].

We now attempt to estimate the pressure built-up by He in He bubbles. The equilibrium bubble pressure can be estimated by [27]

$$P = 2\gamma / R \tag{1},$$

where P is the bubble pressure, γ is the surface energy, and R is the radius of bubble. From TEM images in Fig. 2.4, little difference in bubble size was found either in different layers (Ag and Ni) or in films with different layer thickness (2 and 50 nm). Therefore by taking an average bubble radius of $R = 0.6$ nm, and using $\gamma_{Ag} = 1.25$ J/m^2 and $\gamma_{Ni} = 2.40$ J/m^2 [28], we estimate the bubble pressure to be ~ 4.2 GPa in Ag and ~ 8.0 GPa in Ni. The actual pressure in Ag/Ni should fall somewhere in between this range.

By using the equation of state   for solid state He [29], we estimate the atomic

density of He, ρ, to be between ~ 133 and 109 atoms/nm^3 in Ag and Ni respectively. In what follows we can estimate the number of He atoms (N) in each bubble by using $N = 4\pi r^3 \rho/3$. Therefore we derive ~ 120 atoms/bubble for Ag and 98 atoms/bubble in Ni. If we assume that all He atoms were confined in bubbles and take Ag atomic density as 58 atoms/nm^3, the bubble density in Ag can be estimated as $2\% \times 58/120 = 9.6 \times 10^{24}$ m^{-3}, and similarly in Ni it shall be 18.6×10^{24} m^{-3}. These numbers are much greater than experimentally observed density as shown in Fig. 2.6. The large discrepancy implies that a large amount of the helium resided in matrix or was trapped by other sinks.

If the bubbles were in equilibrium states, bubble size in Ag should be much larger than that in Ni as observed in Ag/V multilayer [21]. However, negligible difference in bubble size was found in this case. Such discrepancies can be explained in several aspects. First, the He ion fluence used in this study is half of that in Ag/V. It has been known that He bubble will exhibit dramatic growth once the He concentration reaches a certain limit. Thus it is likely that the He fluence in our study is under the bubble growth limit, and continuous implantation of He ions might induce apparent bubble growth eventually. Second, the misfit dislocation spacing reported in literature is ~ 5 nm as compared to ~ 3.5 nm in our case as shown in Fig. 2.4g. Misfit dislocations can act as effective sinks to promote annihilation of defects, as well as trapping He atoms, resulting in less He stored in bubbles. Third, V in Ag/V system, which is bcc structure, has a lower packing factor (68%) and more vacancy sites per cubic cell. So He atoms in V have more sites to stay instead of aggregating into bubbles, forming a biased distribution of He atoms between Ag and V layers, resulting in more He in Ag layers. However, Ag and Ni share the same atomic packing factor (74%), as well as equal vacancy sites per cubic cell since they are both fcc structure. Thus He concentration bias is less likely to happen.

For proton irradiated specimens, it is very challenging to examine the density of defect clusters as there were much less detectable defects comparing to those in He irradiated multilayers. However, through HRTEM images, we were able to identify interstitial and vacancy loops. As shown in Fig. 2.5b, there appeared to be more vacancy loops in Ag and more interstitial loops in Ni. There are several aspects to be considered to explain such a difference. First, a Ag atom has larger atomic radius than Ni, and thus Ag interstitials are less mobile. Poor mobility of Ag interstitials prohibits rapid

recombination process and leaves vacancy loops faulted. Second, Ag has a much lower stacking fault energy (17 mJ/m^2) than Ni (120 mJ/m^2) [30]. Stacking faults, which are primarily vacancy loops, are more likely to form in Ag. In heavy ion irradiated fcc metals, it has been found that the radius of stacking fault tetrahedra is inversely proportional to its stacking fault energy (γ_{SFE}), as shown below [31].

$$\gamma_{SFE} = \frac{\mu b^2}{3\pi r_L}\left(\frac{2-\nu}{2(1-\nu)}\right)\ln\left[\frac{4r_L}{r_c}-2\right] \qquad (2),$$

where r_L is the loop radius, μ is the shear modulus, b is the Burgers vector, ν is the Poisson's ratio, and r_c is the size of dislocation core. Third, Ag has greater lattice parameter than Ni. A compressive (tensile) stress might develop along interface in Ag (Ni). The compressive stress state in Ag favors the formation of vacancy loops, and correspondingly interstitial loops will help to relieve tensile stress in Ni layers.

When comparing the magnitude of lattice distortion between He and proton irradiated films, He bubbles apparently introduce more significant distortion to the crystal structure of Ag/Ni (as evidenced by large suppression of XRD peak intensity). In contrast, proton induced damage, even at the same dpa level, has little influence on peak intensity.
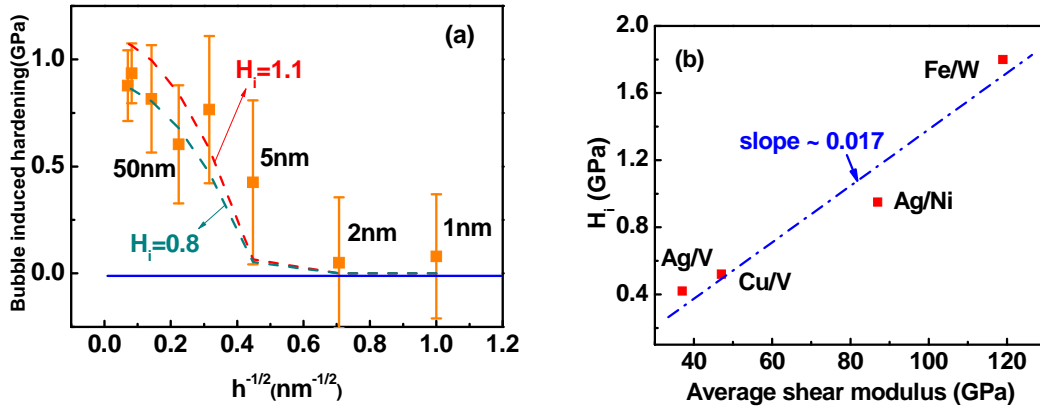
__Mechanism of irradiation hardening__

Figure 2.8 (a) Comparison of experimental data (squares) and modified CLS model (dash lines). Hardness data were obtained from Fig. 7b by subtracting a baseline of 0.3 GPa. Details of the model can be found in the discussion section of this study. (b) H_i as a function of average shear modulus by comparing several immiscible multilayer systems irradiated by He ions.

Radiation hardening originates from numerous sources, including voids, dislocations loops, amorphization and He bubbles (if He is involved) etc. It is important to identify the nature of defects to study hardening mechanism. However, other than voids and bubbles, loops and interstitials were usually undetectable and hard to quantify at low fluence. In this study, we adjust the fluence and energy so that the peak and average damage (in term of dpa) are similar in proton and He irradiated films (Fig. 2.1). As He bubbles prevail in He irradiated specimens and interstitial loops are major defects in proton irradiated specimens, this study offers an approach to qualitatively differentiate radiation hardening induced by interstitial loops and He bubbles.

As seen in Fig. 2.7a, there exists a ~ 0.3 GPa hardness increase in proton irradiated specimens. As there were no He introduced during proton radiation, it is reasonable to attribute this hardness increase to primarily dislocation loops. Assuming a similar dislocation loop density in He irradiated films, radiation hardening by a similar magnitude, ~ 0.3 GPa, shall be induced as shown by the dash line in Fig. 2.7b. Such a level of hardening fits well for He irradiated multilayers when h ≤ 2 nm. Therefore, the size dependent radiation hardening seen in Fig. 2.7b is probably the actual hardening induced by He bubbles. Friedel-Kroupa-Hirsch (FKH) model [32] is used first to describe the bubble induced increase in yield strength

$$\Delta\sigma = \frac{1}{8}MGbdN_{He}^{2/3}$$

(3),

where M is Taylor factor, which is ~ 2.7 for fcc metals, d and N are the respective diameter and density of He bubbles. By applying $d = 1.2$ nm, $G = 53$ GPa (average of Ag and Ni), $b = 0.269$ nm (average of Ag and Ni) and the average He bubble density of ~ 1.2 $\times 10^{24}$ m^{-3} (at half-maximum of the bubble density curve for Ag/Ni 50nm), $\Delta\sigma$ is calculated to be ~ 0.13 GPa, corresponding to ~ 0.39 GPa hardness increase, much lower than experimental observations, ~ 1.1 GPa. Such a large underestimation of radiation hardening arises because the equation did not take layer structure into account. Assume He bubbles are obstacles to dislocation in multilayers, Wei *et al.* modified the confined layer slip (CLS) model as follows [21]:

$$\Delta H = H_i \left(1 - \frac{l}{\sqrt{2}h} \right)$$

(4),

where ΔH is the hardness increase, H_i is the average obstacle hardness (derived from σ_i by multiplying a factor of 9), and l is the average bubble spacing which can be calculated from bubble density. Thus the irradiation-induced hardening can be divided into three regions. When $h > l$, ΔH is close to H_i. And for bulk materials whose $h \rightarrow \infty$, $\Delta H = H_i$. When h is comparable with l, $\Delta H > 0$, radiation induced hardening is evident due to bubble obstacles. When $h < l$, $\Delta H = 0$, which means original interfaces still dominate the hardening mechanism, resulting in no hardening. By subtracting 0.3 GPa from overall hardening, we obtain bubble induced hardening as shown in Fig. 2.8a. By applying $l =$ 9.4 nm (calculated from bubble density in Fig. 2.6) and varying H_i value, ΔH can be plotted as a function of $h^{-1/2}$, fitting the experimental data. The average obstacle strength H_i is in the range of 0.8 – 1.1 GPa, as compared to 0.42 GPa in Ag/V, 1.8 GPa in Fe/W and 0.52 GPa in Cu/V (with different l) [21]. Fig. 2.8b shows H_i as a function of average shear modulus by comparing several aforementioned multilayer systems irradiated by He ions. It is found that H_i exhibits a linear relationship with average shear modulus, showing a slope of ~ 0.017. Therefore, equation (4) can be modified to:

$$\Delta H = kG_{ave} \left(1 - \frac{l}{\sqrt{2}h} \right)$$

(5),

where k is the slope showed in Fig. 8b (~ 0.017) and G_{ave} is the average shear modulus of the constituents. Note that bubble spacing (derived from 50 nm experimental data) used for analysis is kept as a constant for all layer thickness, therefore H_i estimated in this study is an upper bound for large layer thickness and a lower bound for medium layer thickness. It is likely the barrier resistance of He bubbles to propagation of dislocations might depend on the yield strength of matrix materials.

In conclusion, He and proton radiation induced microstructural evolution and hardening in Ag/Ni multilayers were compared systematically. Bubbles were found to be the major defects in He irradiated films, whereas dislocation loops were observed in proton irradiated Ag/Ni. Proton radiation induced much less lattice distortion in comparison to He bubble induced damage. Proton radiation induced hardening is low and has little dependence on layer thickness, in drastic contrast to He bubble induced

hardening in multilayers. Bubble induced hardening follows the modified CLS model.

References

[1] G. Ackland, Science, 327 (2010) 1587-1588.

[2] R. Andrievskii, The Physics of Metals and Metallography, 110 (2010) 229-240.

[3] J.L. Boutard, S. Dudarev, E. Diegele, Materials Issues for Generation IV Systems, in, Springer Netherlands, 2008, pp. 481-500.

[4] R.W. Grimes, R.J.M. Konings, L. Edwards, Nat Mater, 7 (2008) 683-685.

[5] E.G. Fu, J. Carter, G. Swadener, A. Misra, L. Shao, H. Wang, X. Zhang, Journal of Nuclear Materials, 385 (2009) 629-632.

[6] N. Li, E.G. Fu, H. Wang, J.J. Carter, L. Shao, S.A. Maloy, A. Misra, X. Zhang, Journal of Nuclear Materials, 389 (2009) 233-238.

[7] E.G. Fu, A. Misra, H. Wang, L. Shao, X. Zhang, Journal of Nuclear Materials, 407 (2010) 178-188.

[8] A. Misra, M. Demkowicz, X. Zhang, R. Hoagland, JOM Journal of the Minerals, Metals and Materials Society, 59 (2007) 62-65.

[9] B.N. Singh, M. Eldrup, S.J. Zinkle, S.I. Golubov, Philosophical Magazine A, 82 (2002) 1137-1158.

[10] S.J. Zinkle, Materials Issues for Generation IV Systems, in, Springer Netherlands, 2008, pp. 227-244.

[11] B.N. Singh, Philosophical Magazine, 29 (1974) 25-42.

[12] X.-M. Bai, A.F. Voter, R.G. Hoagland, M. Nastasi, B.P. Uberuaga, Science, 327 (2010) 1631-1634.

[13] C. Sun, K.Y. Yu, J.H. Lee, Y. Liu, H. Wang, L. Shao, S.A. Maloy, K.T. Hartwig, X. Zhang, Journal of Nuclear Materials, 420 (2012) 235-240.

[14] K.Y. Yu, Y. Liu, C. Sun, H. Wang, L. Shao, E.G. Fu, X. Zhang, Journal of Nuclear Materials, 425 (2012) 140-146.

[15] H. Wang, R. Araujo, J.G. Swadener, Y.Q. Wang, X. Zhang, E.G. Fu, T. Cagin, Nuclear Instruments and Methods in Physics Research Section B: Beam Interactions with Materials and Atoms, 261 (2007) 1162-1166.

[16] G.R. Odette, M.J. Alinger, B.D. Wirth, Annual Review of Materials Research, 38

(2008) 471-503.

[17] M.J. Demkowicz, O. Anderoglu, X. Zhang, A. Misra, Journal of Materials Research, 26 (2011) 1666-1675.

[18] M.J. Demkowicz, P. Bellon, B.D. Wirth, MRS Bulletin, 35 (2010) 992-998.

[19] J. Pacaud, C. Jaouen, G. Gladyszewski, Journal of Applied Physics, 86 (1999) 4847-4854.

[20] W. Yuan, Acta Phys. Sin., 61 (2012).

[21] Q.M. Wei, N. Li, N. Mara, M. Nastasi, A. Misra, Acta Materialia, 59 (2011) 6331-6340.

[22] M. Milosavljević, V. Milinović, D. Peruško, A. Grce, M. Stojanović, D. Pjević, M. Mitrić, J. Kovač, K.P. Homewood, Nuclear Instruments and Methods in Physics Research Section B: Beam Interactions with Materials and Atoms, 269 (2011) 2090-2097.

[23] N. Li, M.S. Martin, O. Anderoglu, A. Misra, L. Shao, H. Wang, X. Zhang, Journal of Applied Physics, 105 (2009) 123522-123528.

[24] N. Li, J.J. Carter, A. Misra, L. Shao, H. Wang, X. Zhang, Philosophical Magazine Letters, 91 (2010) 18-28.

[25] J.F. Ziegler, U. Littmark, J.P. Biersack, Calculation using the Stopping and Range of Ions in Matter (SRIM) Code. <http://www.srim.org/>.

[26] N. Li, K.Y. Yu, J. Lee, H. Wang, X. Zhang, Journal of Applied Physics, 107 (2010) 093503-093507.

[27] A. Polian, M. Grimsditch, EPL (Europhysics Letters), 2 (1986) 849.

[28] L. Vitos, A.V. Ruban, H.L. Skriver, J. Kollár, Surface Science, 411 (1998) 186-202.

[29] S.E. Donnelly, Radiation Effects, 90 (1985) 1-47.

[30] J.L. J. P. Hirth, Theory of dislocations, 1967.

[31] G. Was, Fundamentals of Radiation Materials Science, 2007.

[32] F. Kroupa, P.B. Hirsch, Discuss. Faraday Soc. , 38 (1964) 49.

II. 3. Microstructure and strengthening mechanisms in Cu/Fe multilayers (Acta Materialia, 2012)

Note: We have reported preliminary studies on this subject in the previous annual report. There were a couple of open questions back then. Here we present a thorough report of this project.

Certain metallic multilayers with nanoscale layer thicknesses exhibit high strength close to theoretical values [1-6]. Deformation mechanisms have been extensively studied in metallic multilayers. Dislocation pile-ups [7], moduli mismatch [8], misfit dislocations and coherency stress [9] are among some of the important factors that contribute to hardening. Some of the models that explain the high strength of multilayers are briefly described as follows.

Hall-Petch model [3, 7] operates when individual layer thickness, h, is greater than tens of nanometers. Strengthening arises from dislocations pile-up on the glide plane against grain or interphase boundaries. The hardness increases linearly with $h^{-1/2}$, following the Hall-Petch model. Thus the Hall-Petch slope indicates the resistance of the boundary and is often used to predict the peak strength of multilayers [3, 10, 11]. However, the strength predicted from slope is sometimes not consist with the measured peak strength, since the multilayers may contain defects, e.g. columnar grains and twins [12-14] that have much smaller dimension than individual layer thickness. Certain modifications were made accordingly. Misra *et al* [15] developed a deformation mechanism map to determine the dominant feature size for dislocation pile-ups against boundaries. Pande *et al* [16] developed a model to incorporate the influence of twins on Hall-Petch slope.

At smaller h, tens of nm, confined layer slip (CLS) model based on Orowan bowing mechanism [1, 17] is more appropriate. At this length scale, dislocation pile-up becomes more difficult. Correspondingly dislocations are confined by and glide between layer interfaces, instead of transmitting across the interfaces because the stress required for bowing of dislocations is less than that for transpassing across interface. Recently Misra *et al* [11] developed a refined CLS model by considering interface stress and dislocation-dislocation interactions.

Interface barrier strength (IBS) mechanism operates when h is several nm. The strength of multilayer at such length scales is determined by the inherent resistance of layer interface to the transmission of single dislocations. Various factors, including

Koehler stress [8], coherency stress and misfit dislocations [9], etc. are considered to estimate the interface barrier strength. Koehler stress arises from a significant repulsive image force for a dislocation to slip from the lower modulus phase to higher modulus counterpart. Meanwhile coherency stresses alternating from tension to compression periodically often exist and lead to resistance to dislocation propagation across interfaces. When the layer thickness is above critical thickness for coherency, misfit dislocation arrays often appear to accommodate strain between layers. The interaction of misfit and gliding dislocations would also increase the interface strength.

FCC/BCC multilayers e.g. Cu/Nb [18], Cu/Cr [19, 20], Cu/V [21], V/Ag [22], with opaque and immiscible layer interfaces attract significant attention. The discontinuity of slip systems across interface and the lower shear resistance of layer interface (referred to as weak interface), in e.g. Cu/Nb, promote the dissociation or spread of the core of gliding dislocations at the interface [23, 24]. A dislocation once absorbed by a weak layer interface, loses its singularity, making it difficult to be reemitted in the opposite layers. Therefore, the "weak interface" offers a strong barrier to the transmission of dislocations. Meanwhile Cu/Fe multilayers were studied in several occasions. Thick Cu/Fe multilayers with h of several microns were fabricated by rolling of alternatively bonded Cu and Fe sheets [25]. Gao *et al* [26] fabricated Cu/Fe multilayers with h over a range of 5 – 40 nm. Their study showed a very high peak hardness, ~ 7.3 GPa, with however little explanation. Shamsutdinov *et al* [27] studied Cu/Fe multilayer with fixed Cu sub-layer thickness of 5 nm and varied Fe sub-layer thickness from 13 to 54 nm and found out that grain size and existence of voids in the multilayer determined the stress state in the film. Cu/Fe multilayer was also a popular subject due to its giant magnetoresistance (GMR) effect [28, 29].

In spite of these studies, the microstructure of Cu/Fe multilayers were less well understood, and a systematic study of their deformation mechanism is lacking. In this paper, we provide extensive microscopy studies of layer interface and microstructure of Cu/Fe multilayers with two types of textures, and identify the influence of layer interface as well as other defects, such as nanoscale columnar grain boundaries and high density twins, on deformation mechanisms of the system.

Cu/Fe multilayers with equal individual layer thickness (h), varying from 0.75 to

200 nm were magnetron sputtered at room temperature on HF etched Si (110) and Si (100) substrates. The chamber was evacuated to a base pressure less than 8×10^{-8} torr prior to deposition. Before the deposition of Cu/Fe multilayers, a 100 nm thick Cu seed layer was deposited. The total film thickness was ~ 500 nm when h = 0.75 nm, ~ 1 μm when h = 1 – 5 nm, ~ 1.5 μm when h = 10, 25 nm, ~ 2 μm when h = 50, 100 nm, and ~ 4 μm when h = 200 nm. The deposition rate of Fe is 0.5 nm/s for all layer thickness. For Cu, the deposition rate was ~ 0.33 - 1.1 nm/s. X-ray diffraction (XRD) experiments were performed in a Brukers D8 Discover X-ray powder diffractometer at room temperature. Transmission electron microscopy (TEM) experiment was carried out on a JEOL 2010 transmission electron microscope operated at 200 kV. Scanning transmission electron microscopy (STEM) experiments and energy dispersive X-ray (EDX) analyses were performed on an FEI Tecnai G2 F20 microscope operated at 200 kV with a Fischione ultra-high resolution high-angle annular dark field (HAADF) detector (0.23 nm resolution in STEM image mode) and an Oxford Instruments EDX detector with a spatial resolution of ~ 1 nm for chemical analysis. Film hardness and elastic modulus were measured based on an average of 12 - 15 indents at different indentation depths by a Fisherscope HM 2000XYp micro/nanoindentor with a Vickers indenter tip. Several bilayers were typically probed during nanoindentation, while special care was taken to avoid substrate effect. For Cu/Fe film with film thickness ~ 500 nm, the Hysitron Triboindenter was employed to confirm the hardness value. Cross-sectional TEM (XTEM) samples were prepared by dimpling and low energy (3.5 keV) Ar ion milling and subsequent ion polishing.

Examination of microstructure and mechanical properties

XRD patterns of as-deposited Cu/Fe multilayers on Si (110) substrate are shown in Fig. 3.1. When h ≥ 25 nm, Cu (111) and Fe (110) peaks were observed. At smaller h, the relative intensity of Fe (110) peak diminished rapidly, whereas the Cu (111) peak intensity became much stronger. When h ≤ 10 nm, Fe (110) peak disappeared and Cu (111) became the primary peak. Fig. 3.2 compares the selected area diffraction (SAD) patterns of various multilayers on Si (110) substrate. Cu 200 nm/Fe 200 nm (referred to as Cu/Fe 200 nm hereafter) multilayer showed polycrystalline structures while others exhibited increasing intensity of Cu (111) and Fe (110) textures at smaller h. Careful

examination showed that Cu (111) and Fe (110) did not overlap until h = 5 nm, below
which there is increasing magnitude of coherency. When h = 0.75 nm, single crystal like
diffraction pattern was identified. Furthermore the diffraction pattern suggests the
formation of both Σ3 (111) type of coherent twin boundary (CTB) and Σ3 (112)
incoherent twin boundary (ITB).

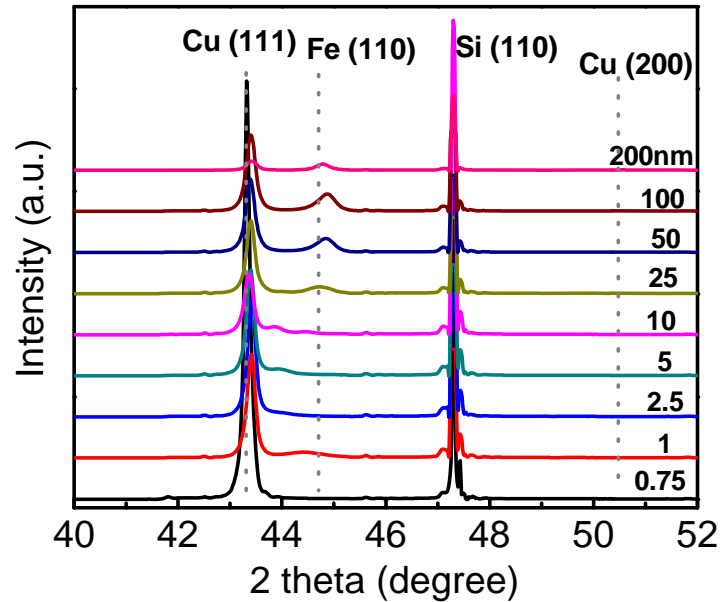Figure 3.1 XRD patterns of Cu/Fe multilayers deposited on Si (110) substrates. Only Cu
(111) and Fe (110) were observed. At smaller layer thickness, the peak intensity of Fe
(110) decreased, whereas that of the Cu (111) increased slightly. The Cu/Fe 0.75nm
multilayer exhibits an extremely strong Cu (111) texture. Note that the peak intensity of
Cu (111) peaks is partially contributed from 100 nm thick Cu seed layer.
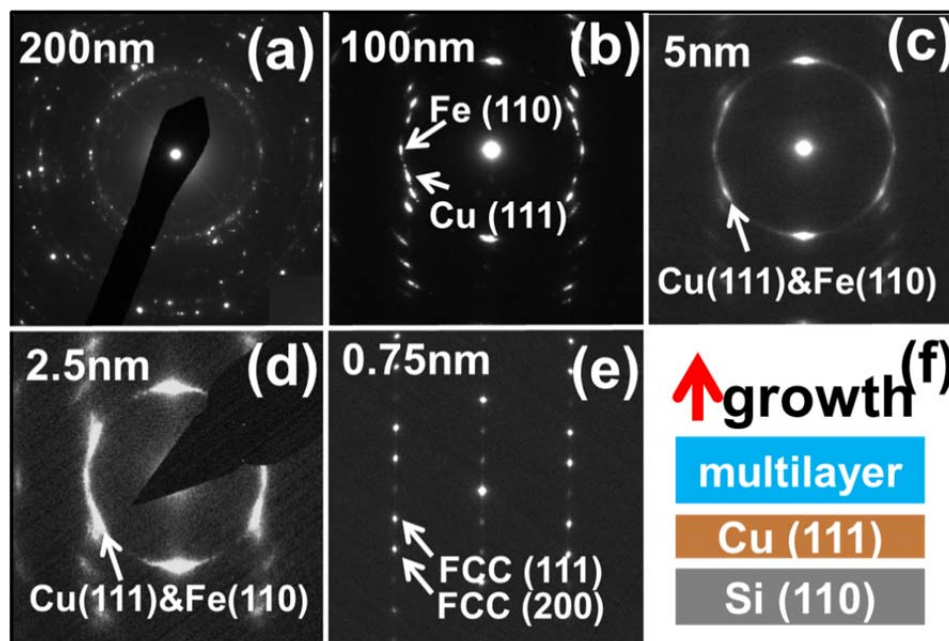
Figure 3.2 SAD patterns of Cu/Fe multilayers on Si (110) substrates with a 100 nm Cu (111) seed layer: (a) Cu/Fe 200 nm showed polycrystalline structure; (b)-(d) Cu/Fe 100, 5 and 2.5 nm multilayers showed Cu (111) and Fe (110) texture; (e) Cu/Fe 0.75 nm film showed twinned diffraction pattern with single crystal like diffraction spots; (f) schematic exhibition of growth direction and film orientation. When h> 5 nm Cu (111) and Fe (110) diffraction dots were separated.
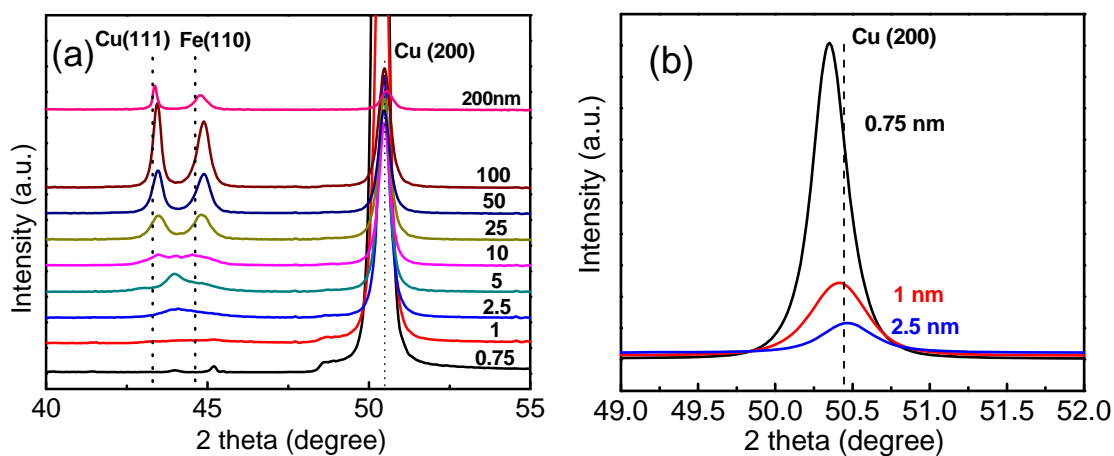
Figure 3.3 (a) XRD patterns of Cu/Fe multilayers on Si (100) substrates with a 100 nm

thick Cu (100) seed layer. Films had polycrystalline nature when h > 5 nm as evidenced by the appearance of Cu (111) and Fe (110) peaks. When h ≤ 2.5 nm, the intensity of the Cu (200) peak increased dramatically. (b) The position of Cu (200) peaks shifted to lower angle at smaller h.

XRD patterns of Cu/Fe multilayers on Si (100) substrate (Fig. 3.3a) showed that films had polycrystalline nature when h ≥ 5 nm, very similar to that observed in multilayers on Si (110) substrate. The intensity of Cu (111) and Fe (110) peaks completely diminished only when h ≤ 1 nm, indicating the formation of fully coherent (100) type of interface. Meanwhile, the Cu (200) peak intensity increased dramatically as h decreased to below 2.5 nm as shown in Fig. 3.3b.
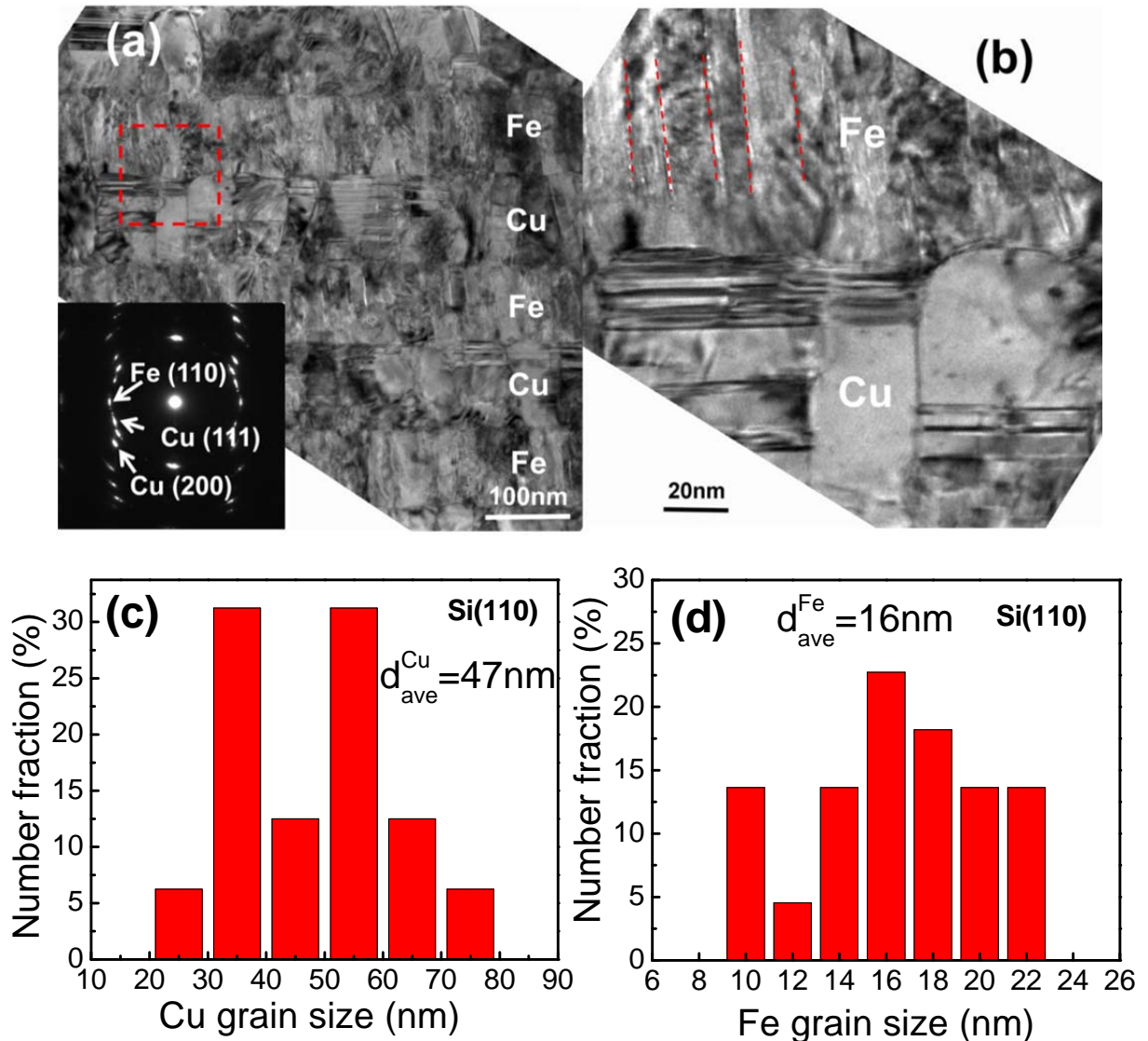
Figure 3.4 (a) A cross-sectional TEM (XTEM) micrograph of Cu/Fe 100nm on Si (110) substrate shows abundant twins in Cu layers. (b) A magnified view of the box in (a) reveals the formation of nanoscale columnar grains in Fe layers; (c) and (d) display statistical distribution of grain in Cu and Fe, and the average columnar grain sizes of Cu and Fe are ~ 47 and 16 nm, respectively.

In what follows, we present extensive microscopy studies of the microstructure of multilayers. In Cu/Fe 100 nm multilayer on Si (110) substrate (Fig. 3.4a-b), twins were occasionally observed in Cu, wherein Fe was composed of nanoscale columnar grains. Statistical analyses in Fig. 3.4c and d shows that the average columnar grain size of Cu is ~ 47 nm, three times of that in Fe, ~ 16 nm.
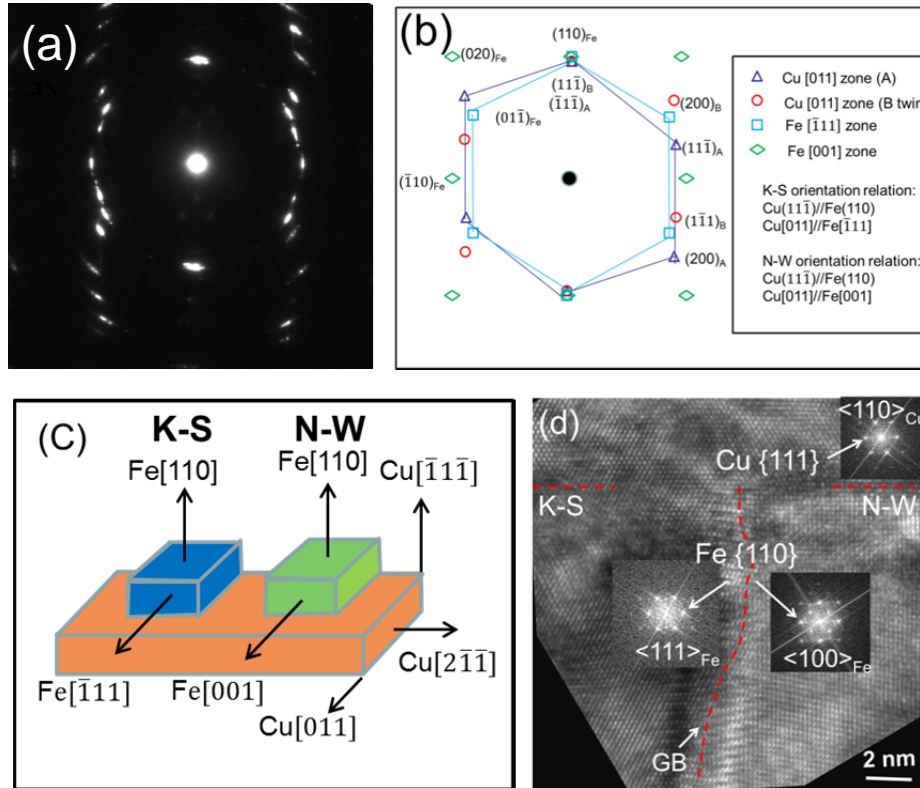
Figure 3.5 (a) SAD pattern and (b) its corresponding indexes in Cu/Fe 100 nm films on Si (110) substrate illustrate two types of orientation relationship between Cu and Fe, namely

K-S and N-W orientation. (c) Schematics illustrate the orientation relationships: K-S $((\bar{1}1\bar{1})_{Cu}// (110)_{Fe}, [011]_{Cu}//[\bar{1}11]_{Fe})$ and N-W $((\bar{1}1\bar{1})_{Cu}//(110)_{Fe}, [011]_{Cu}//[001]_{Fe})$. (d) HRTEM micrograph showed the formation of K-S and N-W relationship between Cu and Fe in neighboring grains. Fe was observed along <111> and <100> zone axes, whereas Cu was examined along <110> zone as shown by the fast Fourier transforms (FFTs).

Close examination of diffraction pattern of the same specimen (Fig. 3.5a-b) reveals two types of orientation relationship along interface, one being Kurdjumov-Sachs (K-S): $(\bar{1}1\bar{1})_{Cu}//(110)_{Fe}$, $[011]_{Cu}//[\bar{1}11]_{Fe}$, and the other one being Nishiyama-Wasserman (N-W) relation: $(\bar{1}1\bar{1})_{Cu}//(110)_{Fe}$, $[011]_{Cu}//[001]_{Fe}$, as shown schematically in Fig. 3.5c. In Fig. 3.5d, an HRTEM image exhibits the coexistence of the K-S and N-W interfaces. A single grain in Cu (the top layer) formed two types of interface with neighboring Fe grains underneath it. The inserted FFTs confirmed the existence of two different orientations in neighboring Fe grains. In para llel Cu/Fe 100 nm multilayer on Si (100) substrate has much weaker texture (Fig. 3.6a) and less twins in Cu layer (Fig. 3.6b). The average columnar grain size in Fe remained small, ~ 15 nm, comparing to ~ 56 nm in Cu as shown in Fig. 3.6c and d.
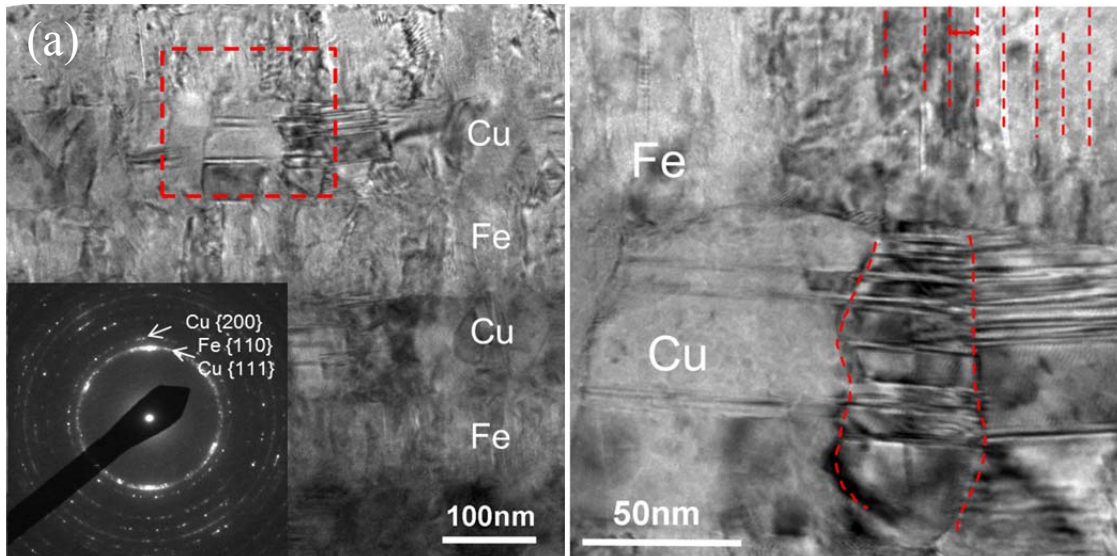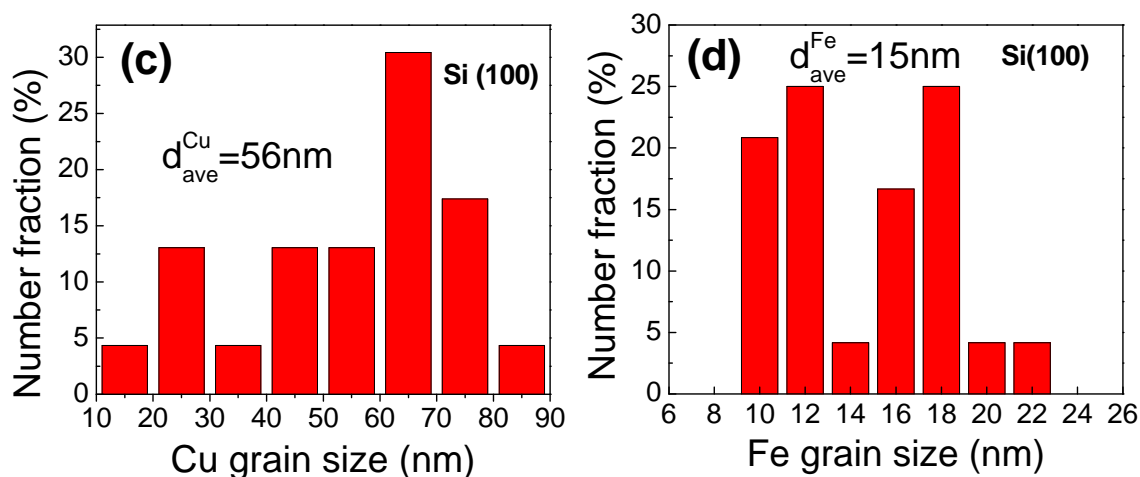
Figure 3.6 (a) An XTEM micrograph of Cu/Fe 100 nm multilayer on Si (100) substrate shows polycrystalline films as confirmed by the SAD pattern, and some twins were observed in Cu layers. (b) A magnified TEM micrograph shows that Fe layer was again composed of nano-columns. (c) and (d) are statistical distributions that show an average grain size of ~ 56 and 15 nm in Cu and Fe respectively.
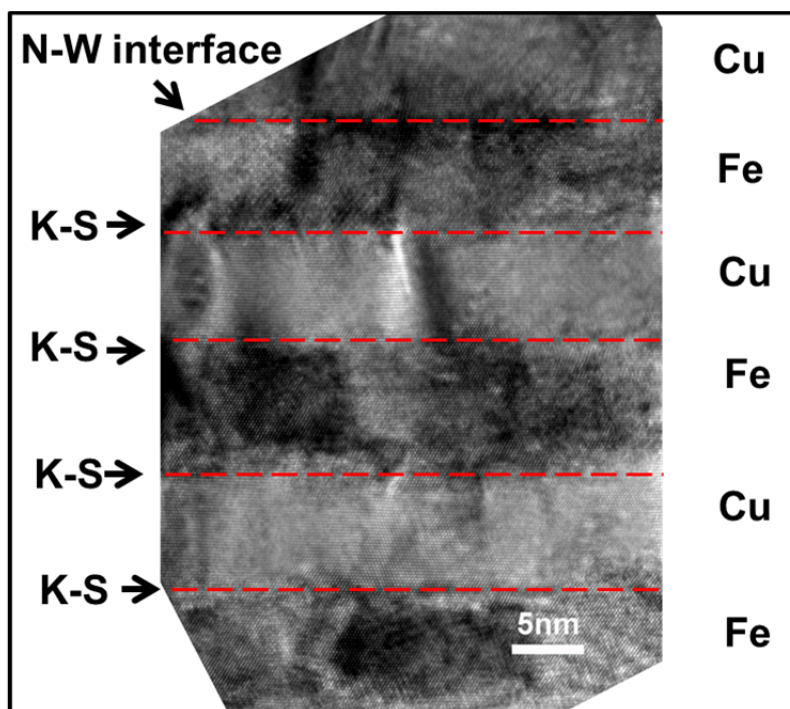
Figure 3.7 XTEM micrograph of Cu/Fe 10 nm multilayers grown on Si (110) substrate. The grain sizes of Cu and Fe were larger than layer thickness. Both K-S and N-W orientation relationships were observed.

Table 1. A summary of grain and twin sizes at different layer thicknesses.

Sample	Cu grain size (nm)	Fe grain size (nm)
Cu/Fe 200 nm // Si(110)	115	23
Cu/Fe 100 nm // Si(110)	47	16
Cu/Fe 50 nm // Si(110)	30	11
Cu/Fe 100 nm // Si(100)	56	15
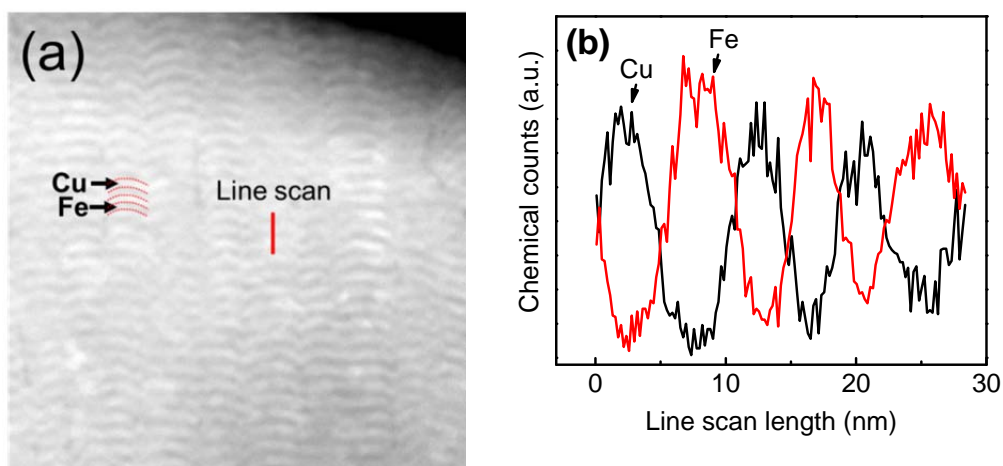
Figure 3.8 (a) A cross-sectional STEM micrograph of Cu/Fe 5nm film on Si (110) substrate shows discrete layer structure. (b) Compositional line profile displays a chemically modulated layer structure with insignificant intermixing.

As summarized in Table 1, the average columnar grain sizes in Cu and Fe decreased with decreasing h, from 200 to 50 nm, and the grain size of Cu is 3-5 times that of Fe. To see whether the grain size of Fe decreases further at smaller h, we examined Cu/Fe 10 nm multilayer on Si (110). As shown in Fig. 3.7, the columnar grain size of Fe is comparable or slightly greater than h. The same micrograph also delineates the formation of K-S and N-W type of orientations along interfaces.

We performed STEM experiments to evaluate the morphology and chemistry of multilayers. Fig. 3.8a shows a STEM image and compositional line profile of a Cu/Fe 5 nm multilayer. Layer structures are evident in spite of a small difference in atomic number between Cu (Z = 29) and Fe (Z = 26). No significant inter-diffusion occurred as suggested from the compositional profile in Fig. 3.8b.
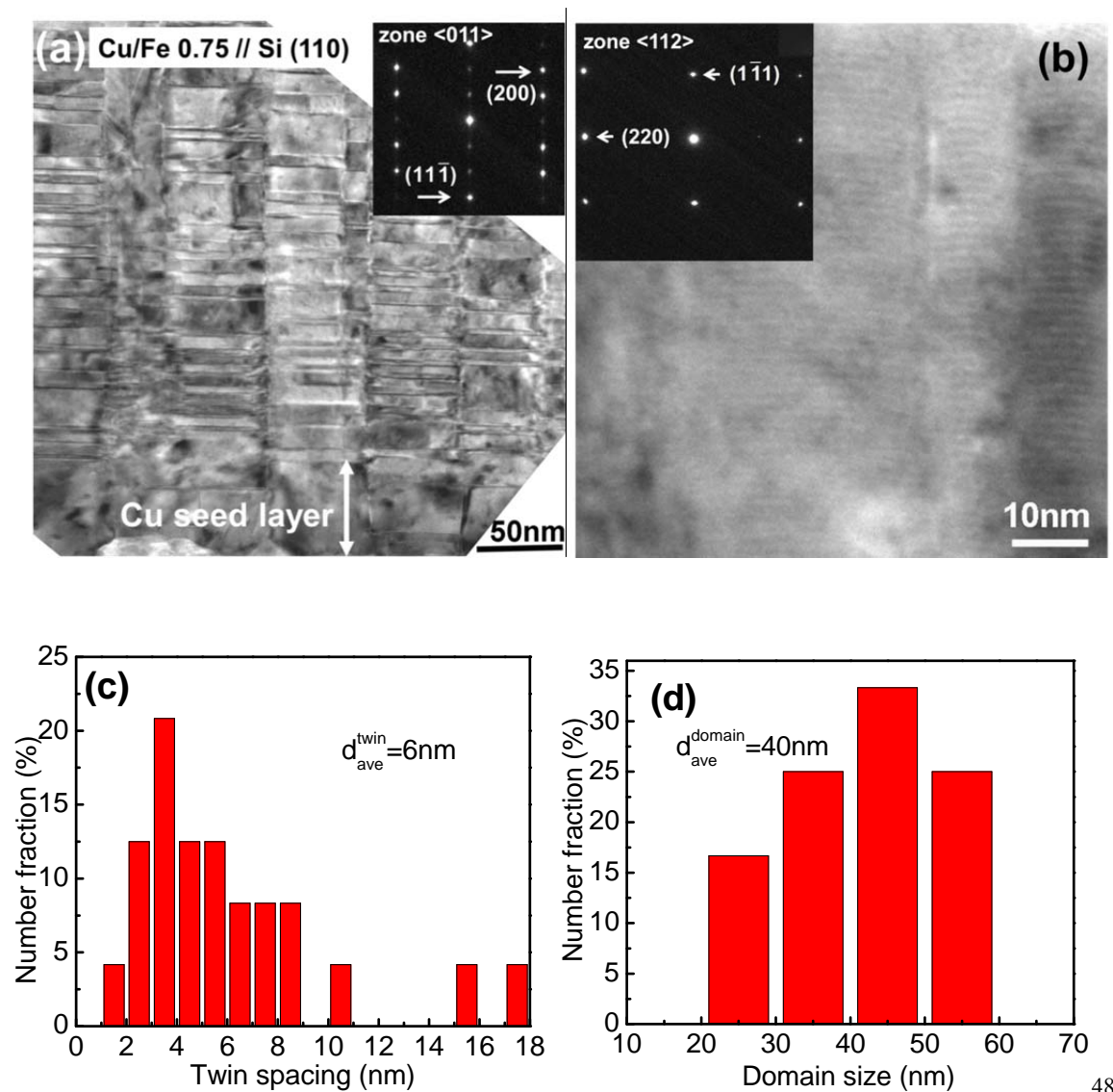
Figure 3.9 (a) An XTEM micrograph of Cu/Fe 0.75 nm multilayer on Si (110) substrate examined along the FCC <110> zone axis exhibits high density of growth twins. The SAD inset also shows the evidence of incoherent twin boundaries. (b) When the same film was studied along the FCC <112> zone axis, discrete layer structure was observed. (c) and (d): statistical distributions show that the average twin spacing and domain sizes are ~ 6 and 40 nm, respectively.
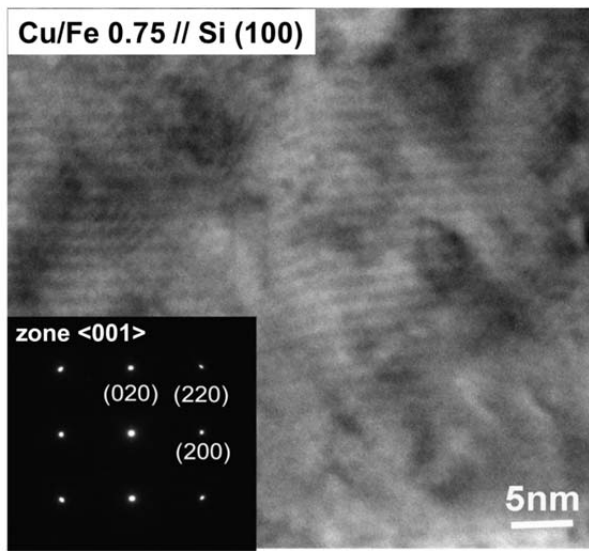

Figure 3.10 An XTEM micrograph of Cu/Fe 0.75 nm film on Si (100) substrate examined along the FCC <100> zone axis exhibits clear layer structure. The inserted SAD pattern shows single crystal like diffraction pattern.

Cu/Fe 0.75 nm multilayer deposited on Si (110) had high density twins as shown in Fig. 3.9a when examined along FCC <110> zone axis (// Si <111>). Along FCC <112> zone axis (// Si <112>), only discrete layer structure could be observed (Fig. 3.9b), wherein twins were not visible. As shown in Fig. 3.9c and d, the average twin thickness and columnar grain size are ~ 6 and 40 nm, respectively. In comparison in Cu/Fe 0.75 nm multilayers grown on Si (100) substrate, only layer structure was observed and there is no evidence of twins when examined along FCC <001> zone axis (Fig. 3.10). The SAD pattern indicates the formation of single crystal like structure.
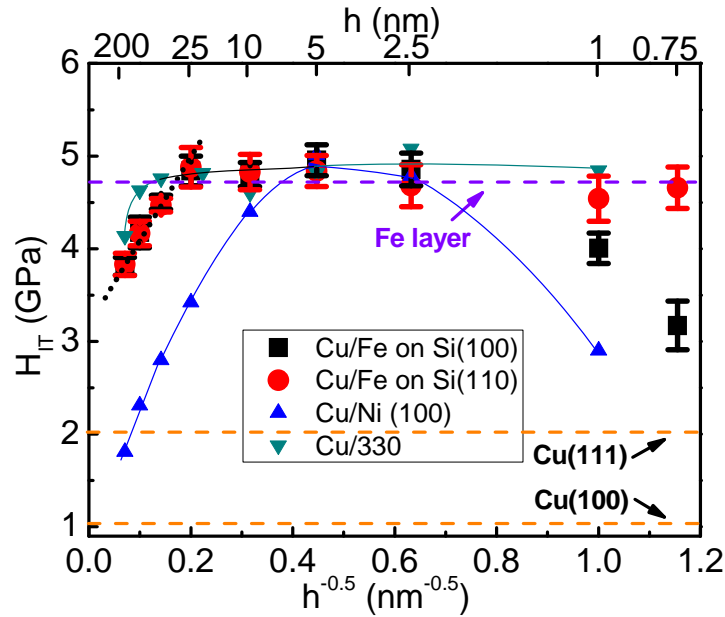
Figure 3.11 The hardnesses of sputtered Cu/Fe multilayers deposited on Si (100) and Si (110) substrates are plotted as a function of $h^{-0.5}$, and compared to that of Cu/Ni (100) and Cu/330 SS multilayers.

The hardnesses of Cu/Fe multilayers on Si (110) and (100) substrates are shown as a function of $h^{-1/2}$ in Fig. 3.11, and are compared to highly textured Cu/Ni (100) multilayers [5] and (111) textured Cu/330 stainless steel (SS) multilayers [10]. Several distinct characteristics are noteworthy.

(1) The hardnesses of Cu/Fe multilayers on different substrates overlapped when h > 2.5 nm. At smaller h (< 2.5 nm), softening was observed for the film on Si (100) substrate, which is similar to Cu/Ni on Si (100). However, the hardness of Cu/Fe films on Si (110) retained their high strength at smaller h.

(2) The hardness of two sets of Cu/Fe multilayers reaches a plateau when h = 25 nm, similar to what was observed in Cu/330 SS [10]. Meanwhile, the maximum strength of the four sets of multilayers is nearly identical.

(3) At large layer thickness ($\geq$ 50 nm), the Hall-Petch slope is $\sim$ 10.3 GPa·nm$^{1/2}$ for Cu/Fe systems, much lower than the slope of Cu/Ni ($\sim$ 15 GPa·nm$^{1/2}$) and Cu/330 SS

multilayers ($\sim$ 19.5 GPa·nm$^{1/2}$).

Microstructural evolution

Columnar grain size clearly evolves with h. When h $\geq$ 50 nm, the columnar grain size of Cu decreased from 115 to 30 nm at smaller h. Meanwhile the grain size of Fe also decreased from 23 to 11 nm. When h decreased to below 50 nm, the grain size of Fe did not decrease further.

The grain size of Cu is approximately 3 times of that in Fe in Cu/Fe 100 nm multilayer on Si (110) substrate. As the neighboring Fe grains frequently formed both K-S and N-W orientation relationships adjacent to the same Cu grain, thus there must be high angle grain boundaries between Fe grains. The co-existence of K-S and N-W type orientation relationships were also seen in V/Ag system at interfaces with various curvatures [22].

Cu/Fe 0.75 nm multilayers on both substrates exhibited single crystal like structure. Fe had face centered cubic (FCC) structure, and hence formed coherent (transparent) interface with Cu. The critical layer thickness for the formation of misfit dislocations can be estimated by [30],

$$h_c = \frac{b}{8\pi(1+\nu)\varepsilon_m}[\ln\left(\frac{h_c}{b}\right)+1]$$

$$(1)$$

wherein the magnitude of the Burgers vector b is 0.25 nm, the mismatch strain ε_m is 0.83% (the lattice constant of Cu and FCC Fe are 3.615 and 3.585 Å [31, 32], respectively), the Poisson's ratio ν is 0.3. The calculated value for h_c is $\sim$ 3 nm. Thus Cu/Fe 0.75 nm multilayer should be fully coherent. However coherency quickly degraded when h increased to 1 nm in both Cu/Fe (100) and (111) films. This could be related to the fact that FCC Fe is a metastable phase. Hence there is a driving for FCC Fe to transform to stable BCC phase. The energy difference between FCC and BCC Fe was not considered when calculating h_c, and thus leads to its overestimation.

The formation of nanotwins in (111) Cu/Fe multilayers

It is unusual to spot the formation of twins in Cu/Fe multilayers. It is known that twins can relieve stress. Hence it is necessary to compare the mismatch strain energy and the energy required for the formation of twins.

To nucleate a twin interface, one leading partial dislocation is emitted from grain boundary, followed by a twinning partial dislocation of the same Burgers vector on the adjacent slip plane [33, 34]. Based on the formation of twinned nuclei, subsequent atoms would stack continuously to extend the twin thickness during deposition process. Thus, we assume two partial dislocations are required to nucleate a twin interface. The energy for formation of a twin, E_{twin}, is thus estimated by

$$E_{twin} = E_{dis} + \gamma_{twin}$$

(2)

where γ_{twin} is the energy of twin boundaries (~ 24 mJ/m^2 [9]) for Cu, and E_{dis} is the energy of a pair of partial dislocations and can be calculated by

$$E_{disl} = \frac{Gb^2}{2\pi} \ln(\frac{D}{b} + 1)$$

(3)

where D is the grain size. The energy of a pair of partial dislocation with 40 nm in length (equal to the average grain size) is thus $\sim 3.24 \times 10^{-17}$ J. Meanwhile the energy of twin boundary in a 40 nm grain is $\sim 3.84 \times 10^{-17}$ J. The mismatch strain energy, E_m can be calculated by [35]

$$E_m = \varepsilon_m{}^2 M_{Fe} h_{Fe}$$

(4)

where M is biaxial modulus of Fe and ε_m is mismatch strain. As the average twin thickness is ~ 6 nm, indicating that when the thickness of Fe approaches 3 nm, a twin partial forms as shown schematically in Fig. 3.12. Hence using $h_{Fe} = 3$ nm, we arrive that the overall mismatch strain energy in a 40 nm grain is $\sim 9.9 \times 10^{-17}$ J, sufficient to trigger the formation of twins and a pair of partial dislocations.
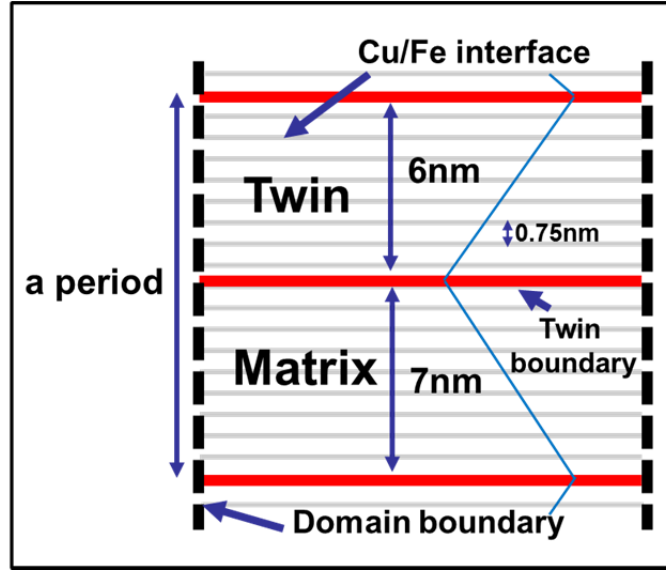
Figure 3.12 Schematic illustration of a period of (111) Cu/Fe 0.75 nm multilayer with twin structure, including a twin and a matrix.

Next we estimate the shear stress close to the free edge of islands to nucleate a Shockley partial in Cu. At the free surface, there is no stress; while inside the island, the biaxial stress (mismatch stress) increases rapidly to a steady state value. An interfacial shear stress is thus required to transfer the stress (from substrate or seed layer) into films. The shear stress, τ, can be estimated as [35, 36]

$$\tau \approx \sigma_m \sqrt{\frac{kh_f}{2\pi x}}$$

(5)

where σ_m is the biaxial mismatch stress, x is the distance from the edge of island, k is the biaxial modulus ratio between substrate and films, and can be calculated as

$$k = \left(\frac{E_s}{1-v_s}\right) / \left(\frac{E_f}{1-v_f}\right)$$

(6)

τ is estimated to be $\sim 0.7 - 1.0$ GPa when x is $\frac{1}{2}$ - 1 h_f. It has been shown that the required shear stress to create a Shockley partial in Cu is ~ 540MPa [36], thus the shear

stress is sufficient to nucleate a Shockley partial in Cu.

Mechanical properties-grain, layer and twin interface induced strengthening

(a) Strengthening at large layer thickness (h = 50 - 200 nm)

The following analyses show that an appropriate parameter to determine the size dependent strengthening mechanisms is the average columnar grain size of Fe, rather than h.

Hall-Petch model: dislocation pile-up against layer interface

Previous studies show that if layer thickness is deterministic dimension for Hall-Petch type of strengthening in multilayers, then the maximum hardness can be estimated reasonably well by using the Hall-Petch slope (K_{HP}) via [3]:

$$K_{HP} = \sqrt{\tau^* \mu b / [\pi(1-\nu)]}$$

(7)

where τ^* is the interface barrier strength, μ is the shear modulus (μ=48 GPa for Cu), b is the Burgers vector (b=0.25 nm for Cu), and ν is the Poisson's ratio (~ 0.33). Using the measured slope 10.3 GPa·nm$^{1/2}$ for Cu/Fe we obtain τ^*= 0.24 GPa. The peak hardness could be estimated as 8.1τ^* by using the Tabor relation (H = 2.7 σ, where σ is the flow stress) and considering Taylor factor ($\sigma = 3\tau^*$). Thus, the estimated peak hardness is merely 1.9 GPa, much lower than the measured peak hardness, ~ 5 GPa.

Table 2. Comparisons of Hall-Petch slopes, estimated interface barrier strength, τ* from measured Hall-Petch slopes, peak hardness calculated from estimated interface barrier strength, measured peak hardness and, and the estimated Hall-Petch slope by elastic moduli and Burgers vectors.

Material	Cu/Fe	Cu/304	Cu/330	Cu/Ni(111)	Cu/Ni(100)
Experimental k (GPa·nm$^{1/2}$)	10.3	16.9	19.5	17.7	15
Calculated τ* (GPa)[a]	0.24	0.64	0.85	0.84	0.6
Calculated peak hardness (GPa)	1.9	5.2	7	6.8	4.8
Measured peak hardness	5	5.5	5.1	5.8	5

(GPa)

---

[a] $K_{HP} = \sqrt{\tau * \mu b / [\pi(1-v)]}$

In Table 2, we listed the relationship of Hall-Petch slope and peak hardness of Cu/304 SS [37], Cu/330 SS[10], and Cu/Ni (111) and (100) [5]. We found that except for Cu/Fe, the difference of measured and calculated peak hardnesses in most other systems is small. Thus Hall-Petch slope cannot be used to predict the peak strength of Cu/Fe multilayers.

Confined layer slip (CLS) model to describe dislocation activity in columnar Fe grains

The break-down of Hall-Petch model at such a large layer thickness and exceptionally high hardness of Cu/Fe (than Cu/Ni with identical h) indicates that strengthening mechanism is no longer determined by h alone. Microscopy studies have shown that when h = 50 - 200 nm, Fe was composed of nanoscale columnar grains with various grain size, ~ 11-23 nm. The grain size of Fe is clearly much less than layer thickness. Fig. 3.13 shows schematically the deformation mechanism in Cu/Fe with nanocolumns in Fe. Dislocations may pile-up in Cu. But for dislocation to transmit across interface into Fe layer, the dislocation must be able to propagate within narrow columns in Fe. Hence plastic yielding is determined by the stress necessary for single dislocation bowing via the CLS mechanism. The critical resolved shear stress τ_{cls} can thus be calculated by [11]

$$\tau_{cls} = \frac{\mu b}{8\pi d}\left(\frac{4-v}{1-v}\right)\ln(\frac{\alpha d}{b})$$ (8)

where μ is shear modulus (77.5 GPa for Fe), d is the columnar grain size of Fe, b is Burgers vector (0.248 nm for Fe) and α represents the core cut-off parameter. The calculated results (two dash lines) by using α = 0.11 and α = 0.15 are compared to experimental data in Fig. 3.14. The estimated hardness fits the experimental data well. Twin density was low in Cu at such a large layer thickness, and hence the contribution of twins may be insignificant over this range of layer thickness.
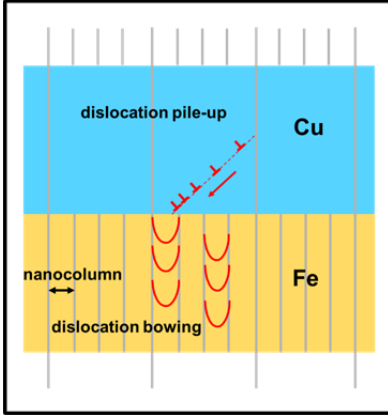
Figure 3.13 Schematic illustration of deformation mechanism in Cu/Fe multilayer with large layer thickness. In the Cu layer, dislocations pile up against phase interface; in Fe layer, dislocations bow out by confined layer slip mechanism.
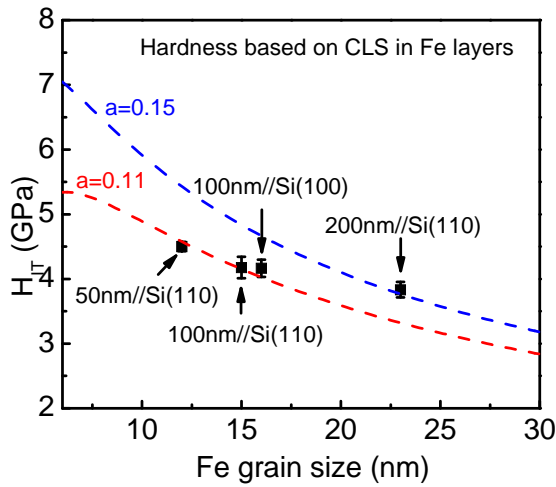

Figure 3.14 Experimental hardness data of multilayer with respect to Fe grain size at h=50-200 nm. Two dash curves are simulated hardness value based on CLS model of Fe grains.

(b) Strengthening mechanism when h = 2.5 – 25 nm.

Previous discussion demonstrates that the strengthening mainly arises from confined dislocation propagation in nanocolumns in Fe. However, with continuous decrease of layer thickness, the grain size is eventually greater than h. Hence strengthening is now determined by Cu/Fe interfaces. We now attempt to estimate the interface barrier strength, $\tau_{barrier}^*$, as [38]

$$\tau_{barrier}^* = \tau_d^* + \tau_k^* \qquad (9).$$

The first term τ_d^* comes from misfit dislocations and can be expressed by [9]

$$\tau_d^* = \alpha G^*[(\Delta a / a) - (b / \lambda)] \qquad (10),$$

where $\alpha \approx 0.41$ is Saada's constant, G^* is the mean shear modulus and could be estimated as $G^* = G_{Cu}^* \cdot G_{Fe}^* / (G_{Cu}^* + G_{Fe}^*)$. λ is the average spacing of the interface

dislocation array (λ=25 nm). $\Delta a / a$ is the mismatch strain (~ 2.94% for Cu/Fe (bcc Fe) with K-S type of interface). The term in bracket is the residual elastic strain parallel to the interface plane caused by lattice mismatch. Then the estimated hardness by lattice mismatch from Eq.(10) is ~ 2 GPa.

The second term, named Koehler stress, τ_k^* comes from the differences in elastic moduli and maximum τ_k^* could be obtained by [8],

$$\sigma_{max} \cong R\mu_1 \sin\theta / 8\pi \qquad (11),$$

where $R = (\mu_2 - \mu_1)/(\mu_2 + \mu_1)$, μ_2 is the modulus of high-elastic-constant material and μ_1 is the modulus of low-elastic-constant material. θ is the angle between the slip plane and the interface. Assuming $\sin\theta$=0.81664, we can estimate hardness by modulus difference is ~ 3 GPa. As a result, we can obtain the calculated peak hardness is ~ 5 GPa. This is consistent with the plateau hardness we obtained. The peak hardness is similar between Cu/Ni (100) and Cu/Fe (100) multilayer, since the mismatch strain and modulus difference are very similar in both systems.

(c) Softening and twining induced strengthening (when h < 2.5 nm).

At this length scale, the hardnesses of Cu/Fe (111) and (100) have clearly different dependence on layer thickness. Softening was observed in Cu/Fe (100), similar to that in Cu/Ni (100) [5]. Softening could be explained by the formation of fully coherent interface and diminishing Koehler stress (as the dislocation core radius is comparable to h). The hardness of Cu/Fe 0.75 nm multilayer on Si (100) substrate was ~ the rule-of-mixture hardness of single layer Cu and Fe films. In contrast, the hardness of Cu/Fe 0.75 nm with (111) texture remained high, ~ 4.7 GPa. The retention of high hardness is related to the formation of high density twins which have an average twin spacing of ~ 6 nm. In Eq. (8), assuming $\alpha = 0.16$, and use the twin thickness (6 nm) and μ=48 GPa (Cu), we obtain a calculated hardness value of ~ 4.6 GPa, similar to experimental observations.

In conclusion, we studied strengthening mechanisms of Cu/Fe multilayers with various individual layer thicknesses on Si (100) and Si (110) substrates. K-S and N-W orientation relationships were identified along layer interfaces. When h > 25 nm, the

nanocolumn grain size in Fe is smaller than h, and is the primary parameter that dominates the strength of multilayers. A plateau of hardness is achieved when h = 2.5 - 25 nm, and can be explained by interface barrier strength model. Fully coherent interfaces were achieved at h of 0.75 nm in both sets of multilayers. The hardness of (111) textured Cu/Fe 0.75 nm multilayer remains high due to the formation of a large amount of nanotwins, wherein (100) textured Cu/Fe, significant softening was observed due to the formation of fully coherent layer interface and diminishing Koehler stress.

References

[1]   Embury JD, Hirth JP. Acta Metall 1994;42:2051.

[2]   Misra A, Krug H. Adv Eng Mater 2001;3:217.

[3]   Anderson PM, Foecke T, Hazzledine PM. MRS Bull 1999;24:27.

[4]   Misra A, Verdier M, Lu YC, Kung H, Mitchell TE, Nastasi M, et al. Scripta Mater 1998;39:555.

[5]   Liu Y, Bufford D, Wang H, Sun C, Zhang X. Acta Mater 2011;59:1924.

[6]   Wang J, Misra A. Curr Opin Solid State Mater Sci 2011;15:20.

[7]   Petch NJ. J Iron Steel Inst 1953;174:25.

[8]   Koehler JS. Phys Rev B 1970;2:547.

[9]   Rao SI, Hazzledine PM. Phil Mag A 2000;80:2011.

[10]   Zhang X, Misra A, Wang H, Shen TD, Nastasi M, Mitchell TE, et al. Acta Mater 2004;52:995.

[11]   Misra A, Hirth JP, Hoagland RG. Acta Mater 2005;53:4817.

[12]   Li X, Wei Y, Lu L, Lu K, Gao H. Nature 2010;464:877.

[13]   Lu K, Lu L, Suresh S. Science 2009;324:349.

[14]   Zhu YT, Wu XL, Liao XZ, Narayan J, Kecskés LJ, Mathaudhu SN. Acta Mater 2011;59:812.

[15]   Misra A, Verdier M, Kung H, Embury JD, Hirth JP. Scripta Mater 1999;41:973.

[16]   Pande CS, Rath BB, Imam MA. Mater Sci Eng A 2004;367:171.

[17]   D. Nix W. Mater Sci Eng A 1997;234–236:37.

[18]   Misra A, Zhang X, Hammon D, Hoagland RG. Acta Mater 2005;53:221.

[19]   Zhang JY, Niu JJ, Zhang X, Zhang P, Liu G, Zhang GJ, et al. Mater Sci Eng A

2012;543:139.

[20]   Niu JJ, Zhang JY, Liu G, Zhang P, Lei SY, Zhang GJ, et al. Acta Mater 2012;60:3677.

[21]   Fu EG, Li N, Misra A, Hoagland RG, Wang H, Zhang X. Mater Sci Eng A 2008;493:283.

[22]   Wei Q, Misra A. Acta Mater 2010;58:4871.

[23]   Wang J, Hoagland RG, Hirth JP, Misra A. Acta Mater 2008;56:5685.

[24]   Hoagland RG, Hirth JP, Misra A. Phil Mag 2006;86:3537.

[25]   Huang B, Ishihara KN, Shingu PH. J Mater Sci Lett 2001;20:1669.

[26]   Gao J, Wu ZL, Zhang ZP, Cao BS, Lei MK. Key Eng Mater 2008;373-374:104.

[27]   Shamsutdinov NR, Böttger AJ, Tichelaar FD. Scripta Mater 2006;54:1727.

[28]   Lloyd SJ. J Magn Magn Mater 1999;198–199:671.

[29]   Lee DW, Ryan DH, Altounian Z, Kuprin A. Phys Rev B 1999;59:7001.

[30]   Tu KN, Mayer JW, Feldman LC. Electronic thin film science: for electrical engineers and materials scientists. New York: Macmillan, 1992.

[31]   Lloyd SJ, Dunin-Borkowski RE. Phys Rev B 1999;59:2352.

[32]   Lu SH, Quinn J, Tian D, Jona F, Marcus PM. Surf Sci 1989;209:364.

[33]   Zhu YT, Liao XZ, Wu XL. Prog Mater Sci 2012;57:1.

[34]   Li BQ, Sui ML, Mao SX. J Mater Sci Technol 2011;27:97.

[35]   Freund LB, Suresh S. Thin Film Materials: Stress, Defect Formation and Surface Evolution. Cambridge: Cambridge University Press, 2004.

[36]   Liu Y, Bufford D, Rios S, Wang H, Chen J, Zhang JY, et al. J Appl Phys 2012;111:073526.

[37]   Zhang X, Misra A, Wang H, Shen TD, Swadener JG, Embury JD, et al. J Mater Res 2003;18:1600.

[38]   Zhu XF, Li YP, Zhang GP, Tan J, Liu Y. Appl Phys Lett 2008;92:161905.

II. 4. Radiation damage in helium irradiated Cu/Fe multilayers (in preparation)

FCC/BCC Cu/Fe mulatilyers were subjected to He ion irrraidaiton. Cu/Fe multilayers were fabricated by magnetron sputtering. The deposition rate is 0.5 nm/s for Fe and ~ 0.33 - 1.1 nm/s for Cu. The individual layer thickness varies from 0.75 to 100 nm on Si (100) substrate, and from 0.75 to 200 nm on Si (110) substrates.

The stopping and range of ions in matter (SRIM) computer code was used to simulate the displacement and He concentration profile, as shown in Fig. 4.1. The He concentration reaches a peak value of ~3.5 at.% at a depth of ~350 nm. The peak irradiation damage is ~ 5.5 displacements per atom (dpa) at a depth of ~300 nm. The radiation zone extends to ~530 nm underneath flm surface.
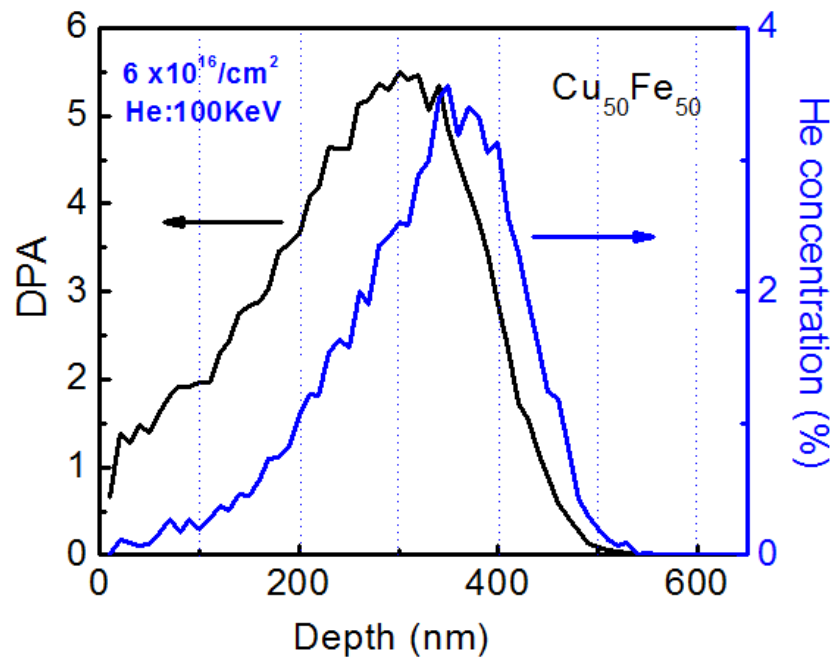

Figure 4.1 The depth profile of radiation damage in unit of displacements per atom (dpa) and helium concentration obtained from SRIM simulation of $Cu_{50}Fe_{50}$ alloy subjected to He ion irradiation at100 keV with a total fluence of 6×10^{16} ions/cm^2.
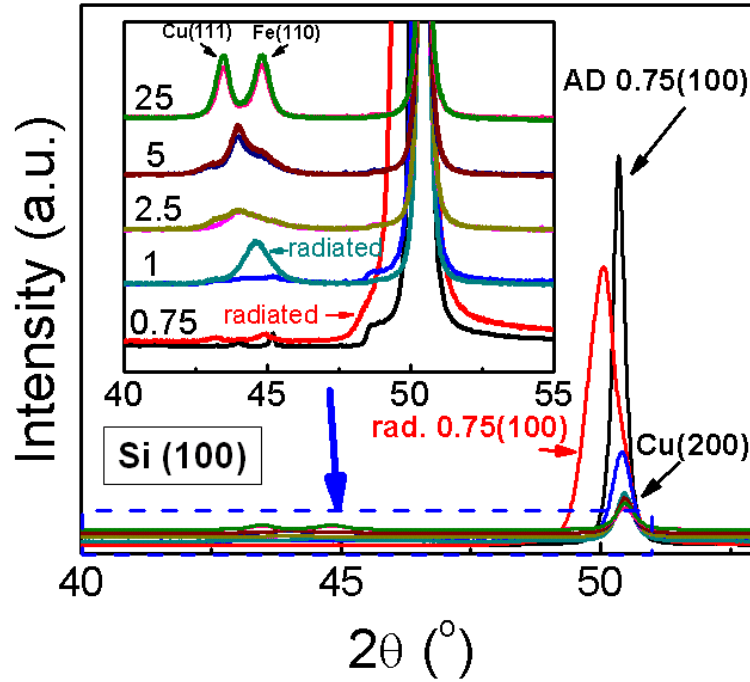
Figure 4.2. XRD patterns of Cu/Fe multilayers on Si (100) substrates show evident peak shift in certain specimens (Cu/Fe 0.75 nm) after He ion irradiation, whereas most other specimens have insignificant variation of XRD profiles.

Fig. 4.2 shows the XRD patterns of Cu/Fe multilayers on Si (100) before and after He radiation. When h > 1nm, the XRD curves before and after radiation overlap, that is the intensities and peak positions before and after radiation did not change significantly. When h = 1 nm, the intensity of FCC (200) peak decreases and a new peak appears between Cu (111) and Fe (110). When h = 0.75 nm, the FCC (200) peak shifts prominently to the left, indicating radiation induced out-of-plane lattice expansion. Hence in-plane compressive stress was developed after radiation.

Fig. 4.3 shows the XRD patterns of Cu/Fe multilayers on Si (110) before and after He ion irradiation. Radiation induces insignificant variation of XRD profiles when h = 1 – 200 nm, as shown in Fig. 4.3a. No FCC (200) peak was observed after radiation. When h = 0.75 nm, an obvious peak shift and shape change were observed, as shown in Fig. 4.3b. The FCC (111) peak of irradiated Cu/Fe 0.75 nm multilayer was decomposed into three peaks, labeled as D1, D2 and D3. Detailed examination is underway to interpret

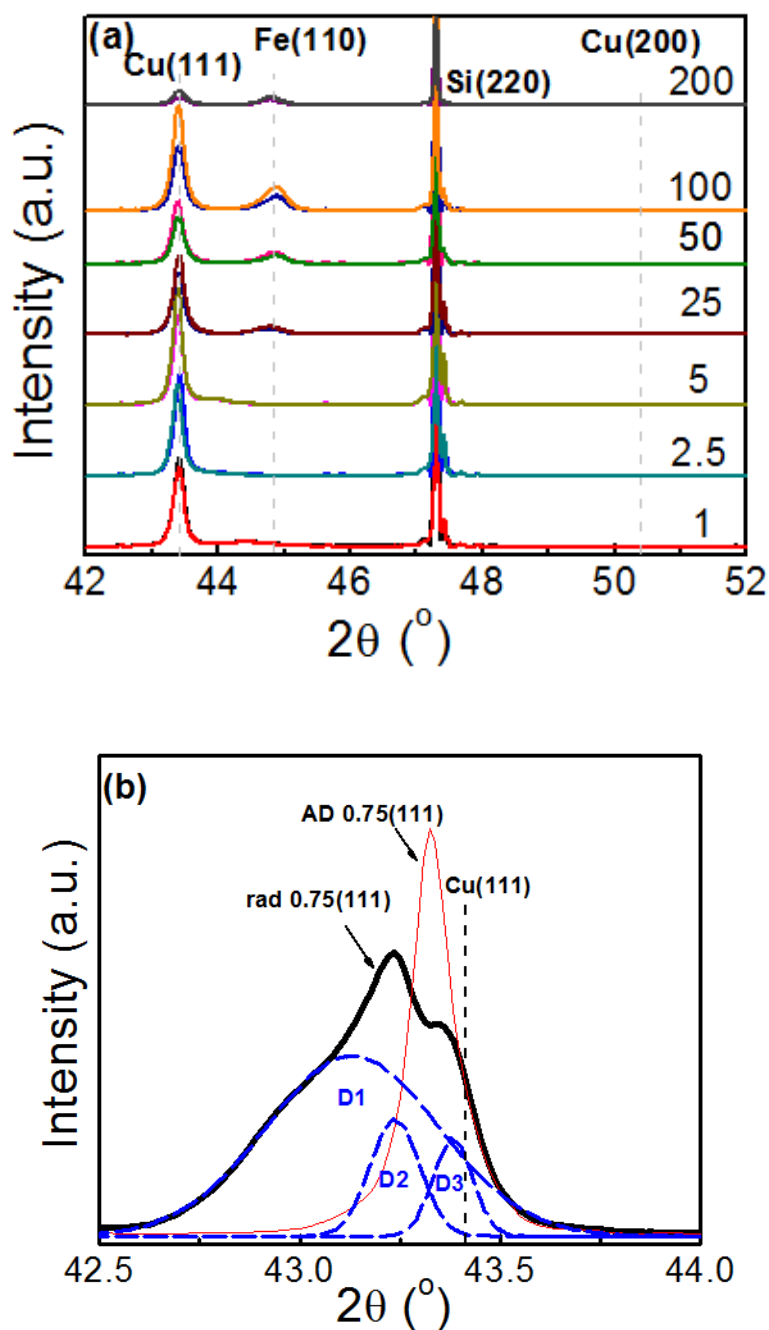61

radiation induced distortion in this multilayer.

Figure 4.3. XRD patterns of Cu/Fe multilayers deposited on Si (110) substrates before and after He radiation. (a) There was insignificant variation of peak position and peak intensity when h = 1 – 200 nm. (b) When h = 0.75 nm, significant peak broadening was observed after radiation. The peak can be deconvoluted into three peaks, D1-D3.
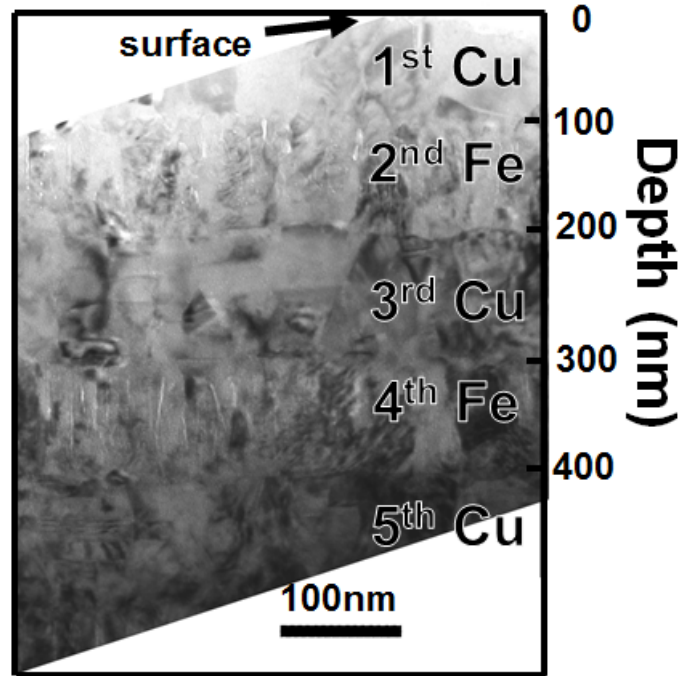
Figure 4.4. A cross-sectional TEM micrograph of Cu/Fe 100 nm multilayer on Si (110) substrate after He ion irradiation. Layer interfaces remained intact after radiation.

Fig. 4.4 shows the He ion irradiated Cu/Fe 100nm multilayer on Si (110). Layer structure was not destroyed by radiation. Columnar nano grains in Fe layers retained after radiation. Details of each layer are displayed in Fig. 4.5a-d.
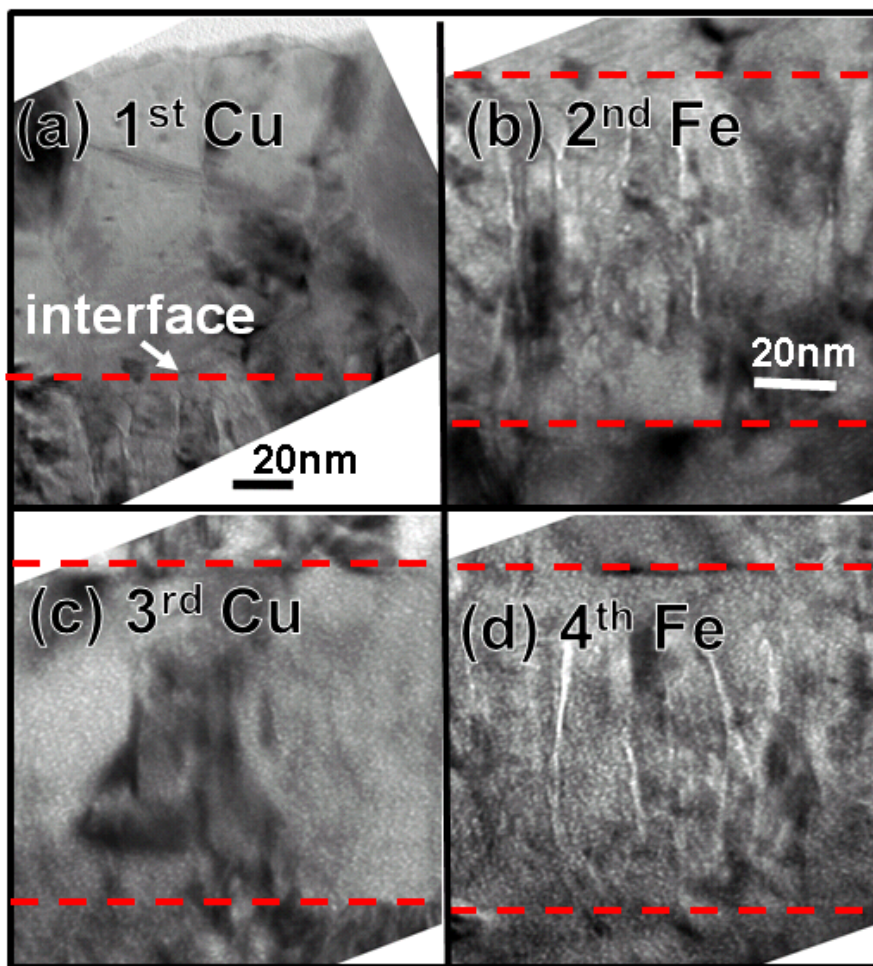
Figure 4.5 XTEM micrograph of Cu/Fe 100 nm film on Si (110) substrate after He ion irradiation at high magnification. (a) Little bubbles were observed in the 1st layer, Cu. (b) Bubbles in the 2nd layer (Fe) appeared to align along layer interfaces. (c) Bubble density increased rapidly in the 3rd layer (Cu). (d) A high density of He bubbles were observed in the 4th layer composed of Fe.

Fig. 4.5a-d show individual layers in Fig. 4.4 at higher magnification. Bubbles were observed near the 1st Cu/Fe interface. In the 2nd layer, a large number of bubbles retain in the iron layer. More bubbles were observed in 3rd layer and bubble density increased significantly in 4th (Fe) layer. Bubbles appeared to algin along grain boundaries.
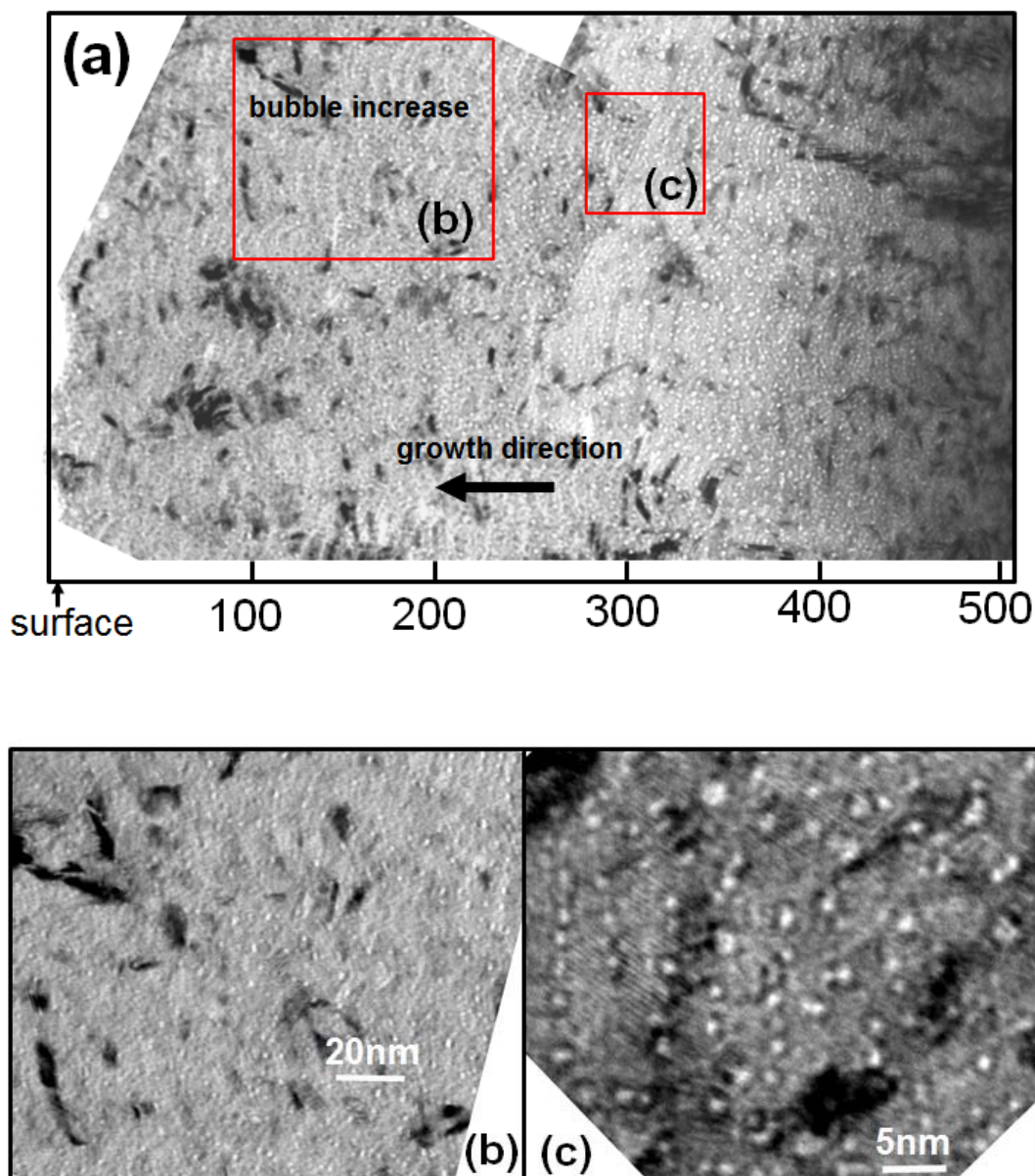
Figure 4.6 (a) XTEM micrograph of panoramic view of Cu/Fe 5nm on Si (110) substrate after He ion irradiation. (b) and (c) are magnified view of red box in (a). High density He bubbles was observed along layer interfaces.

Fig. 4.6 shows XTEM image of irradiated Cu/Fe 5nm multilayers on Si (110). Fig. 4.6a shows the low magnification panoramic view of the irradiated area. The variation of bubble density across the specimen is evident. No bubbles were observed beyond the depth of 450 nm, indicating the end of radiation damage zone. Fig. 4.6b shows the

surface area at the depth ~100 nm. Bubbles decorated along layer interfaces. Fig. 4.6c shows most bubbles stayed along Cu/Fe interfaces.
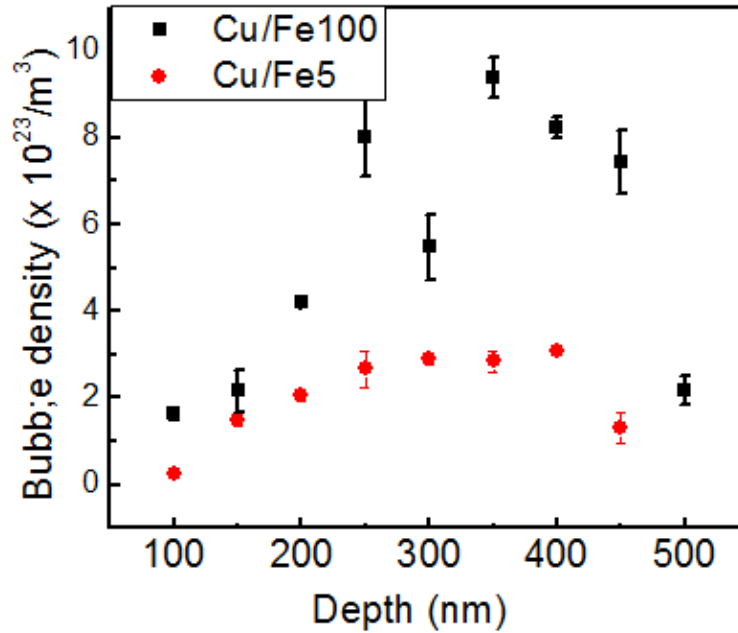

Figure 4.7. The comparison of depth dependent He bubble density between the irradiated Cu/Fe 100 and Cu/Fe 5 nm multilayers on Si (110) substrate. The density of He bubbles in Cu/Fe 5 nm film is much lower than that in Cu/Fe 100 nm film.

Fig. 4.7 compares the evolution of bubble density versus depth in radiated Cu/Fe 100 and Cu/Fe 5 nm multilayers obtained from microscopy studies. The bubble density of Cu/Fe 5 nm film is a factor of ¼ of that in Cu/Fe 100 nm film. The reduction of He bubble density is likely a consequence of layer interface assisted recombination of point defects. Point defects are likely to segregate to layer interfaces, at which their diffusivity is greater than that in crystal lattices. The higher diffusivity of point defects along interface shall promote the recombination (annihilation) of these point defects.
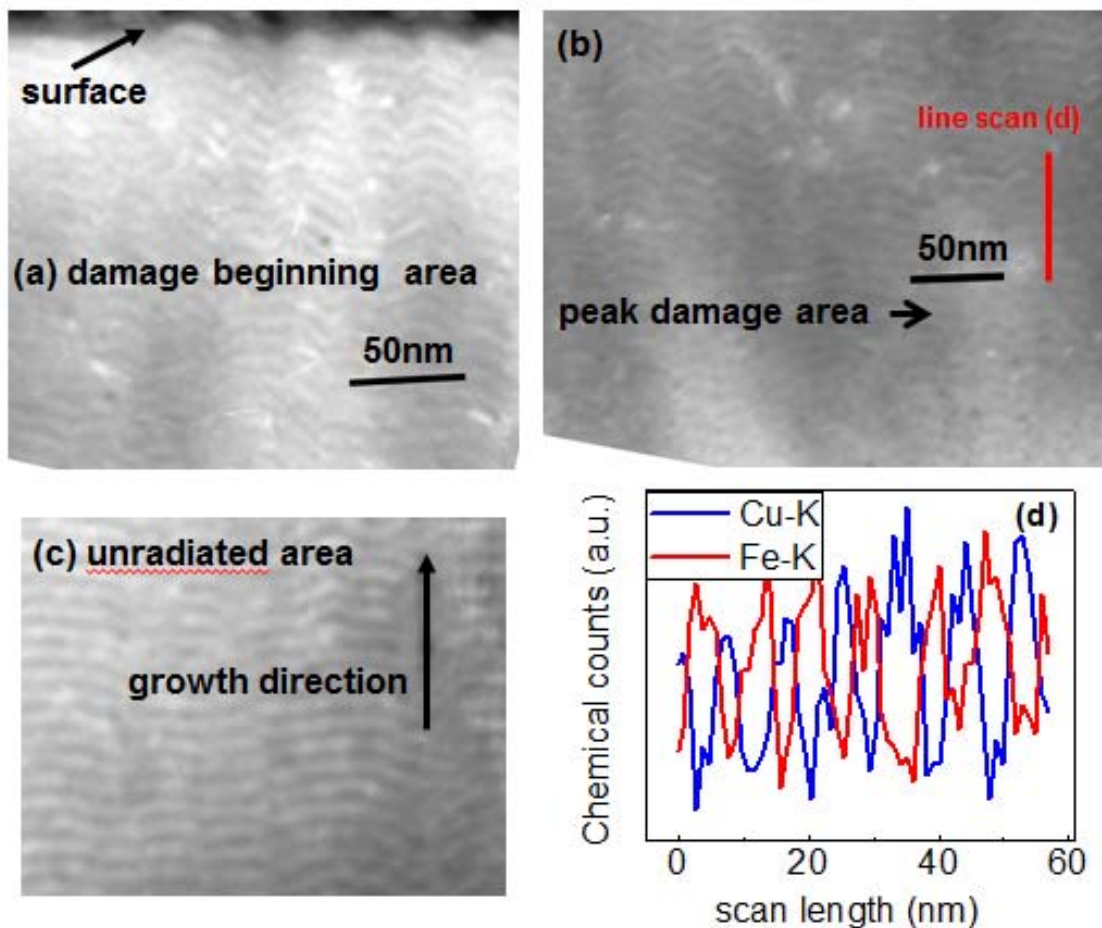
Figure 4.8 Cross-sectional STEM micrographs of Cu/Fe 5nm film on Si (110) substrate display (a) initial irradiated area; (b) peak damage area; and (c) unirradiated area. Layer interface remained chemically unmixed after high dose radiation. (d) Compositional line profile of peak damage area in (b).

Fig. 4.8a-b shows the STEM images of the surface area and peak damage area of He ion irradiated Cu/Fe 5 nm on Si (110). Fig. 4.8c shows the as-deposited specimen for comparison. To confirm that the layer structure still exists after radiation, compositional line profile was collected at the peak damage area, as indicated by the red line in Fig. 8b. Fig. 4.8d confirms the layer structure remained intact after radiation.
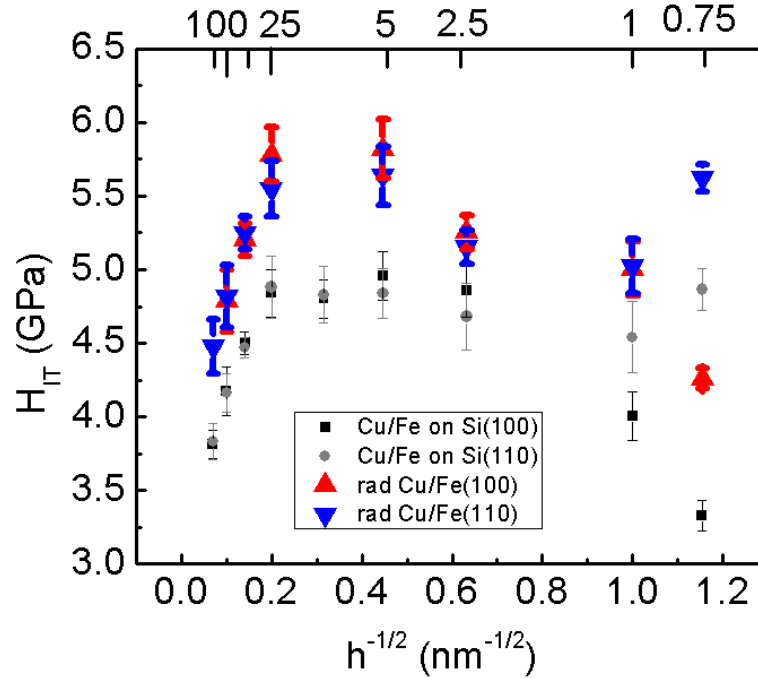
Figure 4.9. Plot of hardness versus $h^{-1/2}$ of Cu/Fe multilayers on Si (100) and (110) before and after He ion irradiation. Radiation hardening is evident in multilayers at large h, whereas hardening is absent in Cu/Fe 2.5 and Cu/Fe 1 nm film. The radiation hardening in Cu/Fe 0.75 nm is of particular interest as it reveals that there may be an optimum layer thickness that assists the alleviation of radiation damage.

Fig. 4.9 shows the hardness versus $h^{-1/2}$ plot of Cu/Fe multilayers on Si (100) and (110) before and after He radiation. Radiation induced hardening was observed for all multilayers. When h > 2.5nm, radiation hardening did not change significantly. This might be related to the absorption of point defects by nanoscale columnar grains in Fe as well as layer interfaces. When h = 2.5 and 1 nm, radiation hardening reaches minimum value. Radiation hardening increases with further decrease of h. When h = 0.75 nm, radiation hardening is significant. At this layer thickness, the interface became fully coherent. Coherent interfaces may be less effective in alleviation of radiation induced damage than incoherent immiscible layer interfaces. The detailed mechanisms of radiation induced damage hardening are under investigation.

II. 5. *In situ* evidence of defect cluster interaction with grain boundary in nanocrystalline Nickel (Materials and Metallurgical Transaction, A, 2012)

Irradiation of metals by high energy particles generates interstitial-vacancy Frenkel pair. These individual point defects can be lost through mutual recombination of interstitials and vacancies or reaction with defect sinks, such as neutral sinks (grain boundaries, voids), biased sinks (dislocations) and variable sinks (impurity atoms and coherent precipitates) [1]. Meanwhile, these point defects can aggregate to form defect clusters, which can be dislocation loops, voids or stacking fault tetrahedron [2]. An important defect cluster population can result in significant changes in mechanical, electrical and magnetic properties. How to mitigate the formation of the defect clusters by irradiation and thus enhance the irradiation tolerance of materials is an important subject that is far from being well solved. The initial microstructure of the metals is believed to play an important role in the nucleation and migration of the point defects and defect clusters. For instance, the addition of some impurities and cold working in austenitic stainless steel showed a reduced swelling under neutron radiation at 400°C [3]. Oxide dispersed strengthened ferritic steels with yttrium oxide particles showed a limited void density under electron irradiation [4]. Immiscible layer interfaces, such as Cu/Nb [5], Cu/Mo [6] and Cu/V [7], can effectively mitigate swelling, lattice distortion and radiation hardening.

Grain boundary structure is considered as an effective neutral sink for irradiation-induced defects [8], [9], [10]. With large volume fraction of grain boundaries, a substantial reduction of radiation damge should be expected in nanocrystalline materials compared to the conventional coarse grained materials. A few simulation studies have been reported about the GB impact on radiation behaviors of nc metals. Samaras et al. observed significant atomic migration towards the surrounding grain boundary structure during thermal spike stage in nc Ni by using molecular dynamic simulations [10]. Bai et al. used molecular dynamic simulation to demonstrate that grain boundary acts as a defect sink as well as defect source, which emit interstitials to annihilate the nearby vacancies in the grain [12]. Experimental studies also showed that irradiation-induced damage was significantly reduced in nanocrystalline metals. Singh et al. found that grain refinement can delay the void nucleation, lower the void

concentration and mitigate the void swelling in stainless steel during electron radiation [13]. Rose et al. have reported that the defect cluster density in Kr ion irradiated nc Pd and ZrO_2 was dramatically reduced by reducing the grain size below 50 nm, and no defect cluster could be detected in nc Pd (< 30 nm) and nc ZrO_2 (< 15 nm) grains[10]. NC $MgGa_2O_4$ and TiNi revealed enhanced amorphization resistance subjected to 300 keV Kr^{++} ions and 1.5 MeV Ar^+ ions, respectively [14],[15]. Chimi et al. measured the electrical resistivity of irradiated nc gold and found that enlarged defect accumulation with decreasing temperature [[16]]. Radiguet et al. performed iron ion irradiation on nc 316 stainless steel with grain size of 40 nm at 350°C and no intragranular precipitates or segregation was observed [[17]].

Grain growth of nc metals under irradiation was reported in the literatures. Voegeli et al. performed the MD simulation for nc Ni with grain size in the range of 5-10 nm and indicated that the grain growth occur when the thermal spike volume is larger than the grain volume or cross the GB structure [[18]]. Kaoumi et al. reported the grain growth of nc Au, Pt, Cu, Zr and Zr-Fe under irradiation even at temperature down to 20 K, and average grain size follows an exponential law with irradiation dose with exponent of ~ 3 [[19]]. Grain growth in irradiated Au, Ge and Si thin films exhibited a weakly temperature dependent growth rate, which increased linearly with damage energy [[20]]. Grain growth was also found in nc 316 stainless steel after irradiation up to 5 dpa at 350 °C [[17]]. Liu et al. found that grain size of Pd thin film increase from 9 nm to 60 nm after ion irradiation at room temperature, and suggested that irradiation induced grain growth may be related to the thermal spike generated by irradiation [[21]].

In this paper, we report on the direct observation of grain boundary impact on the defect cluster formation and migration in nc Ni during Kr^{++} ion irradiation under TEM. The evolution of defect cluster density, defect cluster diameter and grain size in nc and CG Ni was examined by *in situ* irradiation.

The fcc nc Ni was synthesized by pulse electrodeposition, the procedures can be obtained somewhere else [[22]].   Annealing of the nc Ni in a vacuum furnace at 400°C for 2 hours was used to coarsen the nc Ni. The plane view TEM sample disks with 3 mm diameter were prepared by ion milling and subsequent ion polishing. Convergent beam electron diffraction (CBED) technique [[23]] was used to estimate the Ni foil thickness.

SRIM simulation [[24]] was used to estimate the displacement profile and Kr^{++} ion distribution under irradiation. Displacement energy for Ni, 40 eV, was used to calculate the displacement per atom. The results show that all the Kr^{++} ions with energy of 1 MeV will penetrate through the first 200 nm, resulting that displacement contains in the TEM sample foil where the Kr^{++} ion concentration can be neglected. *In situ* Kr^{++} ion irradiation with energy of 1 MeV was conducted at room temperature in the Intermediate Voltage Electron Microscope (IVEM) at Argonne National Laboratory, USA [[25]]. The electron beam was operated at 200 kV and kept on during irradiation in order to record the microstructure evolution. The average irradiation rate is 0.003 dpa/s.

Microstructure and defect evolution

Figure 5.1 a shows the initial microstructure of the coarse grained fcc Ni with average grain size of 2.5 μm. Figure 5.1 b presents the microstructure of the nanocrystalline fcc Ni, the average grain size is ~ 55 nm.
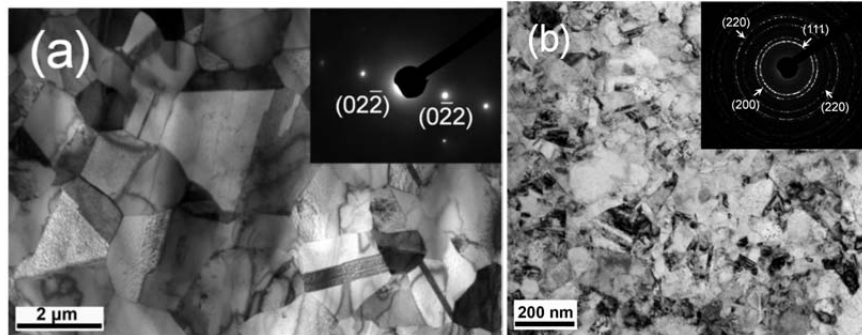

Figure 5.1 (a) Coarse grained Ni with average grain size of 2.5 μm. (b) Nanocrystalline Ni with average grain size of 55 nm.

Figure 5.2 shows the *in situ* Kr^{++} ion irradiation of NC Ni to a dose from 0.56 to 0.68 dpa at room temperature within 40 seconds. The arrows show the individual dislocation loops, each arrow represent one loop. Due to the lower energy barrier of interstitials for migration than vacancies, these mobile dislocation loops are more likely to be the interstitial loops. We set the first slot shot in the Figure 5. 2a as zero second. It was seen that there are three individual interstitial loops formed near the grain boundary. The closest distance between the grains in Figure 5.2a is 8.6 nm. After 13 seconds, these

individual loops combined together, and formed two small dislocation segments with length of each ~ 10 nm, as shown in Figure 5.2b. Figure 5.2 c shows the dislocation segments near the grain boundary preferentially diffuse towards the grain boundary, and the length of the dislocation segments significantly reduced. After 40 seconds, the dislocation segments were almost absorbed by the grain boundary nearby. The closest distance between the two grains was reduced to be 6.9 nm.
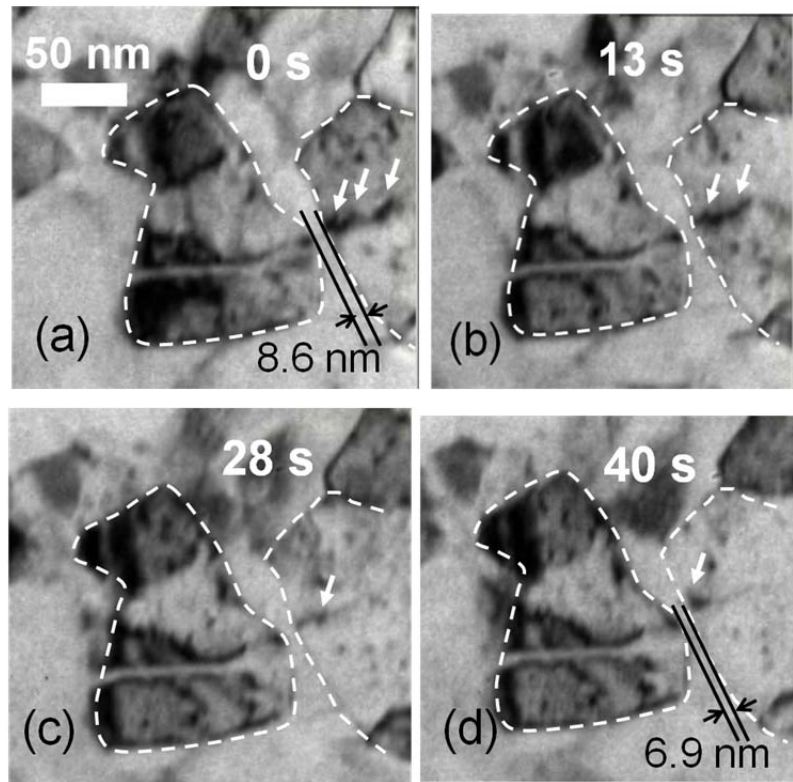

Figure 5.2 *In situ* Kr++ ion irradiation of NC Ni with dose from 0.56 to 0.68 dpa at room temperature. Interaction between grain boundary and interstitial loops is clearly observed. The arrows represent the dislocation loops. (a) Three individual dislocation loops are located near the grain boundary, and the closet distance between the two grains is 8.6 nm. (b) With 13 seconds, the loops combine and become two dislocation segments. (c) After 28 second, the dislocation segments diffuse towards the nearby grain boundary. (d) By 40 seconds, the closet distance between the two grains is reduced to be 6.9 nm. Gain boundary effectively suppresses the formation of dislocation networks and the growth of dislocation loops.
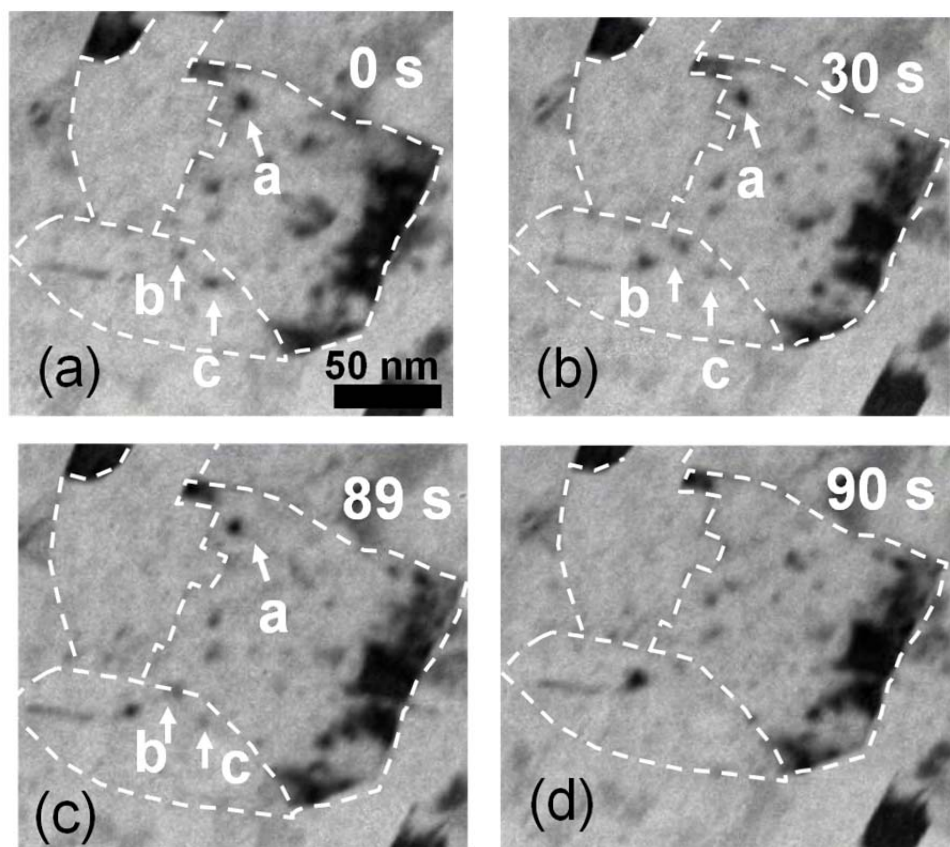
Figure 5.3 *In situ* Kr++ ion irradiation of NC Ni to a dose from 1.51 to 1.78 dpa at room temperature within 90 seconds. The migration of interstitial loops, a, b and c are tracked. (a) Three loops, a, b and c with diameter of 4.5 nm, 2.5 nm and 3.5 nm, respectively, are located near the grain boundaries. (b) The loops diffuse towards the grain boundary and diameters are also reduced. (c) The diameter of loop a is reduced to be 3.2 nm. (d) The loop a, b and c are trapped by the grain boundary.

Figure 5.3 shows the *In situ* Kr^{++} ion irradiation of NC Ni to a dose from 1.51 to 1.78 dpa at room temperature. In this scenario, the absorption of individual interstitial loops by grain boundary structure was observed. As shown in Figure 5.3 a, three individual interstitial loops, located near the grain boundaries, are tracked. The diameter of the loop **a**, **b** and **c** were 4.5 nm, 2.5 nm and 3.5 nm, respectively. With 30 seconds, the three loops diffused towards the nearby grain boundaries and the diameter of the loops tended to be reduced, as shown in Figure 5. 3 b. After 89 seconds, the loop a, **b** and **c** were diffusing towards the grain boundary. At 90 seconds, shown in Figure 5.3d, the loop **a** was suddenly sucked by the grain boundary.

Defect absorption mechanisms

Figure 5.4 presents the TEM images of coarse grained Ni after Kr[++] ion irradiation at room temperature to a dose of 1 dpa and 5 dpa. The black dots in the bright field image were considered as defect clusters, which were interstitial loops and vacancy loops. After radiation up to 1 dpa, the major radiation induced defects are the dislocation loops, while with a radiation dose of 5 dpa, the dislocation segments were generated. Up to a dose of 5 dpa, the defect cluster density is $\sim 1.76 \times 10^{23}/m^3$, and dislocation density increase from $\sim 2 \times 10^{12}/m^2$ to $\sim 7 \times 10^{13}/m^2$.
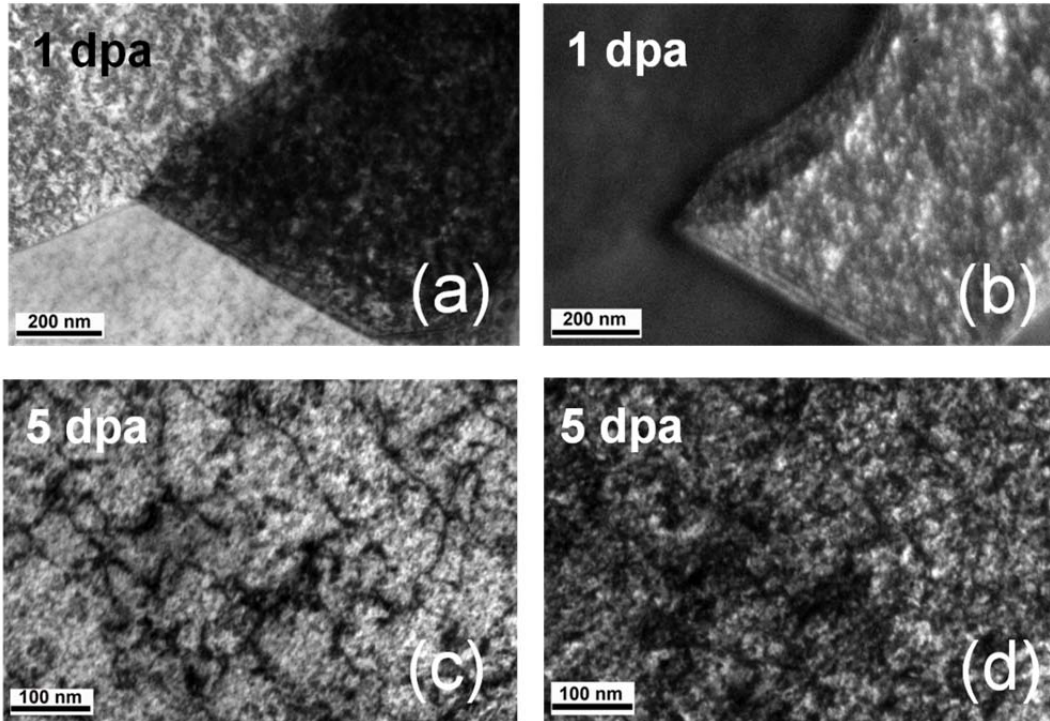

Figure 5.4 TEM images of coarse grained Ni after Kr++ ion irradiation at room temperature. (a) Kinetic bright field TEM image after radiation up to 1 dpa, the black dots are considered as the dislocation loops. (b) Dark field image after radiation to 1 dap. (c) Kinetic bright field TEM image with radiation to a dose of 5 dpa. Dislocation loops and dislocation segments are observed. Dislocation loop density is $\sim 1.76 \times 1023/m3$, and dislocation segment density increase from $\sim 2 \times 1012/m2$ to $\sim 7 \times 1013/m2$. (d) Dark filed image with radiation to a dose up to 5 dpa.

Figure 5.5 shows the bright field and dark field TEM images for irradiated nc Ni to a dose of 1 dpa and 5 dpa. Likewise, the black dots in the bright field image and the white dots in the dark field image were the dislocation loops. Compared with Figure 5.4, it is clearly seen that the defect cluster density becomes significantly lower and the defect cluster diameter also become smaller. After a dose of 5 dpa irradiation, the defect cluster density in nc Ni was measured to be $\sim 8.4 \times 10^{22}/m^3$, which was about 2 times lower than that in CG Ni. The defect cluster diameter in nc Ni and CG Ni were ~ 3.5 nm and 7.5 nm, respectively. In addition, no significant dislocation segments in irradiated nc Ni could be observed.
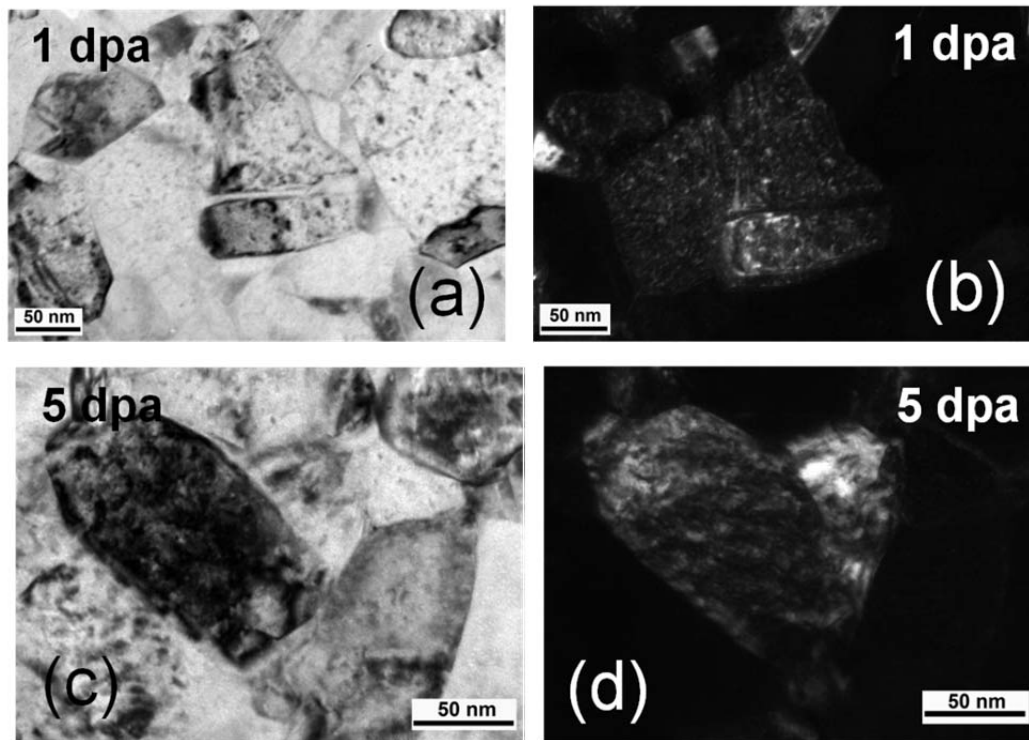
Figure 5.5 TEM images of nanocrystalline Ni after Kr++ ion irradiation at room temperature. (a) Bright field TEM image after radiation up to 1 dpa, dislocation loops are still observed. (b) Dark field image after radiation to 1 dap. (c) Kinetic bright field TEM image with radiation to a dose of 5 dpa. Dislocation loops are observed, but no significant dislocation networks generated. Dislocation loop density is $\sim 8.40 \times 10^{22}/m^3$. (d) Dark filed image with radiation to a dose up to 5 dpa.

Figure 5.6 shows the TEM image of nc Ni after 5 dpa irradiation. It is seen that no significant grain growth occur. The statistic grain size distribution shows that after radiation the average grain size slightly increased from 55 nm to 62 nm, the difference of which was negligible, and that the distribution of the grain size became slightly broader. Figure 5.7 illustrates the evolution of defect cluster density vs. irradiation dose. The defect cluster density increased dramatically at the beginning stage of irradiation, i.e. up to a dose of ~ 0.5 dpa, and then saturates to become stable until 5 dpa.
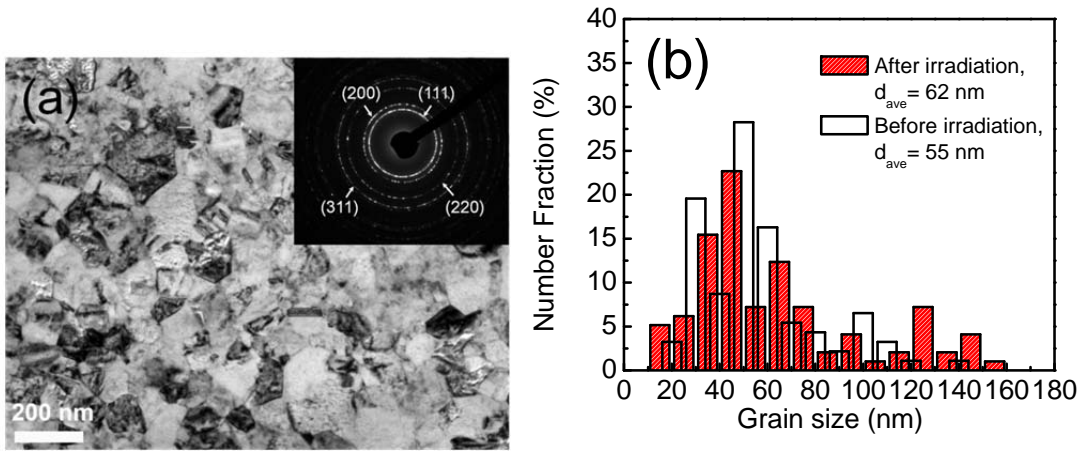
Figure 5.6 (a) Bright filed TEM image in a low magnification of NC Ni after Kr++ ion irradiation to a dose of 5 dpa at room temperature. (b) Statistic study indicates that there is no significant grain growth occurs after irradiation, and that the distribution of grain size becomes slightly broader.

Figure 5.7 Dislocation loop density (ρ_{loop}) as a function of dose. Dislocation loop density of CG and NC Ni increases with dose in the beginning stage and then saturates to certain level. After radiation to 5 dpa, the average loop density of CG Ni is about 2 times larger than that of NC Ni.

Figure 5.8 The plot of defect cluster diameter vs. dose. The defect cluster diameter in nc Ni increase at a slower rate, compared with that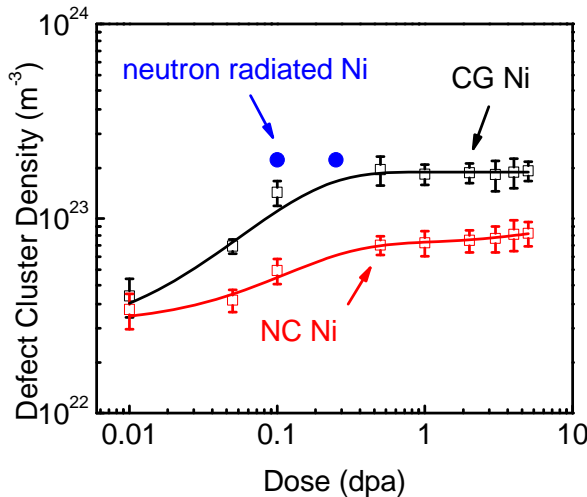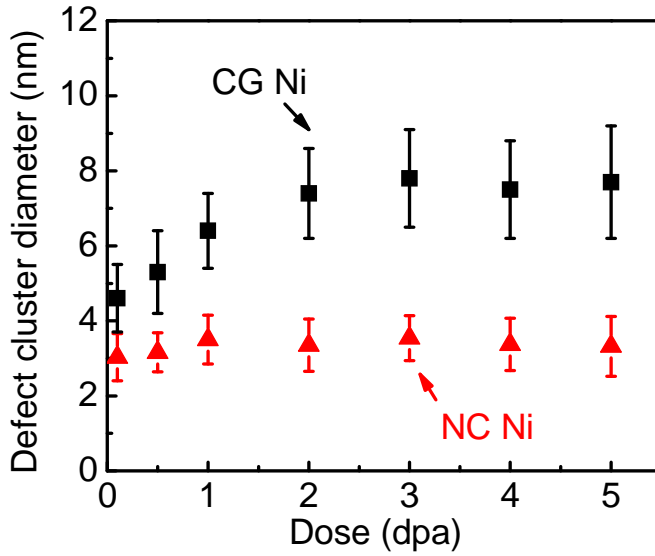 in CG Ni. To a dose of 5 dpa, the average dislocation loop diameter of NC Ni is ~ 3.5 nm, which is smaller than that of CG Ni, ~ 7.5 nm.

Figure 5.8 illustrates the growth of the defect cluster as a function of dose. In CG Ni, the defect cluster diameter increased with dose up to 2 dpa, and then saturates to ~ 7.5 nm, while in nc Ni, the defect cluster diameter saturated to ~ 3.5 nm very rapidly and the increasing stage was difficult to observe.

From the evolution of the defect density plot, we can clearly see that defect clusters density increase rate in nc Ni is much lower than in CG Ni, and that the saturated defect cluster density is also reduced by ~ 50% through grain refinement. These defect clusters are formed by the aggregation and collapse of the point defects, which are the interstitials and vacancies. Reducing the population of the point defects will lower the chance of forming defect clusters. The point defects can be lost either through recombination of interstitials and vacancies or by the reaction with defect sinks, such as grain boundary, dislocations, precipitate, etc. Here we assume the grain boundary is the only defect sinks in this case, the mathematical description of the concentration of the point defects ($C_\theta, \theta = i$ for interstitials and $\theta = v$ for vacancies) by chemical rate equations are [[1]]:

$$\frac{\partial C_\theta}{\partial t} = K - R_{\theta\theta'} C_\theta C_{\theta'} - S_{gb} D_\theta C_\theta$$

(1)

where t is the time, K is the atomic displacement rate; when $\theta = i$, then $\theta' = v$; D_i and D_v are the diffusion coefficients for interstitials and vacancies; R_{iv} is the recombination rate of interstitial and vacancy, $R_{iv} = 4\pi(D_i + D_v)r_{i,v}$, where $r_{i,v}$ assume 0.72 nm [[26]]; S_{gb} is the grain boundary sink strength, for nc Ni, $S_{gb} = 24/d^2$, where d is the grain size [[1]], and for CG Ni, $S_{gb} = 10^{15} m^{-2}$. The diffusion coefficients of interstitials and vacancies, D_i and D_v , are calculated based on the migration energy of interstitials and vacancies, E_i and E_v, respectively. For fcc Ni at 300K, $E_i = 0.14eV$ and $E_v = 1.3eV$ [[28]]. For the steady state concentration of interstitials and vacancies, C_i^s and C_v^s, setting $\dfrac{dC_i}{dt} = \dfrac{dC_v}{dt} = 0$, gives:

$$C_\theta = -\frac{S_{gb}D_{\theta'}}{2R_{iv}} + [\frac{K}{R_{iv}}(\frac{D_\theta}{D_{\theta'}}) + (\frac{S_{gb}D_{\theta'}}{2R_{iv}})^2]^{1/2}$$

(2),

With significant grain size difference in CG Ni (~2.5μm) and nc Ni (~ 55 nm), we can calculate the ratio of concentration of interstitials and vacancies in CG and nc Ni at steady state: $C_i^{CG}/C_i^{nc} \approx C_v^{CG}/C_v^{nc} = 7.87$. The concentration of interstitial and vacancy in CG Ni are ~ 8 times more than those in nc Ni, suggesting that the grain boundary structure in nc Ni can effectively reduce concentration of both interstitials and vacancies. From the microstructure evolution obtained from the in situ experiment, the density and diameter of dislocation loop in CG Ni is around two times more than that in nc Ni. For the loops on {111} planes, we estimate the number of point defect in each dislocation loop by using the relationship: $r_L = (\sqrt{3}a^2n/4\pi)^{1/2}$, where r_L is the dislocation loop radius and a is the lattice parameter [[29]]. Thus, we estimate that the concentration ratio of point defects, which form the dislocation loops, in CG and nc Ni is ~ 8, which is in the same order of magnitude we calculated based on the model above.

The grain boundary structure, on the one hand, serves as defect sinks to trap the interstitials and vacancies produced by primary bombarding, lowering the density of point defects. On the other hand, the grain boundary structure can also act as defect

sources, which can emit interstitials and vacancies to combine with the defect clusters in the bulk. From the *in situ* video, we clearly observed that the grain boundary effectively suppresses the growth of dislocation loops and only absorb the dislocation loops near the grain boundaries. The average velocity of the defect clusters sucked into the grain boundaries is ~ 5 nm/s. Based on the Brownian diffusion model, we estimate the diffusivity D=10.5nm^2/s. By using $D = D_0 \exp(-\dfrac{E^m}{kT})$, where $D_0 = 10^{13} n^{-0.65}$, can calculate the migration energy for the defect cluster is ~ 0.2 eV. This value is very close to the calculated activation energy of Ni, ~ 0.2 eV, for the motion of dislocation loop with ~ 200 interstitials, which is ~ 3.5 nm in diameter [[30]].
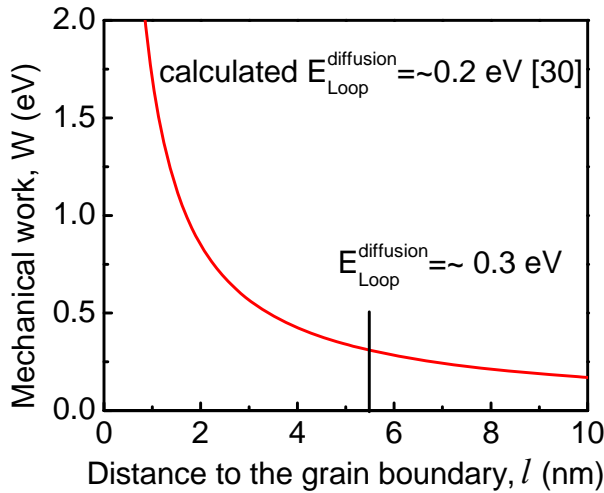

Figure 5.9. Mechanical work versus distance from dislocation loop to grain boundary, *l*. The mechanical work is associated with the dislocation loop climb by the emission of vacancy from grain boundary. From the in situ TEM, the average *l* for the dislocation loop trapped to the grain boundary is ~ 5.5 nm. The activation energy for the dislocation loop near the grain boundary is estimated to be ~ 0.3 eV.

When the mechanical work done by the climb force exceeds the diffusion barrier energy of the dislocation loop near the grain boundary, the loops will be sucked into the grain boundary. Here we simple consider the dislocation loop near grain boundary as screw dislocation since the self energy per unit length of the dislocation is lower in the screw orientation that that in the edge orientation. We can calculate the climb force, F, for the dislocation to move towards the grain boundary by using the image force between screw dislocation and the grain boundary. The image force per unit length is given by [[26]]

$$\frac{F}{L} = -\frac{Gb^2}{4\pi d} \tag{3}$$

where G is the shear modulus, 76 GPa , b is the Burgers vector, l is the distance between the dislocation loop and the grain boundary. If we assume the grain boundary as ideal vacancy sinks. The mechanical work per unit length corresponding to the climb is expressed as

$$\frac{W}{L} = -\frac{F}{L}b$$

(4)

Figure 5.9 shows the mechanical work associated with dislocation loop climb through the emission of vacancy from the grain boundary as a function of the distance. As the distance increase, the climb force reduces and thus the mechanical work, leading to the less impact of grain boundary on the dislocation loop. We observed that in the nc Ni, the average trapped distance between dislocation loop and grain boundary is ~ 5.5 nm. At this critical point, the migration energy for the dislocation loop is ~ 0.3 eV, which is slightly higher than the experimental value. The difference comes from the overestimation of the interaction force between grain boundary and dislocation loops.

The interaction of ion irradiation-induced defect clusters with grain boundaries was clearly observed at room temperature by using *in situ* Kr^{++} ion irradiation under TEM. The grain boundary effectively absorbed the defect clusters and suppressed the growth of defect clusters and formation of dislocation networks. In irradiated nc Ni up to 5 dpa, the density and diameter of defect clusters were around half of those in CG Ni, and no clear dislocation segments were generated. No significant grain growth occurred in nc Ni during the ion irradiation.

References

[1] G. Was, Fundamentals of Radiation Materials Science, Springer, New York, 2007.

[2] H. R. Brager and J. L. Straalsund, "Defect development in neutron irradiated type 316 stainless steel", Journal of Nuclear Materials 46 (1973), 134-158.

[3] E. Wakai, N. Hashimoto, J. P. Robertson, T. Sawai, and A. Hishinuma, "Swelling of cold-worked austenitic stainless steels irradiated in HFIR under spectrally tailored conditions", Journal of Nuclear Materials 307-311 (2002), 352-356.

[4] J. Saito, T. Suda, S. Yamashita, S. Ohnuki, H. Takahashi, N. Akasaka, M. Nishida, and S. Ukai, "Void formation and microstructural development in oxide dispersion strengthened ferritic steels during electron-irradiation", Journal of Nuclear Materials 258–263, Part 2 (1998), 1264-1268.

[5] X. Zhang, N. Li, O. Anderoglu, H. Wang, J. G. Swadener, T. Höchbauer, A. Misra, and R. G. Hoagland, "Nanostructured Cu/Nb multilayers subjected to helium ion-irradiation", Nuclear Instruments and Methods in Physics Research Section B: Beam Interactions with Materials and Atoms 261 (2007), 1129-1132.

[6] N. Li, J. J. Carter, A. Misra, L. Shao, H. Wang, and X. Zhang, "The influence of interfaces on the formation of bubbles in He-ion-irradiated Cu/Mo nanolayers", Philosophical Magazine Letters 91 (2011), 18-28.

[7] E. G. Fu, A. Misra, H. Wang, L. Shao, and X. Zhang, "Interface enabled defects reduction in helium ion irradiated Cu/V nanolayers", Journal of Nuclear Materials 407 (2010), 178-188.

[8] H. Trinkaus and B. N. Singh, "Helium accumulation in metals during irradiation - where do we stand?", Journal of Nuclear Materials 323 (2003), 229-242.

[9] T. D. Shen, "Radiation tolerance in a nanostructure: Is smaller better?", Nuclear Instruments and Methods in Physics Research Section B: Beam Interactions with Materials and Atoms 266 (2008), 921-925.

[10] M. Rose, A. G. Balogh, and H. Hahn, "Instability of irradiation induced defects in nanostructured materials", Nuclear Instruments and Methods in Physics Research Section B: Beam Interactions with Materials and Atoms 127-128 (1997), 119-122.

[11] M. Samaras, P. M. Derlet, H. Van Swygenhoven, and M. Victoria, "Computer Simulation of Displacement Cascades in Nanocrystalline Ni", Physical Review Letters 88 (2002), 125505.

[12] X.-M. Bai, A. F. Voter, R. G. Hoagland, M. Nastasi, and B. P. Uberuaga, "Efficient Annealing of Radiation Damage Near Grain Boundaries via Interstitial Emission", Science 327 (2010), 1631-1634.

[13] B. N. Singh, "Effect of grain size on void formation during high-energy electron irradiation of austenitic stainless steel", Philosophical Magazine 29 (1974), 25 - 42.

[14] T. D. Shen, S. Feng, M. Tang, J. A. Valdez, Y. Wang, and K. E. Sickafus, "Enhanced radiation tolerance in nanocrystalline MgGa$_2$O$_4$", Applied Physics Letters 90 (2007), 263115.

[15] A. R. Kilmametov, D. V. Gunderov, R. Z. Valiev, A. G. Balogh, and H. Hahn, "Enhanced ion irradiation resistance of bulk nanocrystalline TiNi alloy", Scripta Materialia 59 (2008), 1027-1030.

[16] Y. Chimi, A. Iwase, N. Ishikawa, M. Kobiyama, T. Inami, and S. Okuda, "Accumulation and recovery of defects in ion-irradiated nanocrystalline gold", Journal of Nuclear Materials 297 (2001), 355-357.

[17] B. Radiguet, A. Etienne, P. Pareige, X. Sauvage, and R. Valiev, "Irradiation behavior of nanostructured 316 austenitic stainless steel", Journal of Materials Science **43** (2008), 7338-7343.

[18] W. Voegeli, K. Albe, and H. Hahn, "Simulation of grain growth in nanocrystalline nickel induced by ion irradiation", Nuclear Instruments and Methods in Physics Research Section B: Beam Interactions with Materials and Atoms **202** (2003), 230-235.

[19] D. Kaoumi, A. T. Motta, and R. C. Birtcher, "A thermal spike model of grain growth under irradiation", Journal of Applied Physics **104** (2008), 073525.

[20] H. A. Atwater, C. V. Thompson, and H. I. Smith, "Ion-bombardment-enhanced grain growth in germanium, silicon, and gold thin films", Journal of Applied Physics **64** (1988), 2337-2353.

[21] J. C. Liu, M. Nastasi, and J. W. Mayer, "Ion irradiation induced grain growth in Pd polycrystalline thin films", Journal of Applied Physics **62** (1987), 423-428.

[22] M. S. Chandrasekar and M. Pushpavanam, "Pulse and pulse reverse plating—Conceptual, advantages and applications", Electrochimica Acta **53** (2008), 3313-3322.

[23] D. B. Williams, C. B. Carter, Transmission Electron Microscopy, 2nd edition, Springer, 2009.

[24] J. F. Ziegler, J. P. Biersack, M. D. Ziegler, Calculation using the stopping and range of ions in matter (SRIM) code. <*http://www.srim.org/*>.

[25] R. C. Birtcher, M. A. Kirk, K. Furuya, G. R. Lumpkin and M-O. Ruault, "In situ Transmission Electron Microscopy Investigation of Radiation Effects", Journal of Materials Research 20 (2005), 1654-1683.

[26] J. P. Hirth, J. Lothe, Theory of Dislocations, 2nd edition, Krieger, Malabar, FL, 1992.

[27] D. A. Porter, K. E. Easterling, M. Y. Sherif, Phase transformations in metals and alloys, 3rd edition, Boca Raton, FL, 2009.

[28] S. M. Foiles, M. I. Baskes, and M. S. Daw, "Embedded-atom-method functions for the fcc metals Cu, Ag, Au, Ni, Pd, Pt, and their alloys", Physical Review B 33 (1986), 7983-7991.

[29] A. Hardouin Duparc, C. Moingeon, N. Smetniansky-de-Grande, and A. Barbu, "Microstructure modelling of ferritic alloys under high flux 1 MeV electron irradiations", Journal of Nuclear Materials 302 (2002), 143-155.

[30] E. Kuramoto, "Computer simulation of fundamental behaviors of interstitial clusters in Fe and Ni", Journal of Nuclear Materials 276 (2000), 143-153.

II. 6. *In situ* studies of irradiation induced twin boundary migration in nanotwinned silver (Scripta Materialia, 2013)

Twin boundaries (TBs) can enable unique mechanical and physical properties in metallic materials, thus twinning has been extensively studied in various face centered cubic (fcc) metals [1-3]. In fcc metals with $\sum3$ {111} coherent twin boundaries (CTBs) [1, 4], or $\sum3$ {112} incoherent twin boundaries (ITBs), twining typically occurs via the migration of 1/6 <112> Shockley partials [4]. Recent studies show that twinning can become an important alternative deformation mechanism other than dislocation slip in metals and alloys at cryogenic temperature or within nanograins [1, 2, 5, 6]. Deformation twinning in nanostructured metals has been extensively studied due to the fact that twinning becomes a more active deformation mechanism during plastic deformation [7, 8]. Deformation twins can form via emission of partials from grain boundary (GB) [9-11], splitting of GB [6, 9] and overlapping of stacking faults [12].

Besides deformation twins, high density growth twins have been observed in a variety of nanotwinned (nt) metallic materials, including Cu, Ag, Ni and its alloys, 330 stainless steel, and most recently Al [13-17]. Compared to their bulk counterparts, nt metals have shown high strength and ductility, superior electrical conductivity and high temperature thermal stability [7, 13, 15, 18]. In nt metals, CTBs and ITBs play critical roles on the mechanical strength and ductility. *In situ* nanoindentation studies showed ITBs and CTBs in nt Cu can migrate rapidly under stress and consequently detwinning (removal of TBs) occurs [19-21]. Atomistic simulations also explained the experimental observations of the migration of ITBs via a collective glide of Shockley partials in sets of three, one partial on each adjacent {111} glide planes [19, 22]. The migration speed of ITBs is related to stacking fault energy and the twin thickness [19, 20, 23]. The interaction of dislocations with CTB can lead to multiple steps (stacking faults) due to repetitive dissociation of stacking faults into perfect dislocations and mobile Shockley partials [21]. These steps can then act as sources for ITBs, and thus increase the mobility of TBs. These *in situ* studies strongly suggest that TBs can migrate under stress.

Recently we reported another salient character of TBs in nt metals. *In situ* Kr ion irradiation of nt Ag showed that TBs can actively interact with stacking fault tetrahedra (SFTs) and cause their collapse. Such interaction results in the formation of high density stacking faults adjacent to CTBs [24]. SFTs are notoriously stable defect clusters in fcc metals and their removal typically requires high temperature annealing, injection of interstitials or interaction with mobile dislocations [25]. Thus nt metals could become a new class of radiation tolerant materials.

GBs are considered as defect sinks in irradiated materials [26-28]. GBs can absorb irradiation induced self interstitial atoms (SIAs), vacancies and their clusters to alleviate radiation damage. As a special type of GB, TB may also act defect traps. King and Smith have studied the mechanism of point defect absorption by GBs and $\sum3$ {111} CTBs in electron irradiated Al and Cu, and showed that TBs may be biased sinks for dislocation loops [29]. It has also been shown that $\sum3$ {111} CTB obtains much smaller formation energy and greater binding energy for both interstitials and vacancies, as compared to $\sum3$ {112} ITB [30]. The findings are consistent to MD simulations on twinned Cu [31].

In this study, we report two important observations derived from *in situ* Kr ion irradiation of nt Ag. First, TBs in nt Ag migrate continuously and gradually during radiation in absence of stress. Second, dislocation loops frequently interact with CTBs and ITBs. We then connect the two events and explain the mechanisms of TB migration due to their interaction with radiation induced defects. We finish by pointing out the significance of TBs in absorbing defect loops and the potential impact of TB migration on continuous and effective removal of radiation induced defects in nt metals.

Epitaxial Ag films with thickness of ~ 2 μm were synthesized on single crystal Si (111) substrate by using DC magnetron sputtering technique at room temperature. Ag films were then annealed at 700 for 0.5 hours to achieve an average twin thickness of ~ 70 nm. Cross-sectional transmission electron microscopy (XTEM) specimens for *in situ* radiation study were prepared using grinding, polishing and ion mill techniques. Prior to and post irradiation, the specimen was investigated by an FEI Tecnai G2 F20 ST microscope. The specimen was irradiated with 1MeV Kr^{++}ions up to a maximum fluence of 2×10^{14} ions/m^2 (corresponding to a maximum of 1 dpa) at room temperature at the IVEM-TANDEM facility at Argonne National Laboratory where an ion accelerator is attached to a HITACHI H-9000NAR microscope. The microstructure of as-deposited twinned silver is revealed by Figure 6.1.
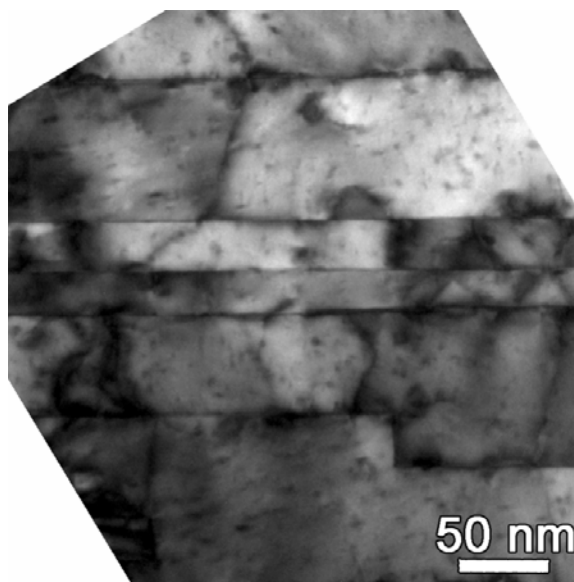

Figure 6.1 Cross-sectional transmission electron microscopy (XTEM) image of as-deposited nanotwinned Ag showing an average twin thickness of ~ 70 nm.
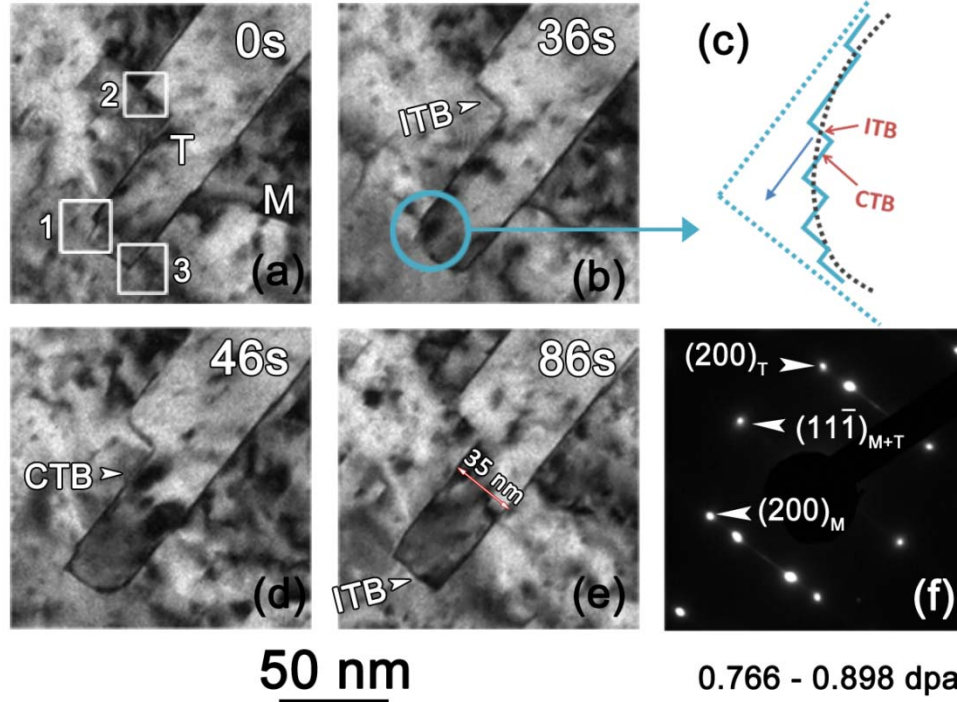
Figure 6.2 Continuous migration and recovery of twin boundaries (TBs). Snapshots recorded during *in situ* radiation in TEM and corresponding schematics showing the continuous evolution of twin boundaries over a dose range of 0.766 – 0.898 dpa. Observation was along [011] direction. (a) At 0s, box 1 showed a small kink at the junction of incoherent twin boundary (ITB) and coherent twin boundary (CTB), while box 2 and 3 each outlined a right angular corner that consisted of a pair of ITB and CTB. (b) By 36 s, sharp corners in box 2 and 3 became blunted, and the kink in box1 evolved into a curved boundary and (c) the corresponding magnified schematic for box 1 shows the curved corner consisted of numerous minuscule steps of ITBs and CTBs. (d) At 46s, the corner in box 1 became sharp again, while the bottom corner in box 3appeared more blunted (with mixtures of ITBs and CTBs steps). (e) The kink in box 1 nearly disappeared eventually by 86s. (f) Selected area diffraction (SAD) pattern indicating the existence of twins with $\Sigma 3$ {111} CTBs..

The variation of TBs is shown by a set of *in situ* video clips taken at a dose varying from 0.766 to 0.898 displacement-per-atom (dpa) in Figure 6.2. There were three major locations where TBs evolved during radiation, as outlined by three boxes. At 0s,

box 1 showed a small kink at the junction of an ITB and CTB, while box 2 and 3 each showed a corner that consisted of a pair of straight and orthogonal ITB and CTB (Figure 6.2a). By 36 s, the sharp corners in box 2 and 3 also became blunted, and the kink in box 1 evolved into a curved boundary (Figure 6.2b). The corresponding schematic for box 1 illustrates the curved corner consisting of numerous minuscule steps of ITBs and CTBs (Figure 6.2c). At 46s, the corner in box 1 became orthogonal again, while the bottom corner in box 3 appeared more obtuse (with mixtures of ITBs and CTBs steps) (Figure 6.2d). The kink in box 1 nearly disappeared by 86s (Figure 6.2e) and eventually evolved into an abrupt right angle at 1 dpa (see Figure 6.3 and 6.4 for visual guide).

The selected area diffraction (SAD) pattern in Figure 6.2f shows two sets of SAD pattern of twin and matrix, as well as the ∑3 {111} CTBs orientation. Also, the streaking lines in the SAD indicate the formation of stacking faults during radiation. The morphology of irradiation induced stacking faults and defect clusters can be found in our previous study [24].
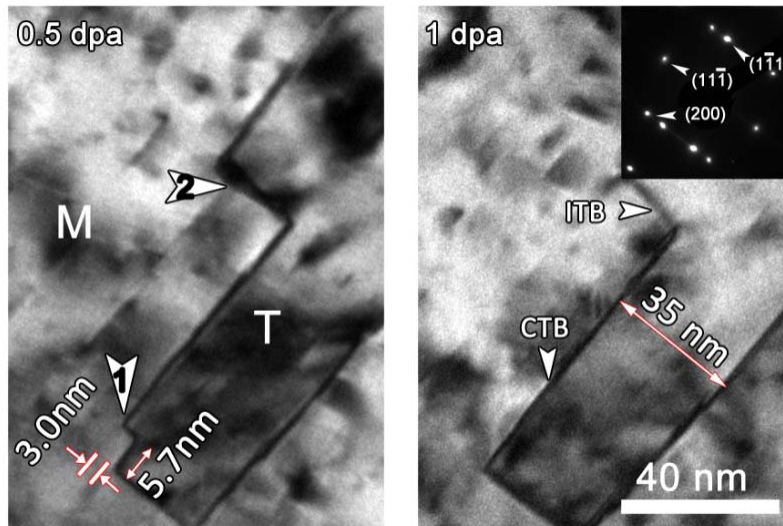
Figure 6.3 Removal of a fine ITB (forward migration). XTEM image of irradiated nanotwinned Ag at 0.5 displacement-per-atom (dpa) and 1 dpa. Twin and matrix are as labeled. The area of interest contained a kink consisting of a 3 nm thick incoherent twin boundary (ITB) and 5.7 nm wide coherent twin boundary (CTB) at 0.5 dpa, as indicated by arrow 1. This kink disappeared at 1 dpa. Arrow 2 indicates a greater ITB which were slightly inclined at the dose span from 0.5 dpa to 1 dpa, showing no evident migration.

Figure 6.4 Visual guide of the *in situ* snapshots showing the evolution of twin boundaries.
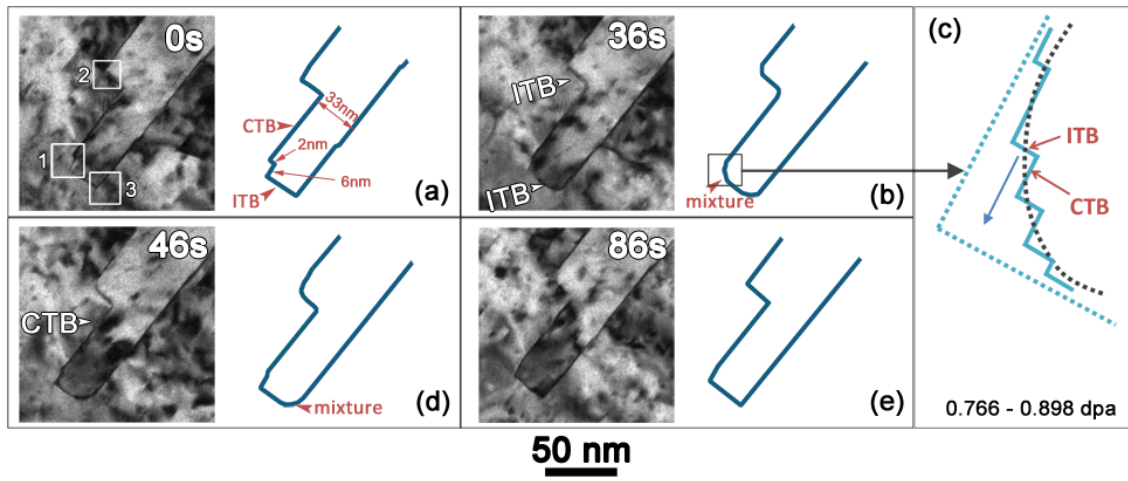
Most twinning or detwinning process takes place under stress via migration of Shockley partials. A few events may occur during twinning, including partial emission, rapid migration of leading partials, pinning by faulted loops, dislocation interactions, and atomic shuffling [1]. This is in large contrast to radiation induced twin boundary migration as little stress is introduced during radiation. Instead a large amount of defects can be generated during Kr radiation, including SIAs, vacancies, dumbbells, crowdions, voids, dislocations, perfect and faulted loops [25, 32]. In fcc metals, loops are more commonly observed and their formation and mobility have been widely studied [33, 34]. This leads us to hypothesize that the mechanism of twin boundary migration could be related to interaction between radiation induced defects and TBs.

To understand TB migration mechanisms, it is necessary to examine defect-TB interactions. As shown in Figure 6.5a, a dislocation loop A was a few nm away from the CTB at 0 s.　By 1 s, the loop (A') migrated rapidly and contacted the CTB (Figure 6.5b). The same loop was then instantly absorbed by the CTB in 0.1s and its migration path was indicated by the arrow in Figure 6.5c. In fcc metals, small defect clusters include dumbbells and crowdions, and larger stable defect clusters are either perfect dislocation loops ($1/2 <110> \{110\}$) or faulted loops ($1/3 <111> \{111\}$) [35]. Perfect loops are considered glissile while the faulted loops are sessile [25, 35]. The mobile defect cluster in Figure 6.5a is likely to be a perfect dislocation loop by examining its crystallographic

orientation. As shown in Figure 6.5d, the projection plane (the observation plane) was (011) and the TB was (11$\bar{1}$) plane. Another (110) was shown to be 60° inclined to the (011) projection plane. The perfect loop slipped along the (011) plane towards TB, as indicated in Figure 6.5d. Experiments and simulations have shown that perfect loops can migrate quickly along one dimension under radiation [35-37]. Thus the perfect loop in this case may perform one dimensional migration towards the TB and its path was projected on the (011) plane.
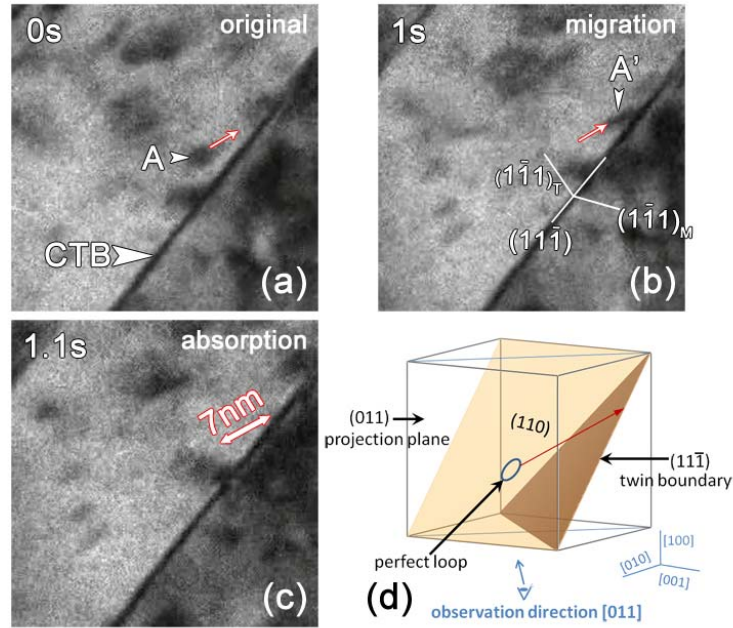
Figure 6.5. *In situ* snapshots showing migration and absorption of defect clusters by a CTB at the dose of ~ 0.82 dpa. (a) Loop A was away from the CTB at 0 s and (b) it migrated toward the CTB at 1s, as indicated by A'. (c) The loop was absorbed by the CTB by 1.1 s. The arrow shows the path of loop migration (by about 7 nm) before being absorbed by the CTB. (d) Schematics of fcc structure and miller indices revealing that the possible orientation and migration direction of the dislocation loop in the snapshots. This dislocation loop may be a perfect glissile loop on (110) plane (projected on the (011) plane of TEM foil), with a Burgers vector of 1/2<110>. The cylinder indicates the glissile trajectory of migration of the loop towards the (11$\bar{1}$) CTB.
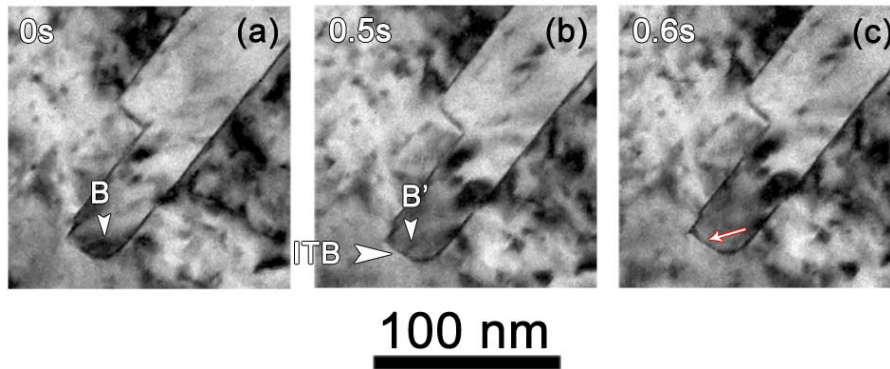
Figure 6.6. *In situ* snapshots showing migration and absorption of defect clusters by an ITB at the dose of ~ 0.85 dpa. (a) A dislocation loop B interacted with the ITB. (b) The loop rearranged itself to B' at 0.5s and (c) was absorbed by 0.6s. The migration path is indicated by an arrow.

There were certainly other types of dislocation loop – TB interactions, one of them being the interaction between loops and ITBs. A dislocation loop, B, was observed in Figure 6.6a in close proximity to an obtuse corner in the twin. The loop rearranged itself to B' at 0.5s (Figure 6.6b) and was then absorbed by adjacent ITB at 0.6s. The migration path is indicated by an arrow.

Li *et al.* examined the migration of vicinal ITBs in self-ion irradiated Cu, and ascribed the ITB migration to collective glide of an array of mobile partials [38]. The driving force for migration is the reduction of potential energy via recombination of vacancies and interstitials. However *in situ* study on radiation induced TB migration is rare. Next we propose several mechanisms of TB migration based on *in situ* radiation studies on nt Ag.
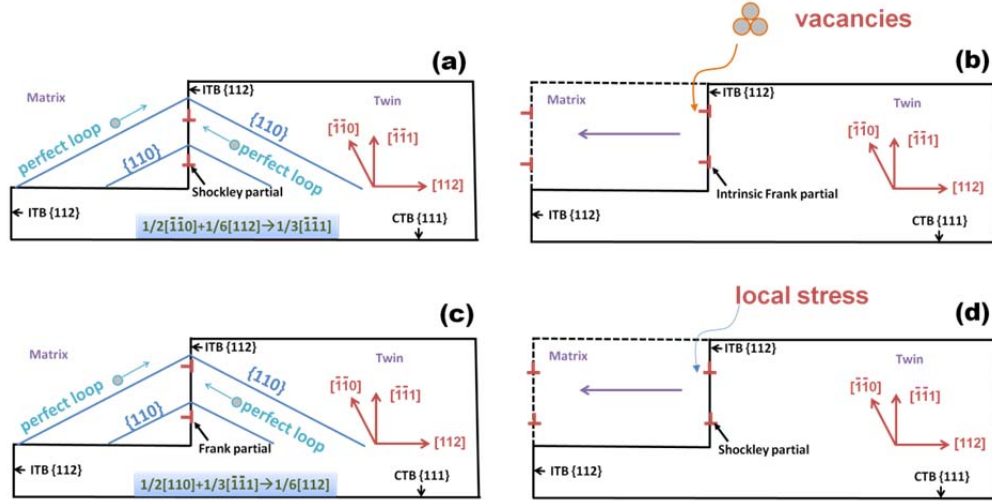
Figure 6.7. Schematics of ITB migration mechanisms during radiation. (a) Schematics illustrates the interaction of dislocation loop on {110} plane with Shockley partials on ITB, leading to the formation of Frank partials at an ITB. (b) The ITB is decorated by an array of 1/3<111> intrinsic Frank partials (due to perfect loop-Shockley partial interactions). The absorption of vacancies can result in the ITB moving leftwards via dislocation climb. (c) The Frank partials can interact with perfect loops again and form mobile Shockley partials which usually dominate the migration of the ITB. (d) Shockley partials can migrate under local stress induced by irradiation.

We will begin by examining the effects of defect-TB interactions on ITB migration. The ideal ITBs typically consist of an array of mobile Shockley partials [19]. A perfect dislocation loop can migrate on one of the {110} planes before it encounters the Shockley partials at the ITB {112}, as shown in Figure 6.7a. Such orientation relationship is inherited from the TEM observations in Figure 6.5. If this perfect dislocation loop is absorbed by an ITB (as shown previously), their interaction may lead to the formation of a Frank partial by

$$\frac{1}{2}[\bar{1}\bar{1}0] + \frac{1}{6}[112] \longrightarrow \frac{1}{3}[\bar{1}\bar{1}1] \tag{1}$$

Thus the ITB may be decorated by an array of Frank partials as a result of frequent interaction with perfect loops as shown in Figure 6.7b. Previous study has also shown that CTBs are possible sinks for SIAs and vacancies [29]. Additionally SFTs may interact

with CTBs and collapse into Frank partials [24, 31]. Thus a large amount of Frank partials formed during radiation may exist along ITBs. Others have also shown that ITB could consist of an array of Frank loops [39].

If Frank partials along ITBs were intrinsic in nature (vacancy loops), they might expand by absorbing vacancies, causing the ITB to migrate leftwards as shown in Figure 6.7b. In comparison the intrinsic Frank partials might shrink by absorbing SIAs and hence ITB can propagate rightwards. Thus during radiation it is likely the ITB could migrate back and forth via dislocation climb by absorbing SIAs or vacancies. These interactions may explain the evolution of straight vs. curved ITB corners in Figure 6.2.

Second, ITBs can migrate through stress driven glide of mobile Shockley partials. It is typical that partial dislocations 1/6<112> are distributed at the ITB. These partials might migrate under local stress induced by defect clusters in contrast to slip of partials under applied stress [1, 3, 20, 21]. Forgoing studies have shown that mobile Shockley partials at ITB may interact with perfect dislocation loop and form sessile Frank partials. If these Frank partials then absorb perfect loops with opposite Burgers vector, then a mobile Shockley partial may recover through the following reaction:

$$\frac{1}{2}[110] + \frac{1}{3}[\bar{1}\bar{1}1] \longrightarrow \frac{1}{6}[112] \tag{2}$$

The interaction process is illustrated in Figure 6.7c. These partials could then glide on (11$\bar{1}$) plane under local stress (arising from interactions with neighboring dislocation loops), resulting in ITB migration as shown in Figure 6.7d. Due to active dislocation-defect interactions under *in situ* irradiation, the two TB migration mechanisms, glide of Shockley partials and climb of Frank partials, may operate alternatively or simultaneously to effectively advance or retreat ITBs.

It should be noted that if a dislocation loop is absorbed by free surface, the stress field of the dislocation loop is completely removed and thus the net Burgers vector of the loop becomes zero. In this study, the interaction of a dislocation loop with an ITB leads to a residual partial dislocation with non-zero Burgers vector, although the majority (stress field) of the dislocation loop has been eliminated during interaction. The net Burgers vector of the three dislocations is zero. The forgoing discussion on the two loop-ITB interaction mechanisms (described in eq. (1) and (2)) also implies dual-directionality on

migration of the ITBs. That is the interactions of loop with ITB can lead to either forward (removal of fine ITB step) or backward migration (creation of additional fine ITB steps) of ITBs during *in situ* study. Indeed both forward and backward migrations of ITBs have been observed as shown in Figure 6.3 (forward) and box 3 (backward) in Figure 6.2 a and d.

In situ nanoindentation also reveals that the morphological evolution of TBs (from orthogonal to curved geometry) could be reversible. Such resilient and highly mobile TBs could be important defect sinks that restore structural integrity of irradiated metallic materials. Thus it may be beneficial to design nanotwinned metallic materials with mobile TBs to achieve significantly improved radiation tolerance compared to their conventional coarse grained counterparts.

Frequent migration of TBs was observed in nanotwinned Ag film subjected to in situ Kr ion irradiation up to 1 dpa. Radiation induced defects were frequently absorbed by TBs. The climb of Frank partials and glide of mobile Shockley partials (at ITBs) were responsible for the migration of twin boundaries. Both mechanisms were associated with dislocation loop-TB interactions and defect absorptions. TBs may have superior sink capacity because their migration direction is reversible depending on the absorption of interstitials or vacancies. Introduction of mobile TBs can be an important approach to drastically enhance radiation tolerance of metallic materials.

Reference

[1] M. Niewczas, Dislocations in Solids, 13 (2007) 263-364.

[2] H. Van Swygenhoven, P.M. Derlet, A.G. Froseth, Nat Mater, 3 (2004) 399-403.

[3] J. Venables, Philosophical Magazine, 6 (1961) 379-396.

[4] J.P. Hirth, J. Lothe, John Wiley and Sons, Inc., 1982, (1982) 857.

[5] M.A. Meyers, O. Vöhringer, V.A. Lubarda, Acta Materialia, 49 (2001) 4025-4039.

[6] V. Yamakov, D. Wolf, S. Phillpot, H. Gleiter, Acta Materialia, 50 (2002) 5005-5020.

[7] K. Lu, L. Lu, S. Suresh, Science, 324 (2009) 349-352.

[8] S. Ogata, J. Li, S. Yip, Physical Review B, 71 (2005) 224102.

[9] X. Wu, X. Liao, S. Srinivasan, F. Zhou, E. Lavernia, R. Valiev, Y. Zhu, Physical review letters, 100 (2008) 95701.

[10] X. Liao, Y. Zhao, Y. Zhu, R. Valiev, D. Gunderov, Journal of applied physics, 96 (2004) 636-640.

[11] X. Liao, F. Zhou, E. Lavernia, D. He, Y. Zhu, Applied Physics Letters, 83 (2003) 5062-5064.

[12] V. Yamakov, D. Wolf, S. Phillpot, A. Mukherjee, H. Gleiter, Nature Materials, 3 (2003) 43-47.

[13] O. Anderoglu, A. Misra, H. Wang, F. Ronning, M.F. Hundley, X. Zhang, Applied Physics Letters, 93 (2008) 083108-083103.

[14] D. Bufford, H. Wang, X. Zhang, Acta Materialia, 59 (2011) 93-101.

[15] Y. Liu, D. Bufford, H. Wang, C. Sun, X. Zhang, Acta Materialia, 59 (2011) 1924-1933.

[16] X. Zhang, A. Misra, H. Wang, T. Shen, M. Nastasi, T. Mitchell, J. Hirth, R. Hoagland, J. Embury, Acta Materialia, 52 (2004) 995-1002.

[17] D. Bufford, Z. Bi, Q.X. Jia, H. Wang, X. Zhang, Applied Physics Letters, 101 (2012) 223112-223115.

[18] L. Lu, Y. Shen, X. Chen, L. Qian, K. Lu, Science, 304 (2004) 422-426.

[19] J. Wang, N. Li, O. Anderoglu, X. Zhang, A. Misra, J.Y. Huang, J.P. Hirth, Acta Materialia, 58 (2010) 2262-2270.

[20] N. Li, J. Wang, J. Huang, A. Misra, X. Zhang, Scripta Materialia, 64 (2011) 149-152.

[21] N. Li, J. Wang, A. Misra, X. Zhang, J.Y. Huang, J.P. Hirth, Acta Materialia, 59 (2011) 5989-5996.

[22] J. Wang, O. Anderoglu, J.P. Hirth, A. Misra, X. Zhang, Applied Physics Letters, 95 (2009) 021908-021903.

[23] J. Wang, A. Misra, J.P. Hirth, Physical Review B, 83 (2011) 064106.

[24] K.Y. Yu, D. Bufford, C. Sun, Y. Liu, H. Wang, M.A. Kirk, M. Li, X. Zhang, Nat Commun, 4 (2013) 1377.

[25] G.S. Was, Fundamentals of radiation materials science: metals and alloys, Springer, 2007.

[26] B.N. Singh, M. Eldrup, S.J. Zinkle, S.I. Golubov, Philosophical Magazine A, 82 (2002) 1137-1158.

[27] X.-M. Bai, A.F. Voter, R.G. Hoagland, M. Nastasi, B.P. Uberuaga, Science, 327

(2010) 1631-1634.

[28] B.N. Singh, Philosophical Magazine, 29 (1974) 25 - 42.

[29] A.H. King, D.A. Smith, Philosophical Magazine A, 42 (1980) 495-512.

[30] M.A. Tschopp, K. Solanki, F. Gao, X. Sun, M.A. Khaleel, M. Horstemeyer, Physical Review B, 85 (2012) 064108.

[31] M. Niewczas, R.G. Hoagland, Philosophical Magazine, 89 (2009) 727-746.

[32] G. Ackland, Science, 327 (2010) 1587-1588.

[33] Y.N. Osetsky, D.J. Bacon, A. Serra, B.N. Singh, S.I. Golubov, Journal of Nuclear Materials, 276 (2000) 65-77.

[34] D.J. Bacon, Y.N. Osetsky, R. Stoller, R.E. Voskoboinikov, Journal of Nuclear Materials, 323 (2003) 152-162.

[35] Y. Matsukawa, S.J. Zinkle, Science, 318 (2007) 959-962.

[36] K. Arakawa, K. Ono, M. Isshiki, K. Mimura, M. Uchikoshi, H. Mori, Science, 318 (2007) 956-959.

[37] Y. Satoh, H. Matsui, Philosophical Magazine, 89 (2009) 1489-1504.

[38] N. Li, J. Wang, Y.Q. Wang, Y. Serruys, M. Nastasi, A. Misra, Journal of applied physics, 113 (2013) 023508-023508.

[39] E.A. Marquis, D.L. Medlin, F. Léonard, Acta Materialia, 55 (2007) 5917-5923.

III. Administrative actions

The project has sponsored the following personnel.

Name	Title	% supported
Xinghang Zhang	PI, Associate professor	One summer month
Kaiyuan Yu	Graduate student (started in fall 2009, graduated in spring 2013)	FTE
Youxing Chen	Graduate student (started in fall 2010, to graduate in fall 2014)	FTE
Cheng Sun	Graduate student (started in fall 2009, graduated in spring 2013, now a postdoctor at Los Alamos National Laboratory)	Partially supported

IV. Near term plans

We plan to perform the following tasks in the last year of the project.

1) Publish papers on radiation damage in Cu/Fe multilayers.

2) We will investigate radiation tolerance of Cu/Co multilayers. (111) Cu/Co has fcc/hcp type of interfaces, whereas (100) Cu/Co has fcc/fcc type of interfaces. We will investigate the influence of different types of interfaces and size effect on radiation tolerance of multilayers.

3) We will start to look into Cu/Ag/Co and Cu/Ag/Mo triphase thin films. These systems will be tailored to acquire large volume fraction of triple junctions, which are usually considered to be effective defect sinks.

Strengthening mechanisms of Ag/Ni immiscible multilayers with fcc/fcc interface

Q1 K.Y. Yu [a,b], Y. Liu [a,b], S. Rios [a,b], H. Wang [a,c], X. Zhang [a,b],*

[a] Department of Materials Science and Engineering, Texas A&M University, College Station, TX 77843, United States
[b] Department of Mechanical Engineering, Texas A&M University, College Station, TX 77843, United States
[c] Department of Electrical and Computer Engineering, Texas A&M University, College Station, TX 77843, United States

ARTICLE INFO

ABSTRACT

We investigate the microstructure and mechanical properties of sputtered face-centered cubic (fcc) Ag/Ni multilayers with varying individual layer thickness h of 1–200 nm deposited on Si (100) and Si (111) substrates. Both multilayer systems have similar <111> fiber texture with predominantly incoherent Ag/Ni interfaces. Superlattice structure arises when h decreases to less than 5 nm. Indentation hardness of both Ag/Ni systems shows similar significant size dependence when h > 3 nm. Strengthening mechanisms in Ag/Ni systems are discussed and compared to those in Cu/Ni and Ag/Cu systems with fcc/fcc interfaces.

© 2013 Published by Elsevier B.V.

1. Introduction

Nanoscale metallic multilayers have attracted increasing attention due to their high mechanical strength and impressive radiation resistance [1–9]. Multilayers, with periodically repeated constituents, exhibit strong size dependent variation in mechanical strength. Indentation hardness of multilayers increases significantly as individual layer thickness h decreases and may reach 1/2–1/3 of theoretical strength when h is a few nanometers [2,3,10–13]. Numerous strengthening mechanisms have been proposed to describe film thickness dependent variation of hardness. When h is greater than 50 nm, mechanical behavior typically follows the Hall – Petch relationship where strengthening is due to dislocation pile-ups at layer interfaces [8,14–16]. When 50 nm > h > 10 nm, dislocation movement is confined within layers via Orowan bowing, and strengthening mechanism can be described by the confined layer slip (CLS) model [3,11]. Recently, a refined CLS model has been developed by taking interface stresses and dislocation interactions into account and the refined model describes the layer thickness dependent variation of hardness in Cu/Nb very well [11]. When h reduces to several nanometers (typically 1 ~ 5 nm), strength of multilayers is typically independent of h as strength originates from the barrier resistance of interface to penetration of dislocations. Strengthening mechanisms become more complex, and usually involve multiple factors such as Koehler stress [17], misfit dislocations [18], coherency stress [18,19] and twinning [20]. Koehler stress arises when layer constituents have significantly different elastic modulus, resulting in a repulsive imaging force for dislocation to slip from soft to hard layer constituent. Misfit

dislocations at layer interfaces may interact with gliding dislocations and cause extra resistance to their propagation [21]. Meanwhile, coherency stress operates in coherent or semi-coherent systems, where a small lattice mismatch exists between layer constituents. Coherency stress does not necessarily add significantly to peak strength. But as coherency stress alternates from tension to compression from one layer to the other, it interferes with the propagation of dislocations within the layers [19]. For incoherent systems, a hardness plateau (saturation at maxima) is typically observed at smaller h [22,23]. While for coherent systems, such as Cu/Ni, softening occurs due to the fact that fully coherent interfaces [18,20], sometimes referred to as transparent interfaces, have little resistance to the transmission of dislocations. In addition, intermixing along interface is also likely to contribute to softening [2].

Abundant studies have focused on microstructure and mechanical properties of multilayers with various types of interfaces. In several fcc/bcc systems, such as Cu/Nb [1,2,10], Cu/Fe [24], Cu/V [5], Al/Nb [6] and Ag/V [25], most of the layer constituents are immiscible except Al/Nb. Strengthening in these systems with primarily Kurdjumov-Sachs (K-S) orientation relationship arises from slip discontinuity across opaque interface. Molecular dynamics (MD) simulations have shown that Cu/Nb system has a weak interface (has lower elastic modulus than layer constituents) and thus dislocations are attracted to the weak interface and lose their singularity, making reemission of dislocations a very difficult process [19]. Hence the weak Cu/Nb interfaces lead to high strength nanolayer composite. In the Cu/Fe system, Chen et. al observed high strength in multilayers with relative large h, ~ 100 nm, and ascribed the high strength to confined dislocation slip within narrow Fe columns [24]. In fully coherent Cu/Fe 0.75 nm multilayers, high density growth twins with an average twin spacing of ~ 6 nm has been observed and these nanotwins play an important role on retention of high hardness in fully coherent fcc Cu/Fe 0.75 nm multilayer.

* Corresponding author at: Department of Materials Science and Engineering, Texas A&M University, College Station, TX 77843, United States. Tel.: +1 979 845 2143.
E-mail address: zhangx@tamu.edu (X. Zhang).

Removal of stacking-fault tetrahedra by twin boundaries in nanotwinned metals

K.Y. Yu[1], D. Bufford[1], C. Sun[1], Y. Liu[1], H. Wang[2], M.A. Kirk[3], M. Li[4] & X. Zhang[1]

Stacking-fault tetrahedra are detrimental defects in neutron- or proton-irradiated structural metals with face-centered cubic structures. Their removal is very challenging and typically requires annealing at very high temperatures, incorporation of interstitials or interaction with mobile dislocations. Here we present an alternative solution to remove stacking-fault tetrahedra discovered during room temperature, *in situ* Kr ion irradiation of epitaxial nanotwinned Ag with an average twin spacing of ∼8 nm. A large number of stacking-fault tetrahedra were removed during their interactions with abundant coherent twin boundaries. Consequently the density of stacking-fault tetrahedra in irradiated nanotwinned Ag was much lower than that in its bulk counterpart. Two fundamental interaction mechanisms were identified, and compared with predictions by molecular dynamics simulations. *In situ* studies also revealed a new phenomenon: radiation-induced frequent migration of coherent and incoherent twin boundaries. Potential migration mechanisms are discussed.

[1] Department of Mechanical Engineering, Materials Science and Engineering Program, Texas A&M University, College Station, Texas 77843-3123, USA. [2] Department of Electrical and Computer Engineering, Texas A&M University, College Station, Texas 77843-3128, USA. [3] Materials Science Division, Argonne National Laboratory, Argonne, Illinois 60439, USA. [4] Nuclear Engineering Division, Argonne National Laboratory, Argonne, Illinois 60439, USA. Correspondence and requests for materials should be addressed to X.Z. (email: zhangx@tamu.edu).

In situ Evidence of Defect Cluster Absorption by Grain Boundaries in Kr Ion Irradiated Nanocrystalline Ni

C. SUN, M. SONG, K.Y. YU, Y. CHEN, M. KIRK, M. LI, H. WANG, and X. ZHANG

Significant microstructural damage, in the form of defect clusters, typically occurs in metals subjected to heavy ion irradiation. High angle grain boundaries (GBs) have long been postulated as sinks for defect clusters, like dislocation loops. Here, we provide direct evidence, *via in situ* Kr ion irradiation within a transmission electron microscope, that high angle GBs in nanocrystalline (NC) Ni, with an average grain size of ~55 nm, can effectively absorb irradiation-induced dislocation loops and segments. These high angle GBs significantly reduce the density and size of irradiation-induced defect clusters in NC Ni compared to their bulk counterparts, and thus NC Ni achieves significant enhancement of irradiation tolerance.

I. INTRODUCTION

RADIATION of metals by high energy particles generates vacancy-interstitial pairs (Frenkel pairs). These point defects can be removed through mutual recombination or a reaction with defect sinks, such as neutral sinks (grain boundaries (GBs), voids), biased sinks (dislocations), and variable sinks (impurity atoms and coherent precipitates).[1] Meanwhile, these point defects can aggregate to form defect clusters, which can be dislocation loops, voids, or stacking fault tetrahedron.[2] High densities of radiation-induced defects can result in significant degradation of mechanical stability of structural metallic materials. The enhancement of radiation tolerance of metallic materials *via* mitigation of the formation of defect clusters is a challenge. The chemistry and microstructures of the materials play an important role on the nucleation and migration of defect clusters. For instance, austenitic stainless steels subjected to cold working or modified with the addition of certain elements showed reduced swelling under neutron radiation at 673 K (400 °C).[3] Oxide dispersion-strengthened ferritic alloys showed enhanced resistance to void swelling and fracture embrittlement under Helium radiation and electron irradiation.[4–6] Layer interfaces in immiscible multilayers such as Cu/Nb,[7,8]

Cu/Mo,[9] Cu/V,[10] and V/Ag[11] can effectively mitigate swelling, lattice distortion, and radiation hardening.

GBs are considered as sinks for irradiation-induced defects.[12–16] A substantial reduction of radiation damage is anticipated in nanocrystalline (NC) materials, given their larger volume fraction of GBs, compared to the conventional coarse-grained (CG) materials. Several molecular dynamic simulations have been reported on the impact of GBs on the radiation behavior of NC metals. Samaras *et al.* observed significant atomic migration toward the surrounding GB during thermal spikes in self-ion irradiated NC Ni.[17] Bai *et al.* showed that GBs act as defect sinks as well as sources, and they emit interstitials to annihilate the nearby vacancies within the grains.[18] Experimental studies also showed that irradiation-induced damage was significantly reduced in NC metals. Singh *et al.* found that grain refinement can delay the nucleation of voids and mitigate void swelling in stainless steel with a grain size from 0.45 to 50 μm during electron irradiation.[19] Rose *et al.* reported that the defect cluster density in Kr ion irradiated NC Pd and ZrO_2 was dramatically reduced by reducing the grain size to below 50 nm, and no defect clusters were detected in NC Pd (<30 nm) and ZrO_2 (<15 nm) grains.[14] NC $MgGa_2O_4$ and TiNi revealed enhanced amorphization resistance subjected to 300 keV Kr^{++} ions and 1.5 MeV Ar^+ ions, respectively.[20,21] Chimi *et al.* reported that the defect accumulation rate in NC Au is lower than that in polycrystalline Au subjected to ^{12}C ion irradiation at 300 K (27 °C).[22] Radiguet *et al.* performed Fe ion irradiation on NC 316 stainless steel with a grain size of 40 nm at 623 K (350 °C) and no intragranular precipitates were observed.[23]

Grain growth of NC metals under irradiation has been reported. For example, Voegeli *et al.* performed MD simulations on NC Ni with a grain size of 5 and 10 nm and indicated that grain growth occurs when the thermal spike volume is larger than the grain volume.[24] Kaoumi *et al.* reported grain growth of NC Au, Pt, Cu,

C. SUN, M. SONG, K.Y. YU, Y. CHEN, Ph.D. Students, and X. ZHANG, Associate Professor, are with Department of Mechanical Engineering, Materials Science and Engineering Program, Texas A&M University, College Station, TX 77843-3123. Contact e-mail: zhangx@tamu.edu M. KIRK, Materials Scientist, is with the Materials Science Division, Argonne National Laboratory, Argonne, IL 60439. M. LI, Materials Researcher, is with the Nuclear Engineering Division, Argonne National Laboratory, Argonne, IL 60439. H. WANG, Associate Professor, is with Department of Electrical and Computer Engineering, Texas A&M University.
Manuscript submitted April 9, 2012.
Article published online February 12, 2013

In situ studies of irradiation-induced twin boundary migration in nanotwinned Ag

K.Y. Yu,[a,b] D. Bufford,[a,b] F. Khatkhatay,[c] H. Wang,[c] M.A. Kirk[d] and X. Zhang[a,b,*]

[a]*Department of Mechanical Engineering, Texas A&M University, College Station, TX 77843-3123, USA*
[b]*Department of Materials Science and Engineering, Texas A&M University, College Station, TX 77843-3123, USA*
[c]*Department of Electrical and Computer Engineering, Texas A&M University, College Station, TX 77843-3128, USA*
[d]*Materials Science Division, Argonne National Laboratory, Argonne, IL 60439, USA*

Twin boundary migration is usually observed during annealing or plastic deformation. We report on *in situ* observation of Kr ion irradiation-induced microstructure evolution in epitaxial nanotwinned Ag films with an average twin thickness of 70 nm. Kr ion irradiation-induced defect clusters are absorbed by coherent and incoherent twin boundaries. Frequent interactions between defect clusters and twin boundaries lead to continuous migration of twin boundaries. The potential mechanisms of twin boundary migration are discussed.
Published by Elsevier Ltd. on behalf of Acta Materialia Inc.

Twin boundaries (TBs) can enable unique mechanical and physical properties in metallic materials, thus twinning has been extensively studied in various face-centered cubic (fcc) metals [1–3]. In fcc metals with $\sum 3$ {1 1 1} coherent twin boundaries (CTBs) [1,4] or $\sum 3$ {1 1 2} incoherent twin boundaries (ITBs), twining typically occurs via the migration of 1/6<1 1 2> Shockley partials [4]. Recent studies show that twinning can become an important alternative deformation mechanism to dislocation slip in metals and alloys at cryogenic temperature or within nanograins [1,2,5,6]. Deformation twinning in nanostructured metals has been extensively studied because twinning becomes a more active deformation mechanism during plastic deformation [7,8]. Deformation twins can form via emission of partials from grain boundaries (GBs) [9–11], splitting of GBs [6,9] and overlapping of stacking faults [12].

Besides deformation twins, high-density growth twins have been observed in a variety of nanotwinned (nt) metallic materials, including Cu, Ag, Ni and its alloys, 330 stainless steel and, most recently, Al [13–17]. Compared to their bulk counterparts, nt metals have shown high strength and ductility, superior electrical conductivity and high-temperature thermal stability [7,13,15,18]. In nt metals, CTBs and ITBs play critical roles on mechanical strength and ductility. *In situ* nanoindentation studies have shown that ITBs and CTBs in nt Cu can migrate rapidly under stress and consequently detwinning (removal of TBs) occurs [19–21]. Atomistic simulations have also explained the experimental observations of the migration of ITBs via a collective glide of Shockley partials in sets of three – one partial on each adjacent {1 1 1} glide plane [19,22]. The migration speed of ITBs is related to the stacking fault energy and twin thickness [19,20,23]. The interaction of dislocations with CTBs can lead to multiple steps (stacking faults) due to repetitive dissociation of stacking faults into perfect dislocations and mobile Shockley partials [21]. These steps can then act as sources for ITBs, and thus increase the mobility of TBs. These *in situ* studies strongly suggest that TBs can migrate under stress.

Recently we reported another salient character of TBs in nt metals. *In situ* Kr ion irradiation of nt Ag showed that TBs can actively interact with stacking fault tetrahedra (SFTs) and cause their collapse. Such interaction results in the formation of high-density stacking faults adjacent to CTBs [24]. SFTs are notoriously stable defect clusters in fcc metals and their removal typically requires high-temperature annealing, injection of interstitials or interaction with mobile dislocations [25]. Thus nt metals could become a new class of radiation-tolerant materials.

GBs are considered as defect sinks in irradiated materials [26–28]. They can absorb irradiation-induced self-interstitial

* Corresponding author. Tel.: +1 979 845 2143; e-mail addresses: zhangx@tamu.edu; xinghangz@yahoo.com

CrossMark

Comparisons of radiation damage in He ion and proton irradiated immiscible Ag/Ni nanolayers

K.Y. Yu [a], Y. Liu [a], E.G. Fu [b], Y.Q. Wang [c], M.T. Myers [d], H. Wang [e], L. Shao [d], X. Zhang [a,*]

[a] Department of Mechanical Engineering, Department of Materials Science and Engineering, Texas A&M University, College Station, TX 77843-3123, United States
[b] State Key Laboratory of Nuclear Physics and Technology, School of Physics, Peking University, Beijing 100871, PR China
[c] Materials Science and Technology Division, Los Alamos National Laboratory, Los Alamos NM87545, United States
[d] Department of Nuclear Engineering, Texas A&M University, College Station, TX 77843-3133, United States
[e] Department of Electrical and Computer Engineering, Texas A&M University, College Station, TX 77843-3128, United States

A B S T R A C T

We compare the evolution of microstructure and mechanical properties of Ag/Ni multilayers of varying layer thickness (1–200 nm) subjected to helium ion and proton irradiation at room temperature to similar dose, ~2 displacements-per-atom on average. Layer structure remained intact after both types of irradiation although defects accumulated in the layers are different. Helium bubbles were the major defects in helium ion irradiated films, while dislocation loops were ubiquitous in proton irradiated multilayers. In He ion irradiated multilayers, radiation hardening was greater than that in proton irradiated specimens, and the magnitude of hardening decreased with decreasing individual layer thickness. In comparison no size dependent hardening was observed in proton irradiated films. Mechanisms of irradiation induced hardening were discussed.

Published by Elsevier B.V.

1. Introduction

In irradiated metallic materials, high-energy light particles, such as electrons, initially create equal number of interstitials and vacancies, and later evolve into defect clusters because biased defect sinks, such as dislocations, can trap one type of the defects preferentially and leave the other type supersaturated. Consequently the evolution of defect density with radiation fluence is typically described by the sink bias model [1]. When incident particles are heavy ions or neutrons, radiation induced damage is predominantly cascades and sub-cascades where vacancies and interstitials are spatially segregated instantaneously, and this phenomenon is described by production bias model [1]. Both cases result in a substantial quantity of defect clusters. Defect clusters lead to void swelling and radiation hardening, which are often accompanied by embrittlement [2–4]. Therefore it is of great significance to design materials with improved radiation tolerance via in situ removal of those defect clusters during radiation. Next generation nuclear reactors require structural materials and coatings with superior radiation tolerance, that is to sustain more than hundreds of displacements-per-atom (dpa) over 80 years [4]. To reach such an ambitious goal, design of materials with a large amount of internal defect sinks, such as dislocations, grain boundaries (GBs) and phase boundaries, is necessary [5]. These sinks must have the ability to annihilate radiation induced defects and their clusters, and consequently suppress radiation hardening and embrittlement

[2]. Meanwhile these defect sinks must be stable themselves against radiation at elevated temperatures [6–9].

Numerous attempts have been made to explore radiation tolerance of nanostructured metallic materials. Zinkle and Singh proposed grain size dependent nucleation of defects based on the observation of grain boundary denuded zone (free of defect clusters by GBs) in neutron irradiated alloys [10–12]. Bai et al., through atomistic simulations, showed that interstitials were first loaded into the grain boundaries, followed by their emission (upon super saturation) back to (unloaded) the interior of grains to annihilate vacancies [13]. Sun et al. studied Fe–Cr–Ni alloys with an average grain size of ~400 nm, processed by equal channel angular pressing (ECAP) and observed significant improvement of radiation tolerance, that is, the density of defect clusters and the magnitude of radiation hardening were both lower in fine grained materials [14]. They have also shown by using in situ Kr ion radiation in transmission electron microscopy that high angle grain boundaries in nanocrystalline Ni can actively engage and remove discrete dislocation loops and dislocation segments [15]. Yu et al. revealed a reduction of helium bubble density with decreasing grain size in nanocrystalline (NC) Fe films prepared by magnetron sputtering [16]. The same authors have also investigated radiation induced damage in nanotwinned Ag subjected to Kr ion radiations at room temperature, and revealed that coherent twin boundaries can effectively destruct stacking fault tetrahedra, which are typically very stable in irradiated metallic materials [17]. Wang et al. showed that NC TiN has superior radiation tolerance against He ion irradiation [18]. Odette

* Corresponding author. Tel.: +1 (979) 845 2143; fax: +1 (979) 845 3081.
E-mail address: zhangx@tamu.edu (X. Zhang).

X. Zhang[1]

Department of Mechanical Engineering,
Materials Science and Engineering Program,
Texas A&M University,
College Station, TX 77843-3123
e-mail: zhangx@tamu.edu

E. G. Fu

Nan Li

A. Misra

Y.-Q. Wang

Materials Physics and Application Division,
Los Alamos National Laboratory,
Los Alamos, NM 87545

L. Shao

Department of Nuclear Engineering,
Texas A&M University,
College Station, TX 77843-3128

H. Wang

Department of Electrical Engineering,
Texas A&M University,
College Station, TX 77843-3128

Design of Radiation Tolerant Nanostructured Metallic Multilayers

We review He ion induced radiation damage in several metallic multilayer systems, including Cu/V, Cu/Mo, Fe/W, and Al/Nb up to a peak dose of several displacements per atom (dpa). Size dependent radiation damage is observed in all systems. Nanolayer composites can store a very high concentration of He. Layer interfaces promote the recombination of opposite type of point defects and hence reduce the accumulative defect density, swelling, and lattice distortion. Interfaces also alleviate radiation hardening substantially. The chemical stability of interfaces is an important issue when considering the design of radiation tolerant nanolayer composites. Immiscible and certain miscible systems possess superior stability against He ion irradiation. Challenge and future directions are briefly discussed. [DOI: 10.1115/1.4006979]

Keywords: radiation damage, metallic multilayers, size effect, radiation hardening, He bubbles

1 Introduction

In nuclear reactors, neutron or proton irradiation can generate damage as high as a few hundred dpa over the years. The primary radiation damage event in metals is the displacement of atoms and the consequent formation of Frenkel (vacancy interstitial) pairs and various aggregates of defects, such as dislocation and interstitial loops, voids, and stacking fault tetrahedra (SFTs). Radiation damage in conventional bulk metals depends sensitively on crystal structures and stacking fault energy. For instance, a large number of interstitial loops and small voids have been observed in bcc metals, such as Fe, V, Mo, etc [1–6]. On the other hand, high density SFT and vacancy clusters were observed in fcc metals [7–13]. Radiation damage also depends on the energy of knock on atoms, dose, dose rate, and radiation temperature [14–16]. At elevated temperature, the density of defects can be decreased by two orders of magnitudes observed in various systems.

Radiation induced voids and He bubbles are two other major type of defects extensively studied in the past. Void swelling has been frequently observed in neutron irradiated fcc and bcc metals and can be very significant in irradiated austenitic stainless steels [17–20]. The rate of void swelling also increases with increasing total dose and dose rate [3]. The accumulation of He atoms in metals is of particular concern as they may lead to the degradation of mechanical properties [21]. The nucleation mechanisms of He bubbles in metals, including the dependence on radiation temperature, displacement rate, and accumulated He concentration have been studied previously [4,22–32]. After nucleation, He bubbles may grow through mechanisms, such as bubble migration and coalescence or Ostwald ripening [33–36].

Grain refinement is an effective strategy to improve radiation tolerance of structural metals. High angle grain boundaries can promote the recombination of interstitials and vacancies and hence reduce the density of defect clusters. Singh [37] showed that the growth rate of voids induced by 1 MeV electron radiation in an electron microscope was reduced when the growing voids were in close proximity to grain boundaries which had defect depleted zones. Sun et al. [38] showed that the bulk ultrafined grained Fe-14Ni-16Cr alloys processed by equal channel angular pressing had enhanced radiation tolerance as evidenced by reduced He bubble density and alleviated radiation hardening. In parallel, similar phenomenon was observed in He irradiated nanocrystalline Fe, Ni, and Au [39–41]. It was shown that the density of defect clusters decreased in irradiated nanocrystalline Pd and ZrO_2 [42]. MD simulations showed that the grain boundaries can be effective interstitial sinks, leaving vacancy clusters inside grains [43]. Nanocrystalline TiNi and $MgGa_2O_4$ appeared to show enhanced resistance to amorphization [44,45]. Nanocrystalline TiN produced by pulsed laser deposition has also shown a size dependent enhancement of radiation tolerance [46].

Multilayer interfaces have shown significant impact on radiation tolerance of metallic nanocomposites. In what follows, we review some of the highlight on size dependent enhancement of radiation tolerance in metallic multilayers. The emphasis was put mainly in the multilayers studied in the authors' research groups at Texas A&M University and Los Alamos National Laboratory as the deposition and radiation conditions were comparable in these systems.

---

[1]Corresponding author.

Radiation damage in helium ion irradiated nanocrystalline Fe

K.Y. Yu [a], Y. Liu [a], C. Sun [a], H. Wang [b], L. Shao [c], E.G. Fu [d], X. Zhang [a,*]

[a] Department of Mechanical Engineering, Materials Science and Engineering Program, Texas A&M University, College Station, TX 77843-3123, United States
[b] Department of Electrical and Computer Engineering, Texas A&M University, College Station, TX 77843-3128, United States
[c] Department of Nuclear Engineering, Texas A&M University, College Station, TX 77843-3133, United States
[d] Materials Physics and Applications Division, Los Alamos National Laboratory, Los Alamos, NM 87545, United States

ARTICLE INFO

ABSTRACT

Fe films with an average columnar grain size varying from 49 to 96 nm are deposited by magnetron sputtering technique. Sputtered films have predominant body centered cubic structure together with a small fraction of face centered cubic phase. Bulk Fe with an average grain size of 700 nm is also irradiated at the same condition for comparison. Helium bubbles are observed in Fe films and bulk Fe irradiated by 100 keV helium ions to a fluence of 6×10^{20} ions/m^2 at room temperature. Smaller grains lead to lower density of He bubbles. Radiation hardening in Fe films is much less than that of bulk Fe, and is a combined consequence of He bubble induced hardening and radiation induced compressive stress in Fe films.

© 2011 Elsevier B.V. All rights reserved.

1. Introduction

Energetic particles during radiation interact with atoms of the target material and induce a large number of point defects, such as vacancies and interstitials. Point defects aggregate to form vacancy clusters, voids, dislocation loops and stacking fault tetrahedron [1–4]. Void swelling and He embrittlement may lead to severe degradation of mechanical properties [5,6]. It is of great interest to develop radiation tolerant materials that can promote the annihilation of radiation induced defects. Studies have shown that certain grain and phase boundaries may act as preferential trapping sites for irradiation induced point defects and their clusters, promote recombination of interstitials and vacancies, and thus alleviate the degradation of mechanical properties [7,8]. It has been established that He plays an important role on the evolution of microstructures and mechanical properties of irradiated materials [9–11]. Helium, in existence of high concentration of vacancy clusters, can quickly combine with vacancy clusters to form He bubbles [6]. Bubble density in some of He ion irradiated metals can approach 10^{23}/m^3 or greater [12,31,33]. Understanding these phenomena is important to develop radiation tolerant materials.

Since stainless steels are commonly used as nuclear reactor structural components, its matrix element, Fe, has been investigated extensively for radiation response [13–17]. He implantation induced radiation damage in Fe has been widely studied by modeling and simulation, including the formation and diffusion of He clusters and bubbles [18,20], He-grain boundary interactions [21,22,36], He-dislocation interactions [23], He cluster thermal stability [24,27] and bubble pressure and size [28]. These studies have

demonstrated that He atoms can be absorbed by both dislocations and grain boundaries. He has a higher binding energy to grain boundaries due to their greater excess volume [11,36]. Bubble density and size are related to grain boundary structures [19,21]. Experimentally, He desorption has been investigated in both single crystal and polycrystalline Fe [26,29], where polycrystals are found to be more favorable for He absorption.

Nanostructured materials have high volume fraction of interfaces, including high angle grain boundaries, phase boundaries and layer interfaces. These high energy defects may act as point defect sinks and thus lead to enhancement of radiation tolerance [3,25,30]. Recent studies show that Cu/Nb, Cu/V and Fe/W multilayer films can significantly reduce radiation induced defects due to their abundant interfacial area [30–34]. Size dependent reductions of He bubble density, lattice distortion, swelling as well as radiation hardening have been observed in He ion irradiated Cu/V multilayers [31,32]. Furthermore the study of He ion irradiated Cu/Mo multilayers shows that segregation of He bubbles to interfaces is directly related to the vacancy-to-He concentration ratio [33]. A relatively low concentration of vacancies allows He to diffuse to the interface and form He bubbles at interfaces. Another type of boundary, metal/oxide interface, can also dramatically enhance radiation tolerance. Uniformly distributed nanoscale oxide precipitates in oxide-dispersion-strengthened (ODS) alloys, have shown superior void swelling resistance and high temperature thermal stability [14]. Nanocrystalline Fe and its alloys subjected to different heavy ion (Kr) radiations have been investigated by Karpe et al., who showed that Kr ions could trigger faster grain growth because of denser collision cascade [35]. Size dependent radiation response has also been found in He irradiated stainless steel, in terms of delayed void nucleation, lower void densities and reduced void swelling by decreasing grain size [8]. It has also

* Corresponding author. Tel.: +1 979 845 2143.
E-mail address: zhangx@tamu.edu (X. Zhang).

Enhanced radiation tolerance of ultrafine grained Fe–Cr–Ni alloy

C. Sun [a], K.Y. Yu [a], J.H. Lee [b], Y. Liu [a], H. Wang [b], L. Shao [c], S.A. Maloy [d], K.T. Hartwig [a], X. Zhang [a,*]

[a] Department of Mechanical Engineering, Materials Science and Engineering Program, Texas A&M University, College Station, TX 77843-3123, USA
[b] Department of Electrical and Computer Engineering, Texas A&M University, College Station, TX 77843-3123, USA
[c] Department of Nuclear Engineering, Texas A&M University, College Station, TX 77843-3123, USA
[d] Materials Science and Technology Division, Los Alamos National Laboratory, Los Alamos, NM 87545, USA

ABSTRACT

The evolutions of microstructure and mechanical properties of Fe–14Cr–16Ni (wt.%) alloy subjected to Helium ion irradiations were investigated. Equal channel angular pressing (ECAP) process was used to significantly reduce the average grain size from 700 μm to 400 nm. At a peak fluence level of 5.5 displacement per atom (dpa), helium bubbles, 0.5–2 nm in diameter, were observed in both coarse-grained (CG) and ultrafine grained (UFG) alloy. The density of He bubbles, dislocation loops, as well as radiation hardening were reduced in the UFG Fe–Cr–Ni alloy comparing to those in its CG counterpart. The results imply that radiation tolerance in bulk metals can be effectively enhanced by refinement of microstructures.

© 2011 Elsevier B.V. All rights reserved.

1. Introduction

Under high energy particle radiation, atoms in crystalline metals are displaced from their regular lattice sites, resulting in the formation of point defects (vacancies and interstitials) [1,2]. These point defects can be annihilated by recombination, or aggregate to form defect clusters such as bubbles [3], voids [4], dislocation loops [5], and stacking fault tetrahedral (SFT) [6]. Austenite stainless steels are commonly used in some nuclear reactor systems, including light water reactor (LWR) and fast breeder reactor (FBR). They have been considered as potential structural materials in fusion reactors due to their excellent corrosion resistance, processability and good creep and fatigue resistance at elevated temperatures [7–9]. However, high rate of Helium atom accumulation under neutron radiation in austenite stainless steel is a major concern because high density of He atoms could combine with vacancy clusters to form He bubbles, which may grow large enough to become voids, and lead to the void swelling and degradation of mechanical properties, such as radiation hardening and He embrittlement [10,11]. Significant void swelling, radiation induced hardening and loss of ductility have been reported in austenite stainless steels [12–14].

Numerous strategies have been explored to enhance radiation tolerance of metallic materials. In general, increasing the density of defect sinks is an effective approach for alleviating radiation damage. It has been reported that the radiation-induced point defects can be effectively trapped by dislocations. Cold working, which produces high density of dislocations, has been used to suppress void swelling in austenitic stainless steel [15,16]. Another

approach, introduction of secondary precipitates, is also adopted to enhance the radiation tolerance. D9 steel with composition of Fe–15Cr–14Ni (wt.%) and TiC precipitates has been developed and shown enhanced void swelling resistance [17].

Grain size also has a significant impact on the radiation behaviors of materials. By reducing the grain size, the grain boundary area per unit volume increases. The increase of grain boundary fraction is expected to promote the recombination of interstitials and vacancies and thus hinder the formation of defect clusters and enhance radiation tolerance [18]. Singh [19] pointed out that void nucleation and void swelling are grain size dependent in stainless steel, and grain refinement can enhance swelling resistance of stainless steel during electron radiation. Rose et al. [20] have reported that the defect cluster density in irradiated nanocrystalline Pd and ZrO_2 was dramatically reduced by reducing the grain size, and no defects could be detected in smallest Pd (<30 nm) and ZrO_2 (<15 nm) grains. Samaras et al. [21] investigated the influence of grain boundary structure on the primary damage state by using molecular dynamics simulations, and showed that grain boundary acted as interstitial sink, and vacancy clusters remained after solidification of cascade events. Moreover, nanocrystalline TiNi and $MgGa_2O_4$ reveal enhanced amorphization resistance [22,23]. Nanocrystalline TiN produced by pulsed laser deposition has also shown a size dependent enhancement of radiation tolerance [24].

Recent studies have shown that immiscible layer interfaces in He ion irradiated metallic nanolayers composites, such as Cu/Nb [25–28], Cu/Mo [29] and Cu/V [30,31], can effectively mitigate swelling, lattice distortion and radiation hardening, and the enhancement of radiation tolerance has a clear size dependence, i.e., nanolayers with smaller layer thickness typically show great improvement of radiation tolerance. Furthermore the immiscible

Taylor & Francis
Taylor & Francis Group

Fluence-dependent radiation damage in helium (He) ion-irradiated Cu/V multilayers

E.G. Fu[ab], H. Wang[c], J. Carter[d], Lin Shao[d], Y.Q. Wang[b] and X. Zhang[a]*

[a]Department of Mechanical Engineering, Materials Science and Engineering Program, Texas A&M University, College Station, TX 77843-3123, USA; [b]Materials Science and Technology Division, Los Alamos National Laboratory, Los Alamos, NM 87545, USA; [c]Department of Electrical and Computer Engineering, Texas A&M University, College Station, TX 77843-3128, USA; [d]Department of Nuclear Engineering, Materials Science and Engineering Program, Texas A&M University, College Station, TX 77843-3133, USA

We have explored the capacity of Cu/V interfaces to absorb helium ion radiation-induced defects spanning a peak damage range of 0.6–18 displacements per atom (dpa). The study provides evidence of alleviated nucleation of He bubbles in the multilayer films from Cu/V 50 nm to Cu/V 2.5 nm. Layer interfaces are retained in all irradiated specimens. Peak bubble density increases monotonically with fluence, and is lower in multilayers with smaller individual layer thickness. Radiation hardening decreases with decreasing layer thickness and appears to reach saturation upon peak radiation damage of 6 dpa. Size- and fluence-dependent radiation damage in multilayers is discussed.

Keywords: multilayer thin films; transmission electron microscopy (TEM); nanoindentation; radiation damage

1. Introduction

Radiation induces damage in materials by violent collisions between energetic particles (neutrons and ions) and target atoms. Long-term irradiation of metals can lead to damage in the form of swelling, blistering, embrittlement, fracture and exfoliation of surfaces in the metals. Void swelling frequently occurs in neutron-irradiated structural metals, such as steels, due to growth of vacancy clusters. Significant void swelling has been observed in irradiated metals and alloys [1]. Degradation of mechanical properties, manifested as embrittlement and loss of ductility, is a serious threat to the application of structural alloys in nuclear reactors. In parallel, significant radiation-hardening occurs frequently due to irradiation-induced point defects and clusters, as well as diminished dislocation activities.

In bulk metals, the concentration of irradiation-induced defects and the magnitude of irradiation-hardening typically scale with increasing fluence, and reach saturation at certain fluence levels. For instance, Singh and Zinkle [2] reviewed

---

*Corresponding author. Email: zhangx@tamu.edu

Microstructure and strengthening mechanisms in Cu/Fe multilayers

Y. Chen [a], Y. Liu [a], C. Sun [a], K.Y. Yu [a], M. Song [a], H. Wang [b], X. Zhang [a,*]

[a] *Department of Mechanical Engineering, Materials Science and Engineering Program, Texas A&M University, College Station, TX 77843-3123, USA*
[b] *Department of Electrical and Computer Engineering, Materials Science and Engineering Program, Texas A&M University, College Station, TX 77843-3128, USA*

Abstract

Nanostructured Cu/Fe multilayers on Si (1 1 0) and Si (1 0 0) substrates were prepared by magnetron sputtering, with individual layer thicknesses h varying from 0.75 to 200 nm. The growth orientation relationships between Cu and Fe at the interfaces were determined to be of the Kurdjumov–Sachs and Nishiyama–Wasserman type. Nanoscale columnar grains in Fe, with an average grain size of 11–23 nm, played a dominant role in the strengthening mechanism when $h \geq 50$ nm. At smaller h the hardness of Cu/Fe multilayers with (1 0 0) texture approached a peak value, followed by softening due to the formation of fully coherent interfaces. However, abundant twins were observed in Cu/Fe films with (1 1 1) texture when $h = 0.75$ nm, which led to the retention of high hardness in the multilayers. Published by Elsevier Ltd. on behalf of Acta Materialia Inc.

Keywords: Multilayers; Strengthening; Nanoindentation; Twinning; Sputtering

1. Introduction

Certain metallic multilayers with nanoscale layer thicknesses exhibit high strength close to the theoretical values [1–6]. The mechanisms of deformation have been extensively studied in metallic multilayers. Dislocation pile-up [7], moduli mismatches [8], misfit dislocations, and coherency stress [9] are among some of the important factors that contribute to hardening. Some of the models that explain the high strength of multilayers are briefly described next.

The Hall–Petch model [3,7] operates when the individual layer thickness h is greater than tens of nanometers. Strengthening arises from dislocation pile-up on the glide plane against the grain or interphase boundaries. The hardness increases linearly with $h^{-1/2}$, following the Hall–Petch model. Thus the Hall–Petch slope that indicates the resistance of the boundary is often used to predict the peak strength of multilayers [3,10,11]. However, in certain cases the peak strength predicted from the slope is not consistent

with the measured values, as the multilayers may contain defects, e.g. columnar grains and twins [12–14] that have much smaller dimensions than the individual layer thicknesses. Certain modifications have thus been made. Misra et al. [15] developed a deformation mechanism map to determine the dominant feature size for dislocation pile-up against boundaries. Pande et al. [16] developed a model to incorporate the influence of annealing twins on the Hall–Petch slope.

At smaller h, of the order of tens of nanometers, the confined layer slip (CLS) model based on the Orowan bowing mechanism [1,17] is more appropriate. At this length scale dislocation pile-up becomes more difficult. Correspondingly, dislocations are confined by and glide between layer interfaces, instead of being transmitted across the interfaces, because the stress required to bow out dislocations is less than that for transmission of dislocations across an interface. Recently Misra et al. [11] developed a refined CLS model by considering interface stress and dislocation–dislocation interactions.

An interface barrier strength (IBS) mechanism operates when h is several nanometers. The strength of multilayers at such length scales is determined by the inherent resistance

* Corresponding author. Tel.: +1 979 845 2143.
 E-mail address: zhangx@tamu.edu (X. Zhang).

Scripta MATERIALIA

ELSEVIER

Significant enhancement in the thermal stability of nanocrystalline metals via immiscible tri-phases

Y. Chen,[a] Y. Liu,[a] F. Khatkhatay,[b] C. Sun,[a] H. Wang[b] and X. Zhang[a,*]

[a]*Department of Mechanical Engineering, Materials Science and Engineering Program, Texas A&M University, College Station, TX 77843-3123, USA*
[b]*Department of Electrical and Computer Engineering, Materials Science and Engineering Program, Texas A&M University, College Station, TX 77843-3128, USA*

The thermal stability of sputtered Co–Cu–Ag tri-phase immiscible nanocomposites (TPINs) was compared to nanocrystalline $Cu_{50}Ag_{50}$ and monolithic Cu. After annealing at 973 K, the grain size of $Co_{34}Cu_{33}Ag_{33}$ was ~115 nm, whereas that of $Cu_{50}Ag_{50}$ increased to over 700 nm. The hardness of annealed $Co_{34}Cu_{33}Ag_{33}$ TPIN remained high, ~3 GPa, comparing to only 1.0 GPa for $Cu_{50}Ag_{50}$ film. The remarkable thermal stability of the TPIN is largely achieved via the introduction of a third immiscible phase, forming abundant tri-phase triple junctions.

Nanocrystalline (NC) metals and alloys exhibit ultra-high mechanical strength [1–7], superior wear resistance [8–10] and remarkable radiation tolerance [11–15] compared to their bulk counterparts. However, they are vulnerable to grain growth due to a large driving force for coarsening arising from a high density of high-angle grain boundaries. Numerous efforts have been made to stabilize NC metals. There are two basic strategies to inhibit grain growth. Kinetically, second phase or solute drag can be used to slow down the migration of grain boundaries in, for example, Ni–P [16] and Fe–Al alloys [17]. Thermodynamically, grain growth is inhibited by solute segregation. The driving force for grain growth is proportional to the effective grain-boundary free energy, γ^*, which is written as [18,19]:

$$\gamma^* = \gamma_0 + \Delta G_{seg}\Gamma, \qquad (1)$$

where γ_0 is the intrinsic (non-segregated) grain boundary energy, ΔG_{seg} is the segregation energy and Γ is the excess amount of segregated solute per unit area on the grain boundaries. Two energetically competing processes are considered during grain growth: the reduction in grain boundary area and the reabsorption of solute atoms into matrix. If the segregation energy is negative, the reabsorption of segregated solute atoms (at grain

boundaries) back into the matrix requires extra energy. A metastable state is obtained when the decrease in energy caused by a reduction in grain boundary area is balanced by the energy required for reabsorption of solute atoms. Thus, segregation of certain solute atoms to grain boundaries can reduce the effective grain boundary free energy, to near zero, and thus the driving force for grain growth is reduced. The thermodynamic strategy exhibits weak temperature dependence and is often more effective than the kinetic method, and hence has been extensively studied theoretically [18,20–22] and experimentally in numerous systems [19,23–32]. In these systems, however, obvious grain growth can still take place upon further annealing at higher temperature. For instance, in the TiO_2–Ca system [24], grain growth occurred after the formation of $CaTiO_3$ precipitates; Vanleeuwen et al. [19] reported grain growth in $Pd_{81}Zr_{19}$ when annealing was performed above 973 K. Botcharova et al. [32] investigated immiscible Cu–Nb alloy, and reported high stability of NC Cu matrix. However, abnormal growth of Nb precipitates to ~600 nm was observed at 1173 K.

Achieving superior thermal stability in NC metals remains a major challenge. Here we introduce the concept of tri-phase immiscible nanocomposites (TPINs) to enhance the thermal stability of NC metals. In TPINs, three immiscible phases are intermingled uniformly with one another. The immiscibility of any two phases

* Corresponding author. Tel.: +1 (979) 845 2143; e-mail: zhangx@tamu.edu

Interface-enabled Defect Reduction in He Ion Irradiated Metallic Multilayers

X. Zhang, E.G. Fu, A. Misra, and M.J. Demkowicz

Metallic multilayers are good model systems to explore the effects of heterophase interfaces in reducing radiation damage in structural materials. We summarize recent studies on radiation damage in immiscible face-centered cubic/body-centered cubic metallic multilayers, in particular Cu/V and Cu/Nb. These multilayers have shown unique characteristics compared to bulk metals under irradiation, including several orders of magnitude higher He solid solubility, dramatic reduction of bubble density, interface confined growth of He bubbles, and much lower radiation hardening. The mechanisms for interface enhanced radiation tolerance are briefly discussed.

INTRODUCTION

For structural metals in nuclear reactors, helium produced as a transmutation product can cause significant dimensional changes, irradiation hardening, and embrittlement.[1–3] Since He solubility in metals is very low, typically below the ppm level,[4,5] and it binds strongly with vacancies, He forms nanometer-sized bubbles via clustering with radiation-induced vacancies. These bubbles may nucleate heterogeneously on dislocations and grain boundaries.[6,7] Extending the performance of structural metals in nuclear reactors thus requires the ability to mitigate the effects of He implantation on material microstructure, particularly to prevent the degradation of material properties by the growth of bubbles and the subsequent formation of blisters.[8] For example, in nuclear reactors, austenitic stainless steel can swell at a rate of 1%/displacements per atom (dpa): a process accelerated by implanted He.[9] A 316 austenitic stainless steel after 14% swelling at 400°C in a nuclear reactor was reported to become so brittle that it fractured during clamping at room temperature.[10]

Singh[11] used in situ 1 MeV electron irradiation in a high voltage electron microscope to show that the growth rate of voids is reduced markedly as the distance between the growing voids and grain boundaries becomes smaller than the 'defect depleted zone width.' As soon as the growing voids reached a grain boundary, void growth was found to cease altogether. These findings indicated that grain boundaries could lead to reduced swelling in steels. Recently there has been a significant interest in designing other radiation-tolerant structural materials using grain and/or phase boundaries as sinks for defects.

Besides grain boundaries, heterophase interfaces in multilayer systems have also been shown to be effective sinks for radiation-induced defects.[12–17] The current studies of radiation tolerant multilayers mostly focus on a funda-

mental science issue: point defect-interface interactions. Studies have shown that certain multilayer systems may significantly reduce radiation induced damage in metallic materials.[12–17] Here we summarize some aspects on interface enabled size dependent enhancement of radiation tolerance in immiscible face-centered cubic/body-centered cubic (f.c.c./b.c.c.) nanolayers. In particular we will discuss interfacial stability under high dose He ion implantation, reduction of He bubbles, and lattice distortion, as well as mitigation of radiation induced hardening. Multilayers with enhanced resistance to radiation can potentially be used in nuclear reactors as radiation protective coatings or fuel pin clad. Structural materials with multilayer structures could be fabricated to enhance radiation tolerance.

CHEMICAL STABILITY OF INTERFACES

High energy He ions can cause ballistic intermixing at phase boundaries. In our previous studies, He ion irradiation at a fluence of 6×10^{16} / cm^2 (100 keV) was found to lead to the formation of intermetallic phases in Al/Nb multilayers[12] and completely destroyed the layered morphology in Fe/W 1 nm multilayer films.[13] Both Al/Nb and Fe/W are miscible systems, where intermetallic phases form along interfaces after irradiation. However, radiation at similar fluences did not lead to any noticeable intermixing in Cu/V[14] and Cu/Nb[15–17] nanolayers, which are immiscible. Figure 1 shows the microstructure of irradiated Cu/V 50 nm and Cu/V 2.5 nm multilayers examined by scanning transmission electron microscopy. The interfaces remain chemically abrupt after irradiation as they were in the as-deposited state, indicating that thermally

Size dependent strengthening mechanisms in sputtered Fe/W multilayers

Nan Li,[1] K. Y. Yu,[1] J. Lee,[2] H. Wang,[2] and X. Zhang[1,a]

[1]*Department of Mechanical Engineering, Materials Science and Engineering Program, Texas A&M University, College Station, Texas 77843-3123, USA*

[2]*Department of Electrical and Computer Engineering, Texas A&M University, College Station, Texas 77843-3128, USA*

We investigate size dependent strengthening mechanisms in sputtered Fe/W multilayers with individual layer thickness, h, varying from 1 to 200 nm. Microstructure analyses reveal that Fe/W has incoherent bcc/bcc interface when h is greater than 5 nm. When h decreases to 1–2.5 nm, the interface becomes semicoherent, and Fe and W show significant lattice distortions comparing to their bulk counterpart due to interface constraint. The layer thickness dependent drastic variations in x-ray diffraction profiles are simulated well by using an analytical model. Film hardness increases with decreasing h, and approaches a maximum value of 12.5 GPa when h is 1 nm. The layer thickness dependent film hardnesses are compared with analytical models. Koehler's image force plays a major role in determining the maximum strength of composites at smaller h. © *2010 American Institute of Physics*. [doi:10.1063/1.3400130]

I. INTRODUCTION

Mechanical properties of metallic multilayer films have received significant attention recently because the maximum hardness in some systems can approach the theoretical strength of the composite.[1,2] A variety of metallic multilayer systems have been explored in an attempt to construct different type of interfaces to achieve high strength. A majority of these studies focus on systems with fcc/fcc type interfaces, such as Cu/Ni, Cu/Ag and Cu/330 austenitic stainless steel,[3–5] and systems with fcc/bcc type interfaces, such as Cu/Nb, Cu/Cr, Cu/W, and Pt/Fe.[3,6,7] There are few studies on size dependent strengthening mechanisms in systems with bcc/bcc type interfaces.[7,8] In general, film hardness increases with decreasing individual layer thickness, h, when h is greater than several tens of nanometers. Strengthening in this regime can be explained well by the Hall–Petch (HP) dislocation pile-up model.[9,10] When h decreases further, film hardness-layer thickness relation deviates from the prediction of conventional HP model, indicating dislocation pile-ups are less likely. Instead, the Orowan bowing model may be a more realistic deformation mechanism.[11,12] At a few nanometer length scale, most multilayer systems reach a maximum hardness (referred to as peak hardness thereafter). In coherent multilayer systems, such as Cu/Ni, peak hardness is dominated by coherency stress, which is proportional to shear modulus and mismatch strain. In system with large elastic modulus mismatch, Koehler stress due to the large modulus difference of the components may prevail.[13–15] Recently it has been shown by molecular dynamic (MD) simulations that in systems with "opaque" interface (referring to incoherent layer interface separating crystals with discontinuous slip system), such as Cu/Nb, interface shear strength is lower than that of each constituent.[16] Dislocations are therefore attracted to interface, and significant dislocation core spreading occurs at the "weak" interface.[16] As a result of dislocation core spreading, dislocations lose their singularity, making it very difficult to reemit into the opposite constituent. The weak interface in Cu/Nb therefore leads to significant strengthening at a few nanometer length scales. Recent review articles have described the work in this area in considerable detail.[17–19] In systems with diffuse composition gradient, film hardness may decrease due to intermixing along layer interface.[20,21]

In this study, the size dependent strengthening mechanisms of an incoherent bcc/bcc system, consisting of a series of Fe/W multilayers, were investigated. Comparisons of peak hardness among Fe/W and several other W-based multilayers have been made to understand the influence of interface on peak strength of multilayers. This study will provide more insight to the understanding of mechanisms that may lead to high strength in metallic multilayers with bcc/bcc type interface.

II. EXPERIMENT

Fe/W multilayers were deposited by the magnetron sputtering technique at room temperature on Si(100), (111), and SiO_2 substrates. The vacuum chamber was evacuated to a base pressure less than 5×10^{-8} torr prior to deposition. The constituents within the multilayers have equal individual layer thickness varying from 1 to 200 nm. The total film thickness was about 2 μm for all multilayers. Hence the number of bilayers varies from 5 for Fe 200 nm/W 200 nm (referred to as Fe/W 200 nm thereafter) to 1000 for Fe/W 1 nm multilayers. Single layer, 2 μm thick Fe and W films were sputter-deposited by using the same technique. Transmission electron microscopy (TEM) was performed on a JEOL 2010 microscope operated at 200 kV. High-resolution TEM (HRTEM) experiments were performed on a JEOL 3000F microscope operated at 300 kV. Scanning TEM (STEM) was performed on FEI Tecnai G2 F20 FE-TEM with

a)Author to whom correspondence should be addressed. Electronic mail: zhangx@tamu.edu. Tel.: (979) 845-2143.

ELSEVIER

In situ TEM observations of room temperature dislocation climb at interfaces in nanolayered Al/Nb composites

Nan Li,[a,b] J. Wang,[b,*] J.Y. Huang,[c] A. Misra[b] and X. Zhang[a,**]

[a]*Department of Mechanical Engineering, Texas A&M University, College Station, TX 77843-3123, USA*
[b]*Los Alamos National Laboratory, Los Alamos, NM 87545, USA*
[c]*Center for Integrated Nanotechnologies, Sandia National Laboratory, Albuquerque, NM 87185, USA*

Using in situ nanoindentation, we investigated dislocation–interface interactions in Al/Nb multilayers. Preferential storage of dislocations at interfaces, as opposed to within layers, was observed. Recovery of dislocations was observed to occur through climb in the interfaces. The rapid climb of dislocations is ascribed to high vacancy diffusivity and vacancy concentration in the interfaces. The vacancy formation energy at interfaces, 0.12 eV, as estimated from the experimentally measured climb rates, was found to be significantly lower than in the bulk.
Published by Elsevier Ltd. on behalf of Acta Materialia Inc.

Keywords: in situ TEM; Dislocations; Multilayers; Climb

Interfaces between dissimilar metals often exhibit unique properties that are not found in bulk crystals [1]. For example, Cu/Nb interfaces can adopt multiple atomic structures with nearly degenerate energies, stimulating the delocalization of point defects within the interface and their interaction [2–11]. Atomistic simulations have revealed that the formation and migration energies of vacancies and interstitials within interfaces are lower than that in bulk materials, implying that these interfaces can act as strong sinks for vacancies and interstitials [9,10]. Using atomistic simulations, we have shown that these interfaces can act as strong barriers for slip transmission due to: (i) trapping of glide dislocations at interfaces due to the spreading of dislocation cores along the low shear resistance interface; (ii) the geometric discontinuity of slip systems across these interfaces [2–6]. Furthermore, atomistic simulations revealed that glide dislocations could efficiently climb near and within interfaces through the emission and absorption of vacancies at dislocation cores [11]. Through dislocation climb, dislocation debris within interfaces can be reassembled into lattice dislocations, moving away from interfaces under applied stress. In addition, reactions between interfacial dislocations

assisted by climb could lead to the annihilation of certain Burgers vectors components and, hence, contribute to the recovery of dislocation content at interfaces [12].

Atomistic simulations [2–5,8–12] and experimental studies [6,7] have suggested that the plastic flow behavior of nanolayered materials is controlled by the interaction of glide dislocations with interfaces. However, experimental studies, in particular real time observations of dislocation–interface interactions are still scarce. In situ straining in a transmission electron microscope has recently been used to elucidate several key phenomena in the deformation of nanocrystalline metals and thin films, e.g. grain coalescence and the interaction of dislocations with grain boundaries [13–16], the effect of impurities on interface motion [17,18], the dependence of nucleation and exhaustion of mobile dislocations on grain size [19] and detwinning mechanisms in nano-twinned Cu films [20]. In order to provide direct evidence of the interface-dominated deformation behavior of nanolayered materials, an Al/Nb multilayer with individual layer thicknesses of 5 nm was chosen in a study of in situ nanoindentation by transmission electron microscopy (TEM), because dislocation forests are not expected to form within layers at this length scale [5–7], decreasing the effect of multiple dislocation interactions.

In this paper, we report direct observations of dislocation–interface interactions in Al/Nb multilayers with individual layer thicknesses of 5 nm using in situ nano-

---

* Corresponding author. Tel.: +1 505 667 1238; e-mail addresses: wangj6@lanl.gov; zhangx@tamu.edu
** Corresponding author

The influence of interfaces on the formation of bubbles in He-ion-irradiated Cu/Mo nanolayers

Nan Li[ac], J.J. Carter[b], A. Misra[c], L. Shao[b], H. Wang[d] and X. Zhang[a]*

[a]Department of Mechanical Engineering, and Materials Science and Engineering Program, Texas A&M University, College Station, TX 77843-3123, USA; [b]Department of Nuclear Engineering, Texas A&M University, College Station, TX 77843-3133, USA; [c]Materials Physics and Application Division, Los Alamos National Laboratory, Los Alamos, NM 87545, USA; [d]Department of Electrical and Computer Engineering, Texas A&M University, College Station, TX 77843-3128, USA

The role of immiscible Cu/Mo interfaces on the formation of helium (He) bubbles in ion-irradiated Cu/Mo 5 nm multilayers is examined. Interfaces significantly enhance the critical He concentration above which bubbles, approximately 1 nm in diameter, are detected via through-focus imaging in a transmission electron microscope. He-to-vacancy ratio affects the formation and distribution of He bubbles. The diameter of He bubbles in Cu appears to be slightly larger than that in Mo.

Keywords: ion irradiation; Cu/Mo multilayers; He bubbles; interfaces

1. Introduction

A high rate of production of helium (He) is a major problem for the integrity of structural materials under neutron irradiation [1,2]. Because of low He solubility in metals [3,4], He atoms tend to combine with radiation-induced vacancy clusters to form He bubbles or voids [5–10]. Void swelling, together with interstitial loops, leads to irradiation hardening and embrittlement [11,12]. At large He concentrations, elevated temperature annealing can lead to unstable bubble growth and blistering [13]. Interfaces can act as effective sinks to absorb radiation-induced defects and He atoms because of a defect formation energy that is lower at interfaces than in the bulk [14,15]. Meanwhile certain type of interfaces, such as Cu/Nb, can adopt several mutable atomic structures with nearly degenerate energies, stimulating the delocalization of point defect cores within interface, and consequently promote the annihilation of vacancies and interstitials [16]. Recent studies have shown that immiscible Cu/Nb multilayers are extremely stable under He-ion irradiation [17].

*Corresponding author. Email: zhangx@tamu.edu

Interface enabled defects reduction in helium ion irradiated Cu/V nanolayers

E.G. Fu [a,b], A. Misra [b], H. Wang [c], Lin Shao [d], X. Zhang [a,*]

[a] Department of Mechanical Engineering, Materials Science and Engineering Program, Texas A&M University, College Station, TX 77843-3123, United States
[b] Materials Physics and Applications Division, Los Alamos National Laboratory, Los Alamos, NM 87545, United States
[c] Department of Electrical and Computer Engineering, Texas A&M University, College Station, TX 77843-3128, United States
[d] Department of Nuclear Engineering, Texas A&M University, College Station, TX 77843-3133, United States

ARTICLE INFO

ABSTRACT

Sputter-deposited Cu/V nanolayer films with individual layer thickness, h, varying from 1 to 200 nm were subjected to helium (He) ion irradiation at room temperature. At a peak dose level of 6 displacements per atom (dpa), the average helium bubble density and lattice expansion decrease significantly with decreasing h. The magnitude of radiation hardening decreases with decreasing individual layer thickness, and becomes negligible when h is 2.5 nm or less. This study indicates that nearly immiscible Cu/V interfaces spaced a few nm apart can effectively reduce the concentration of radiation induced point defects. Consequently, Cu/V nanolayers possess enhanced radiation tolerance, i.e., reduction of swelling and suppression of radiation hardening, compared to monolithic Cu or V.

1. Introduction

Radiation induced defects and evolutions of mechanical properties in neutron and ion irradiated metallic materials have been extensively studied [1–7]. During radiation the interactions between the energetic projectile particles and the atoms of the irradiated materials lead to atomic displacement damages, such as vacancies, interstitials, and their agglomerations in the form of vacancy clusters, voids and dislocation loops [8–12]. Stacking fault tetrahedra (SFT) as a result of agglomeration of vacancies is frequently observed in numerous irradiated metals and alloys with faced-centered cubic (FCC) structure, such as Au, Cu, Ni, Pd and austenitic stainless steel [13–19]. A high concentration of vacancy clusters and SFTs is observed in FCC Cu, whereas interstitial loops seem to prevail in irradiated body-centered cubic (BCC) V [20]. In fusion reactors, besides the aforementioned displacement damages, a high concentration of He atoms created via (n, α) or other transmutation reactions typically leads to a large number of He bubbles in irradiated structural metals [21–23]. Radiation induced void swelling can cause significant dimensional instability and degrade the mechanical properties in the form of embrittlement. Significant void swelling has been observed in neutron radiated 316L stainless steels [4]. Radiation hardening has been extensively studied in irradiated FCC and BCC monolithic metals, such as Cu and V [24–33]. In general, radiation hardening is substantial when metals are irradiated at temperature below 0.3–0.4 T_m, where T_m is the melting temperature [32]. The yield strengths of neutron irradiated Cu and V both increase with the extent of damage, displacement-per-atom (dpa). The increase of yield strength is approximately 200–300 MPa in bulk coarse-grained Cu and V irradiated at a damage level of ~1 dpa [34].

Microstructural control has been shown to be effective in suppressing radiation damage. Significant reduction of void swelling has been recognized in a series of ferritic/martensitic (F/M) steels [35–39] with BCC or body-centered tetragonal (BCT) structures. Also, oxide-dispersion-strengthened (ODS) alloys, with nanoscale oxides uniformly distributed in F/M steels, have shown superior void swelling resistance and high temperature thermal stability [40]. A high density of dislocations in cold-worked 316L stainless steel can moderately alleviate void swelling at low temperatures [3]. The aforementioned studies have shown that grain or phase boundaries may act as sinks for radiation induced point defects and their clusters, where recombination of interstitial and vacancy could occur and such recovery process assists the interfaces in maintaining their ability to continuously absorb point defects [41–44]. Singh [45] has shown that in austenitic stainless steels with grain size of 0.5–50 µm, smaller grains can effectively reduce the concentration of voids and void swelling. Furthermore, Singh and Foreman [46] have shown that the supersaturation of vacancy within grains is lower when grain size is smaller since grain boundaries are effective sinks to reduce radiation induced point defect density. Analytical work also shows that the sink strength of grain boundaries increases with decreasing grain sizes [47]. Increasing the volume fraction of grain or phase boundaries thus appears beneficial to alleviating radiation induced damage. Metallic nanolayer films possess very large interfacial areas. Recent studies show that immiscible Cu/Nb nanolayers, particularly those with a layer thickness of a few nm, are extremely resistant against He ion irradiation induced intermixing [48]. He bubbles are barely

He ion irradiation damage in Al/Nb multilayers

Nan Li,[1] M. S. Martin,[2] O. Anderoglu,[1] A. Misra,[3] L. Shao,[2] H. Wang,[4] and X. Zhang[1,a)]

[1]*Department of Mechanical Engineering and Materials Science and Engineering Program, Texas A&M University, College Station, Texas 77843-3123, USA*
[2]*Department of Nuclear Engineering, Texas A&M University, College Station, Texas 77843-3133, USA*
[3]*Materials Physics and Application Division, Los Alamos National Laboratory, Los Alamos, New Mexico 87545, USA*
[4]*Department of Electrical and Computer Engineering, Texas A&M University, College Station, Texas 77843-3128, USA*

We investigate the evolution of microstructure and mechanical properties of sputter-deposited Al/Nb multilayers with miscible fcc/bcc type interface and individual layer thickness, h, of $1-200$ nm, subjected to helium ion irradiations: 100 keV He$^+$ ions and a fluence of $6 \times 10^{16}/\text{cm}^2$. Helium bubbles, $1-2$ nm in diameter, are observed. When h is greater than 25 nm, hardnesses of irradiated multilayers barely change, whereas radiation hardening is more significant at smaller h. Transmission electron microscopy and scanning transmission electron microscopy studies reveal the formation of a thin layer of Nb$_3$Al intermetallic phase along the Al/Nb interface as a consequence of radiation induced intermixing. The dependence of radiation hardening on h is interpreted by using a composite model considering the formation of the hard Nb$_3$Al intermetallic layer. © *2009 American Institute of Physics*. [DOI: 10.1063/1.3138804]

I. INTRODUCTION

In general heavy ion irradiation of crystalline metallic alloys can cause dramatic variations, including amorphization or phase change.[1] Radiation with lighter ions, such as helium (He), can induce a large number of point defects as a consequence of nuclear collisions, including vacancies and interstitials, and defect clusters, such as He bubbles, voids, and dislocation loops.[2–4] Interplay of these defects can eventually lead to swelling,[5–8] blistering of metal surfaces,[9] and radiation embrittlement.[10] Hence particle irradiation has deleterious effects on the mechanical integrity and dimensional stability of structural metals and reduces their service time in nuclear reactors. Understanding the mechanisms of radiation induced damage in metallic materials is of great significance and could potentially lead to the discovery and development of radiation tolerant materials. Under this context, a unique approach has recently been proposed, i.e., to study layer interface mitigated radiation damage in metallic multilayers.[11–15] The anticipation of enhanced radiation tolerance in metallic nanolayers is based on the following rationale: interfaces act as sinks for radiation induced point defects and external species (such as He), and the enhanced diffusivity of point defects along interfaces could promote rapid recombination of unlike point defects and result in radiation tolerance superior to conventional single-phase bulk metals.[11–15] Such concept has been tested in Cu/Nb multilayer system. The study shows that room temperature irradiated (He ions at 33 keV and a total fluence of $1.5 \times 10^{17}/\text{cm}^2$) Cu/Nb multilayers with 4 nm individual layer thickness do not exhibit blistering upon annealing at 600 °C,

whereas blistering is observed in single layer Cu or Nb, and Cu/Nb multilayers with 40 nm individual layer thickness.[13] In parallel, our recent studies on Cu/V and Fe/W multilayers have shown that void swelling as well as radiation hardening have been significantly suppressed in these fine multilayers.[15,16]

In this paper, we investigate radiation damage in Al/Nb multilayers for the following purposes. First, Al/Nb has a unique fcc/bcc interface, where the interplanar spacing of Al (111) is essentially the same as that of Nb (110), whereas the mismatch between Cu (111) and V (110) is approximately 2.3%, and the mismatch is 11.2% in the case of Cu and Nb. Second, Al–Nb is a chemically miscible system with a negative heat of mixing of -18 J/mol,[17] distinctively different from that of immiscible Cu/V, 5 J/mol (Ref. 17) and Cu/Nb, 3 J/mol.[17] Hence the strength of Al–Nb interatomic bond at interface should be stronger than that of Al–Al and Nb–Nb bonds. Both characteristics imply that interactions of radiation induced point defects with Al/Nb interface could be largely different than those in Cu/V and Cu/Nb system. Finally, the microstructure and mechanical properties of as-received Al/Nb systems have been studied systematically, providing a base line for studying He ion irradiation induced damage in Al/Nb multilayers.[18] In this study, we reveal the retention of layer morphology in Al/Nb multilayers after significant He ion irradiation damage. Radiation hardening mechanisms due to the formation of Nb$_3$Al along layer interface and other defects are discussed.

II. EXPERIMENTAL PROCEDURES

Al/Nb multilayers were deposited by magnetron sputtering at room temperature on SiO$_2$ substrates. The vacuum chamber was evacuated to a base pressure less than 5

---

a)Author to whom correspondence should be addressed. Electronic mail: zhangx@tamu.edu. Tel.: (979) 845-2143.

105, 123522-1

Superior tolerance of Ag/Ni multilayers against Kr ion irradiation: an *in situ* study

K.Y. Yu[a], C. Sun[a], Y. Chen[a], Y. Liu[a], H. Wang[ab], M.A. Kirk[c], M. Li[d] and X. Zhang[ae]*

[a]*Department of Materials Science and Engineering, Texas A & M University, College Station, TX 77843-3123, USA;* [b]*Department of Electrical and Computer Engineering, Texas A & M University, College Station, TX 77843-3128, USA;* [c]*Materials Science Division, Argonne National Laboratory, Argonne, IL 60439, USA;* [d]*Nuclear Engineering Division, Argonne National Laboratory, Argonne, IL 60439, USA;* [e]*Department of Mechanical Engineering, Texas A & M University, College Station, TX 77843-3123, USA*

Monolithic Ag and Ni films and Ag/Ni multilayers with individual layer thickness of 5 and 50 nm were subjected to *in situ* Kr ion irradiation at room temperature to 1 displacement-per-atom (a fluence of 2×10^{14} ions/m^2). Monolithic Ag has high density of small loops (4 nm in diameter), whereas Ni has fewer but much greater loops (exceeding 20 nm). In comparison, dislocation loops, $\sim$4 nm in diameter, were the major defects in the irradiated Ag/Ni 50 nm film, while the loops were barely observed in the Ag/Ni 5 nm film. At 0.2 dpa (0.4×10^{14} ions/m^2), defect density in both monolithic Ag and Ni saturated at 1.6 and 0.2×10^{23}/m^3, compared with 0.8×10^{23}/m^3 in Ag/Ni 50 nm multilayer at a saturation fluence of $\sim$1 dpa (2×10^{14} ions/m^2). Direct observations of frequent loop absorption by layer interfaces suggest that these interfaces are efficient defect sinks. Ag/Ni 5 nm multilayer showed a superior morphological stability against radiation compared to Ag/Ni 50 nm film.

Keywords: Ag/Ni; *in situ* radiation; Kr; interface

1. Introduction

Neutron, proton or heavy ion irradiation can create a large amount of defect clusters in metals and lead to the degradation of mechanical properties in terms of swelling, radiation hardening and embrittlement [1–5]. By alloying and subsequent cold working or heat treatment, certain structural metallic materials can survive up to 60 years of irradiation [1,6]. However, the performance of these materials is still insufficient to meet the requirement for the next generation nuclear reactors: that is, these materials must sustain 300–400 displacements-per-atom (dpa) over 80 years [6,7]. It is a grand challenge to design advanced radiation tolerant metallic materials. The introduction of abundant defects sinks at nanometre-length scale into materials is one of the potential strategies to achieve significantly enhanced radiation tolerance. A large amount of defect sinks, such as dislocations, grain boundaries (GBs) and phase boundaries, may

*Corresponding author. Email: zhangx@tamu.edu